Desalination and Water Treatment
www.deswater.com
doi: 10.5004/dwt.2021.27633

235 (2021) 141–176
September

Recent advancements in the development of graphitic like carbon nitride ($g\text{-}C_3N_4$) photocatalyst for volatile organic compounds removal: a review

Said Al Mamari[a], Alex T. Kuvarega[b], Rengaraj Selvaraj[a,*]

[a]*Department of Chemistry, College of Science, Sultan Qaboos University, Al Khoudh., P.O. Box: 36, P.C. 123, Sultanate of Oman, email: rengaraj@squ.edu.om/srengaraj1971@yahoo.com (R. Selvaraj)*
[b]*Institute for Nanotechnology and Water Sustainability, College of Science, Engineering and Technology, University of South Africa, Florida, 1709, Johannesburg, South Africa*

Received 14 June 2021; Accepted 16 July 2021

ABSTRACT

Environmental pollution has a direct and indirect influence on human life and the ecosystem. The huge emissions from the industries such as oil factories, petrochemical plants and other sources could cause many influences such as human disease, global warming and ozone depletion. This calls for intensive research on renewable energy, decreasing atmospheric air pollution and water contamination. Graphitic carbon nitride, $g\text{-}C_3N_4$ has attracted much attention as a promising semiconductor material that can be used in a comprehensive photocatalytic application due to photochemical characteristics and thermal stability. $g\text{-}C_3N_4$ has the ability to generate charge carriers that form oxygen reactive species upon irradiation with light. The highly reactive oxygen species such as peroxides, superoxide, hydroxyl radical, singlet oxygen, and alpha-oxygen are responsible for the oxidative removal of volatile organic compounds (VOCs) pollutants. Besides, there is potential to improve the structural and catalytic performance of $g\text{-}C_3N_4$ through the formation of composite materials. This review article emphasizes strategies for synthesis, characterization and catalytic performance of $g\text{-}C_3N_4$ composites for removal of VOCs present in the environment. Recent advancements in the field were highlighted and gaps and hotspots in the fabrication of $g\text{-}C_3N_4$ based nanoengineered materials for removal of VOCs were thoroughly discussed.

Keywords: Graphitic carbon nitride; 2D nanostructures; Photocatalysis; Nanocomposites; Volatile organic compounds removal

1. Introduction

Volatile organic compounds (VOCs) are the main gaseous pollutants that cause harmful effects to the environment and on human health. The compounds which are emitted from transport vehicles, refineries, factories, commercial products and biogenic sources could play a significant role in air quality [1]. VOCs pollutants are not stable and have the tendency to spread and accumulate in the air, water and soil [2]. Many of them are carcinogenic and behave as ancestors for photochemical smog and stratospheric ozone depletion [3,4]. About 92% of the world's population lives in different environmental areas where air pollution levels exceed the World Health Organization standard limits [5]. Several technologies have been used for VOCs removals such as recycling, combustion, absorption, adsorption and biological treatment. Nevertheless, these techniques are still not applicable because of the formation of secondary pollutants or byproducts [6]. As a promising method to eliminate the VOCs compound, the heterogeneous photocatalytic oxidation (PCO) process has the advantage of oxidation of a substantial range of toxic VOCs with minimum energy consumption as well as less or no formation of by-products [7]. The PCO process can

---

* Corresponding author.

be used to oxidize organic compounds to harmless end products like carbon dioxide and water, which can be achieved at low temperature and pressure while using economical semiconducting materials, with a broad ability for oxidation of many different pollutants [8]. Extensive research has been focused on the preparation and fabrication of the materials for effective photocatalytic degradation of the VOCs. However, the design of photocatalytic oxidation reactors with higher degradation efficiency and capable of utilizing solar light remains a challenging factor that may add to the other factors during the photocatalysis process such as photocatalyst characteristics, concentrations, temperature, light intensity and temperature [9]. In addition, during the photocatalysis reaction, the photocatalyst should be: (i) photoactive, (ii) absorb and utilize near UV-light, (iii) chemically and biologically inert, (v) photostable and (iv) cost-effective. These properties can be matched with semiconductor materials like TiO_2 as photocatalyst [10]. In the past few decades, an organic semiconductor called graphitic carbon nitride (g-C_3N_4) has attracted much attention in this field [11].

The 2D g-C_3N_4 is a medium bandgap semiconductor with a bandgap energy of ~2.7 eV that may minimize the catalytic chemical process. However, due to lower conductivity and higher recombination rate between electrons and holes and the medium bandgap are the limiting factor. These could be overcome by modification of the g-C_3N_4 through hybridizing it with other well-matched energy levels of semiconductors or materials as cocatalysts forming a heterojunction with enhanced photo-redox properties [12]. Recently, the direct Z-scheme system has been recognized as the base for rational integration of coupled semiconductors that would narrow the bandgap of the two photocatalysts and rearrange the energy band structure. Additionally, the integrating g-C_3N_4 with other photocatalysts forming a direct Z-scheme system could enhance the photoexcited electrons/holes separation efficiency and promote the redox capacity of the component photocatalysts [13].

The g-C_3N_4 common composites consist of two components: g-C_3N_4 and semiconductors. During the photocatalysis under visible light irradiation, the photogenerated electron (e^-) in the conduction band reacts with O_2 to form superoxide radicals ($O_2^{\bullet-}$), while the photogenerated holes, h^+ react with H_2O to form hydroxyl radicals, $^{\bullet}OH$. These active radical species can react with the VOCs and degrade them to H_2O and CO_2 with long stability for the g-C_3N_4 photocatalyst or its composite [14,15]. Most of the reports indicated that the photocatalytic activity of g-C_3N_4 composite with heterostructure direct Z scheme is much higher than the single g-C_3N_4 material [16]. Such materials have been used in several applications of g-C_3N_4 composite photocatalysts including VOCs removal, H_2-production and CO_2 conversion. This review article provides an overview of the recent developments in the photocatalytic degradation of VOCs over photocatalytic materials.

2. Graphitic carbon nitride (g-C3N4) as a metal-free semiconductor

One of the unique materials that have interesting semiconductor properties is the mesoporous carbon nitride g-C_3N_4 with a high surface area and pore size distribution. Also, graphitic like carbon nitride g-C_3N_4 possess interesting structural, textural, optical and electrical properties. Therefore, metal-free materials have attracted many researchers worldwide since the first appearance of their citation in 2009 by Wang et al. [17,18]. But, the first preparation of this polymeric derivative was investigated by Berzelius and Liebig named in 1834 as (melon) using an old polymerization synthetic technique [19]. In 1989, Liu and Cohen prepared carbon nitride (C_3N_4) material through substitution reaction of silicon in β-Si_3N_4 with the carbon atom to form β-C_3N_4 material. Corkill and Cohen calculated the bandgap energy value of the same material in 1993. Later in 1996, Teler and Hemley proposed different allotropic structures of C_3N_4 such as α-C_3N_4, β-C_3N_4, cubic C_3N_4, pseudocubic C_3N_4, g-h-triazine, g-otriazine and g-h-heptazine (g-C_3N_4) [20,21]. The g-C_3N_4 carbon nitride has different structural forms including s-triazine-based orthorhombic structure, s-triazine based hexagonal structure and the most stable structure called tri-s-triazine (heptazine) as shown in Fig. 1 [21,22]. The material was not used as a photocatalyst until 2009 and Wang et al. [23] were the first to report the ability of g-C_3N_4 for utilization in the photocatalysis field.

Due to the photocatalytic properties of the graphitic carbon nitride (g-C_3N_4), it has been developed in the form of nanostructure to improve the large surface area and catalytic activity. The various morphologies of the g-C_3N_4 include; mesoporous, nanotube, nanospheres, nanorods, and hollow g-C_3N_4. These materials showed the ability of light absorption and scattering which also could be enhanced by modification of the graphitic carbon nitride [24]. The shape of the developed materials has a crucial effect on the surface area. Normally the materials have different dimensional structures such as zero-dimensional (0D), one-dimensional (1D), two-dimensional (2D) and three-dimensional materials (3D) and may combine with other materials that have the same or other dimensional structures. However, the two-dimensional (2D) structure has superior properties like a high surface area and more active sites [25].

The two-dimensional (2D) metal-free g-C_3N_4 has a large surface area with a medium bandgap (2.7 eV) and is thermally stable when compared to other structures. The tri-s-triazine building block of g-C_3N_4 allows the aromatic C–N bonds to extend the thermal stability that could reach up to 600°C in the presence of air [26]. Moreover, the g-C_3N_4 structure can form a π-conjugation plane that may bind to many other organic and inorganic materials to improve the reactive characteristics of the new composites [19].

The interesting properties of metal-free graphitic carbon nitride have attracted the attention of many researchers worldwide. Structural, optical and electrical properties of g-C_3N_4 lead to the direction for massive applications in research and development like photocatalysis, sensor and energy storage devices. The size, thickness, porosity, different composites and surface area features in g-C_3N_4 based photocatalyst has led to significant attention in environmental chemistry. The bandgap energy value of (E_g) of the monolayer g-C_3N_4 was calculated by Perdew–Burke–Ernzerhof (GGA-PBE) method and reported to be 1.2 eV. But, Heyd–Scuseria–Ernzerhof (HSE) predicted the

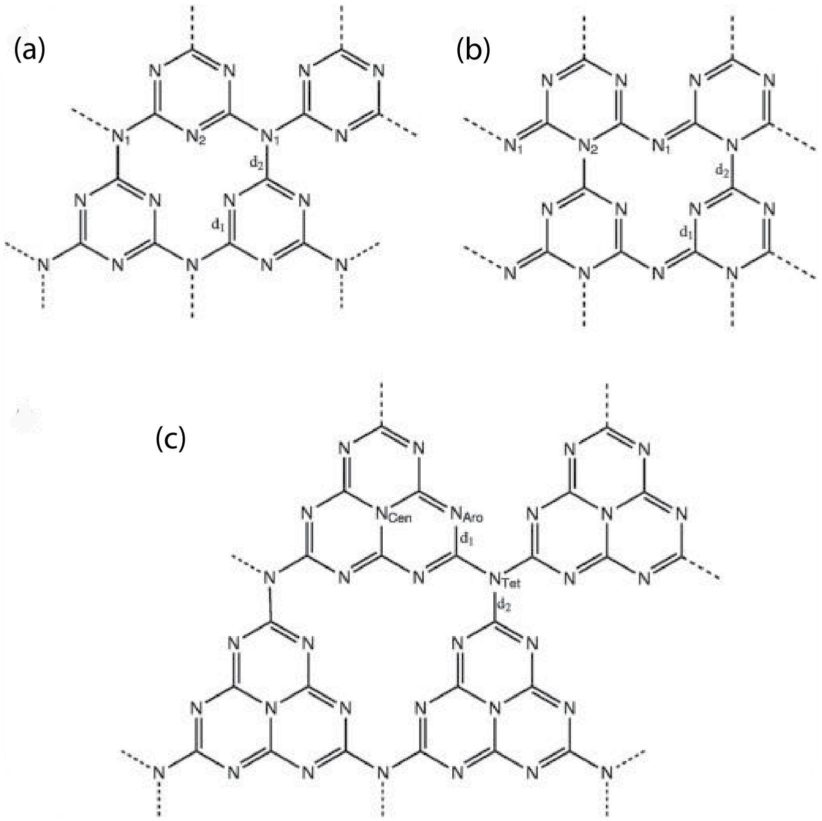

Fig. 1. Crystal structure phases of graphitic like carbon nitride g-C_3N_4: (a) g-hexagonal triazine, (b) g-orthorhombic triazine and (c) g-heptazine triazine [21].

bandgap energy accurately to be 2.7 eV for the graphitic carbon nitride g-C_3N_4 [21].

2.1. Photocatalytic process

In the basic mechanism of photocatalysis, the photons have a certain amount of energy (hν). The photonic bandgap is the range of frequencies in which photons are prohibited to pass through the crystal in any direction of spread [27]. In the photoactivated materials that have a bandgap (BG) lower than the absorbed photons, photons will activate the electrons (e^-) from the lower level of valance band (VB) to a higher level of the conduction band (CB). Hence, a hole (h^+) can be formed in the valance band (VB). The redox reaction takes place on the surface of the semiconductors allowing for the photocatalytic process to occurs. Fig. 2 illustrates the absorption of quantized light and the electron excitation on the photocatalytic process.

The photogenerated charge carriers (e^-/h^+) can recombine and release the absorbed energy in the form of heat as represented in the following equations [29]:

$$\text{Photocatalyst} + h\nu \rightarrow h^+_{(VB)} + e^-_{(CB)} \tag{1}$$

$$h^+_{(VB)} + e^-_{(CB)} \rightarrow \text{energy (heat)} \tag{2}$$

$$H_2O + h^+_{(VB)} \rightarrow {}^\bullet OH \text{ (hydroxyl radical)} + H^+ \tag{3}$$

$$O_2 + e^-_{(CB)} \rightarrow O_2^\bullet \text{ (superoxide radical)} \tag{4}$$

$${}^\bullet OH + \text{pollutant} \rightarrow \text{Intermediates} \rightarrow H_2O + CO_2 \tag{5}$$

$$O_2^{\bullet -} + \text{pollutant} \rightarrow \text{Intermediates} \rightarrow H_2O + CO_2 \tag{6}$$

The effect of the charge recombination between electron-hole pairs minimizes the efficiency of the photocatalytic process [30], due to the fact that recombination of charge carriers reduces the lifetime of charge carriers, utilization of visible light and photoexcitation as well [26].

The medium bandgap of g-C_3N_4 semiconductor with a yellow color and absorption capacity up to 460 nm has opened up lots of interest for harvesting the solar light. Moreover, the thermal stability and chemical unique properties in the aqueous phase permitted continuous research of this material [31]. Furthermore, the wide research to improve the utilization of solar energy by increasing the surface area, charge carrier separation and creation of more reactive sites promotes graphitic carbon nitride g-C_3N_4 to be used as promising photocatalysts [32]. The photocatalytic activity is controlled by the gap between the lowest unoccupied molecular orbital (LUMO) and the highest occupied molecular orbital (HOMO). A unit of six repeated g-C_3N_4 might be the smallest unit that fulfills the limitation in its LUMO-HOMO gap [33]. However, the surface of g-C_3N_4 can be modified to be as a bulk 3D, nanosheets or films 2D, nanorods or nanowires 1D and quantum dot 0D [34]. Practically, the two-dimensional layered structure is interesting to be hybridized with other compounds and enhance the light efficiency of the g-C_3N_4 [35].

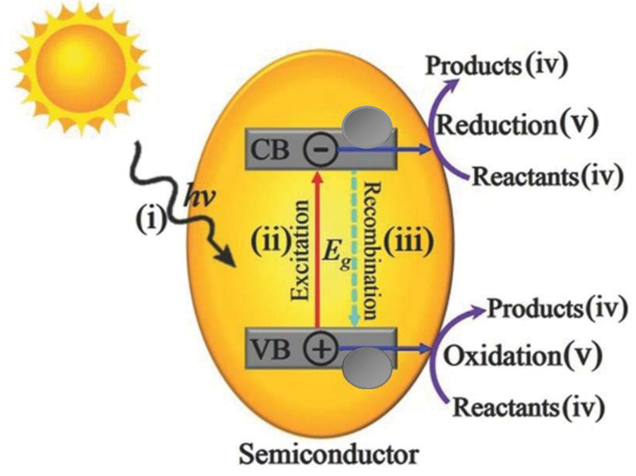

Fig. 2. Redox reaction on the semiconductor surface [28].

2.2. Preparation of graphitic carbon nitride g-C_3N_4

Graphitic carbon nitride g-C_3N_4 can be prepared by many techniques including thermal polymerization, microwave irradiation and hydrothermal methods with nitrogen-rich precursors such as melamine, urea, thiourea, cyanamide and dicyandiamide (DCDA) [36]. These precursors are usually used to prepare bulk g-C_3N_4 with the surface area below 10 $m^2 g^{-1}$ by thermal condensation. The physicochemical properties such as surface area, pore size and light absorption could be intensively influenced by treatment methods. Lin Tang et al [37], prepared g-C_3N_4 yellow powder from heating melamine precursor at 500°C for 3 h at a rate of 2°C/min. After cooling and grinding, it was subjected to calcination at 550°C for 2 h at a rate of 2°C/min. The melamine converted to graphitic-like C_3N_4 sheets at 550°C and decomposed after additional heating at 700°C. The various preparation methods for graphitic carbon nitride including the preparation temperature, bandgap and specific surface area are described in Table 1.

Preparation of g-C_3N_4 with inorganic semiconductors to make a nanocomposite has also attracted much interest in photocatalytic research. The coupling of metal-free g-C_3N_4 and metal oxides show superior properties in gas sensing compared to the pure g-C_3N_4, since the metal element would capture and store the electrons from the conduction band of g-C_3N_4. Moreover, it prevents electrode passivation that results from a high-energy electron inserted into the conduction band of g-C_3N_4 during the photocatalytic process. Furthermore, the metal nanoparticles have a high surface area, long stability and could be recycled several times in the catalytic reaction [55].

3. Preparation of g-C3N4 based hetero-composites

The specific surface area could be enhanced by changing the morphological structure during the preparation method. Mesoporous g-C_3N_4 with a surface area up to 350 $m^2 g^{-1}$ was reported [56]. This could be accomplished by coupling g-C_3N_4 with other materials such as transition metal oxides (TiO_2, ZnO_2, CuO_2, Fe_2O_3) and semiconductors like $LnVO_4$ (Ln = Sm, Dy, Bi, Gd, La), CdS and AgX (where X = Cl, Br or I) which improves structural properties and photocatalytic activity [57]. The synthesis of graphitic carbon nitride g-C_3N_4 could be classified into two types: top-down and bottom-up. In the top-down method, the larger components are divided into smaller units. This strategy includes liquid exfoliation, liquid ammonia-assisted lithiation and thermal exfoliation methods. In the bottom-up method, the smaller units are segregated into complex structures [58]. The increase in the surface kinetics of the graphitic like carbon nitride (g-C_3N_4) and charge separation competence would enhance the photocatalytic activity. Nanosheets of g-C_3N_4 doped with Br and Cl could be prepared by one-step exfoliation using melamine and ammonium as precursors for the graphitic carbon nitride (CN) and gas template. The coupled composite improves the absorption in the visible light and the charge carriers rate with the electron–hole separation [59].

3.1. Hydrothermal method

The hydrothermal method is one of the efficient and costly effective techniques for the preparation of g-C_3N_4 based hetero-composites and produces high purity nanocomposites. This can be attributed to the valance defects while modifying the electronic structure by introducing extra energy levels, which target the charge carriers and enhances the photocatalytic activity of the materials. Hao et al. [60], reported that ZnS/g-C_3N_4 heterostructure prepared by hydrothermal route possessed long absorption in the visible region with enhanced photoinduced electron–hole separation capacity. In another study, Yao et al. [61] developed a hybrid CdZnS@g-C_3N_4 composite for hydrogen generation. The uniform dispersion of the CdZnS quantum dots over the 2D nanosheets of g-C_3N_4 enhanced the reduction of electron-hole recombination and improved the photocatalytic properties. Moreover, Zhang et al. [62] stated that g-C_3N_4 was well incorporated with mesoporous phosphate to make a covalent bonding with the amino group and the synergic advantage increased the surface area and reduced the recombination of charge carriers which leads to high catalytic activity.

3.2. Microwave method

The microwave method consists of digesting the matrices at boiling point in Teflon vessels with microwave radiation for a certain period. This method describes effective synergy between components such as $KBIO_3$ and g-C_3N_4 by facilitating these dispersions and binding for the two materials through the microwave route [63]. Akhundi and Habibi-Yangjeh et al. [64] prepared g-C_3N_4/Ag_2SO_4 nanocomposites with high visible-light photocatalytic activity and matching band energies for both materials by rapid microwave-assisted technique. Furthermore, a ternary Ag/ZnO/g-C_3N_4 micro/nanocomposites were prepared by the same method for the photocatalytic process under visible

Table 1
Graphitic carbon nitride g-C_3N_4 precursors and preparation method, surface areas and bandgaps

No.	Precursors	Preparation methods	Preparation temperature (°C)	Bandgap (eV)	Specific surface area ($m^2\ g^{-1}$)	Ref.
1	Melamine	Air assist	420	2.87	6.0	[38]
		Thermal polymerization and etching	500	2.85	41.5	
		Thermal condensation	500	2.83	7.1	[39]
			550	2.78	8.6	
			600	2.71	11.7	
			650	2.74	46.8	
		Heating melamine treated with sulfuric acid	600	2.69	15.6	[40]
		Oxygen post calcination	550	2.67	22.6	[41]
		Heat treatment	550	2.72	N/A	[42]
2	Urea	Rapid and facial solution combustion process	450	2.76	135.6	[43]
		Pyrolysis reaction condition	N/A	2.73	69.6	[44]
		Pyrolysis under ambient pressure	550	2.85	N/A	[45]
		Facial template free method	550	2.78	288	[46]
		Ammonia etching treatment	550	2.88	149	[47]
		Thermal polymerization	600	2.85	43.8	[48]
3	Thiourea	Facial one-step pyrolysis	N/A	2.60	11.3	[45]
		Direct heating	450	2.71	11	[49]
		Thermal polymerization	550	2.60	11.3	[44]
		Heating	600	2.75	18.5	[48]
4	Cyanamide	Thermal polycondensation	550	2.7	10	[50]
5	Dicyanamide	Facial one-step pyrolysis	N/A	2.66	12.3	[45]
		Direct heating	550	2.75	10	[49]
		Pyrolysis reaction condition	N/A	2.66	12.3	[44]
		Thermal polymerization	600	2.75	12.8	[48]
6	Thiosemicarbazide mixed with melamine, urea, thiourea and trithiocyanuric acid	Mixture blending polymerization to make polymeric carbon nitride film	500	2.75	N/A	[51]
7	Ammonium thiocyanate	Thermal polymerization	550	2.62	9	[52]
8	Guanidine hydrochloride	Thermal-induced polymerization	500	2.75	8.21	[53]
			550	2.70	16.08	
			600	2.83	53.36	
			650	2.88	65.08	
9	Guanidine thiocyanate	Thermal-induced desulfurization and polymerization	450	2.82	5	[54]
			500	2.78	6	
			550	2.74	8	
			600	2.70	16	
			650	2.81	31	
			700	2.89	42	
10	Trithiocyanuric acid	Heat treatment to prepare sulfur doped g-C_3N_4	550	2.50	72.8	[42]

and solar light. The ternary composites showed an excellent absorption of visible light and high photocatalytic activity attributed to the surface extension with advantages of electron-hole separation and effective transfer of charge carriers [65]. Moreover, N-TiO_2/g-C_3N_4 composites developed by microwave techniques exhibited a structural porosity and a large surface area that resulted in a higher contact area. The functionality of the heterojunction between the N-TiO_2 and the g-C_3N_4 improved the photocatalytic activity and reduced the electron-hole recombination [66].

3.3. Solvothermal method

Solvothermal synthetic method is defined as a wet chemical reaction occurring in a solvent at temperatures higher than the boiling point of the solvent and pressure above 1 bar. The solvents used in the solvothermal method are organic solvents such as alcohols or inorganic solvents [67]. If non-aqueous solvents are used as the reaction intermediate, it is called the solvothermal method. Li et al. [68] synthesized a nanoflower morphology of MoS_2 that could build up on pyridine-modified graphitic carbon nitride (g-C_3N_4-Py) prepared by the solvothermal route. The successful coupling of heterostructure MoS_2/g-C_3N_4-Py composites showed a superior visible light absorption, charge carrier transfer and optimum photocatalytic performance for hydrogen production. Besides, Chen et al. [69], reported a novel fabrication of carbon, nitrogen-doped titanium oxide nanoparticles (C, N–TiO_2 NPs) over graphite-carbon nitride nanosheets (g-C_3N_4) via solvothermal preparation method. The designed composite showed a higher ability for hydrogen generation compared to pure single g-C_3N_4 or C, N-TiO_2 nanoparticles. In addition, a two-dimensional graphitic carbon nitride structure (g-C_3N_4) hybridized with TiO_2 core-shell composite of TiO_2/g-C_3N_4 was prepared by the same method. The composition showed improved surface area, higher light absorption and enhanced photocatalytic activity compared to the individual single TiO_2 or g-C_3N_4 [70]. A mesoporous Nb_2O_4 microstructure was effectively grown on the graphitic carbon nitride nanosheet surface forming g-C_3N_4/Nb_2O_5 nanocomposites with high specific surface area and adequate contact in heterostructure leading to enhance photocatalytic activity [71]. The solvothermal process is an effective route to fabricate nanomaterials through speed up the reaction process by boosting hydrolysis, crystal polymerization and operative synergy of g-C_3N_4 composite in the solution media.

3.4. Sol–gel method

The sol–gel method is a promising chemical synthesis technique for obtaining the good structure of the nanomaterials. Usually, the starting precursor is the colloidal solution (sol) of an alkoxide of an inorganic salt. Then, the precursor undergoes a condensation reaction, which results in a polymeric network containing the solvent in the form of a gel. For example, a different ratio of g-C_3N_4-TiO_2 hybrid prepared by sol–gel method to form heterojunction composites resulted in components with well-matched bandgap structure, appropriate specific surface area and enhanced optical properties [72]. Furthermore, Li et al. [73] reported a similar technique for the synthesis of composites for methylene blue photodegradation. The smaller grain size and matching bandgaps were the two key features for the enhancement of photocatalytic degradation. Likewise, composites of g-C_3N_4/TiO_2 composite were fabricated by the same method for catalytic degradation of Methyl orange (MO). The prepared photocatalyst g-C_3N_4/TiO_2 exhibited poor performance after coupling due to reduced light absorption and photoinduced electron–hole pairs [74]. Usually, the sol–gel route is used for the synthesis of composited by doping nanoparticles on the surface of semiconductors which makes it a promising method. Furthermore, it is classified as an advanced common technique compared to other methods due to the low cost, easy processing, high homogeneity and purity of products.

4. Modification of g-C3N4

4.1. Doping of non-metals with g-C_3N_4

This method has been used to prepare g-C_3N_4 nanocomposite with enhanced photocatalytic properties. For example, the post-calcination method is required for changing the material's phase by heating at a high temperature at a slow rate. Xiao et al. used the post-calcination method to decorate the g-C_3N_4 surface by P–N bond formation that acts as an impurity for electron capture to enhance the active sites [75]. Another method used a facile oxidation technique to prepare a porous g-C_3N_4 for hydrogen production. The effectiveness of the thermal oxidation treatment demonstrated that the BET-specific surface area of modified g-C_3N_4 increased to 7.08 times compared to pristine g-C_3N_4. Moreover, the temperature treatment up to 530°C for the pristine g-C_3N_4 gave about (1,430.1 μmol g^{-1} h^{-1}) hydrogen photocatalytic activity [76]. Furthermore, sulfur-doped graphitic carbon nitride (g-$C_3N_{4-X}S_X$) modified by the conventional approach enhanced the photoactivity for hydrogen evaluation to about 8 times more than undoped g-C_3N_4. The homogenous distribution of sulfur particles triggered shifting of the valance band for higher visible light absorption [77]. Moreover, a non-metal bromine and fluorine co-doped graphitic carbon nitride to form (g-C_3N_4-B/F) composite was obtained by using post-thermal treatment. The material displayed a compact interlayer and higher surface area after coupling with boron and conjugating the aromatic ring at the surface of g-C_3N_4, which resulted in a polymeric structure with a generated photolytic property [78]. Bellardita et al. [79] used a thermal condensation method for partial inclusion of phosphorus (P) in the d-C_3N_4 network. The presence of P in the g-C_3N_4 significantly enhances the selectivity towards aldehyde degradation. In addition, an active metal-free red phosphor r-P coupled with graphitic carbon nitride was prepared by the solid-state annealing method. The hetero-composite r-P/g-C_3N_4 exhibited a higher separation for photogenerated electrons and holes which improved the photocatalytic activity of CO_2 conversion to CH_4 fuel and H_2 production [80]. Table 2 illustrates some advantages and disadvantages of the preparation methods of graphitic carbon nitride composites.

4.2. Preparation of noble metal doped g-C_3N_4

Graphitic carbon nitride (g-C_3N_4) has interesting photocatalytic properties, that can still be enhanced by doping with other metals such as Au, Pt and Pd. Noble metals have been doped with the g-C_3N_4 as an impurity to reduce the electron–hole recombination during the photocatalytic process. One of the techniques that are used to form hybrid composites of inorganic and organic materials is

Table 2
Advantages and disadvantages of the preparation methods

Preparation methods	Advantages	Disadvantages	Ref.
Chemical vapor deposition	Maintaining the high purity of the material	Difficult to maintain altitude and sustained pressure	[81,82]
Microcontact printing techniques	Easy to possess and low cost	Limitation in micro size	[83]
Facial calcination method	Improve the mechanical properties of the samples	Need carful examined and difficult to control the crystal transition process	[84]
One-step hydrothermal method	Large accessible surface area, multi electron transport and less diffusion	Difficult to notice the sample change phases and growth	[85]
Facial solid-state method	Large surface area with high chemical stability flexibility of the sample	Long processing and need many equipment requirement	[86]
Ultrasound-assisted liquid-phase exfoliation method	Provide multi-size pores in order to fast transportation of reactants to electroactive sites	Analysis of structural morphology is demanding to specific regulation	[87]
The sample vacuum filtration method	High purity and flexibility of the samples	Limited sample conditional preparation and highly equipment are high	[88]
Metal blending method	The synergetic distribution effect between different hybrids is easier to image	Difficult to control the sample morphology	[89]
Facile hydrothermal method	Uniform dispersion and high purity sample	Not easy to observe the growth preparation of sample at high ratio	[90]

called the deposition–precipitation route. The precipitation process takes place in a solid form of the solution depending on the settling force to collect the particles. Then, the second process of deposition starts with the interaction of the precipitate particles with the support surface [91]. Gold particles were deposited on the graphitic carbon nitride g-C_3N_4 to form Au/g-C_3N_4 nanocomposite for hydrogen gas evaluation by deposition–precipitation route. The product showed enhanced photoactivity of about 23 times higher than pure g-C_3N_4 [92]. Moreover, a bimetallic alloy nanoparticle doped with graphitic carbon nitride to form Pt Pd/g-C_3N_4 photocatalyst composite was also synthesized by the same method. The co-catalyst showed a synergetic effect, suitable stability and higher activity for the hydrogen production rate when compared to the single g-C_3N_4 [93]. Similarly, Pd-Ag noble bimetallic nanoparticles coupled with g-C_3N_4 nanosheets by chemical reduction method were developed. The optimized loading of the noble metals in the Pd Ag/g-C_3N_4 composite demonstrated effective separation of electrons-holes charge carriers (e/h) and increased the photocatalytic hydrogen generation to about 3.43 mmol h^{-1} g^{-1} [94].

4.3. Preparation of transition metals and metal oxides doped g-C_3N_4 binary composites

Although noble metal doped graphitic carbon nitride showed interesting photocatalytic properties and activity, the economic factor due to their cost has resulted in researchers trying to find other alternatives which are more efficient and economic. Transition metal oxides are promising materials due to their abundance in nature, cost-effectiveness and could be used to improve the structural performance of g-C_3N_4. Ahmed et al. [95] fabricated a combination of the α-Fe_2O_3 nanotube with tubular g-C_3N_4 by electrostatic self-assembly method. The photoelectrochemical measurements of (Fe_2O_3 nanotube/g-C_3N_4 tubule) of the composite expressed higher charge separation of photogenerated charges which can be resulted from the heterostructure combination of both materials. In another report, a α-F_2O_3 coupled with g-C_3N_4 to form a direct Z-scheme hybrid was synthesized through one-step solvothermal synthesis. The metal oxide-based photocatalyst composites displayed a significant photocatalytic reduction of CO_2 with rates up to 27.2 μmol g^{-1} h^{-1}, because of narrowing of the bandgap and increasing the optical energy from the reduction reaction [96]. Furthermore, the solvothermal method was used to prepare a composite of g-C_3N_4/α-Fe_2O_3 microspheres. The morphology of the hybrid materials shows a homogenous crystallinity, low electronic resistance and large BET surface area [97]. Besides, a hydrothermal method was used to prepare a composite of α-Fe_2O_3/g-C_3N_4 (FCN) as a photocatalyst for CO_2 reduction to produce methanol. The heterojunction structure in FCN offered high utilization of visible light and separation of photogenerated charge carriers due to the presence of α-Fe_2O_3 which narrowed the bandgap and improved the catalytic activity [98].

Titania (TiO_2) is a very well-known photocatalytic material that has been used in many researches in the past few decades. Xiao et al. [99] fabricated the mesoporous structure of TiO_2/g-C_3N_4 material through a thermal condensation process. The composite revealed a large specific surface area up to 268 m^2 g^{-1} with high reducibility and performance. In another report, the same composite nanostructure prepared by the one-step vapor deposition method showed promising visible light absorption for H_2 evolution that reached 10.8 times more than pristine g-C_3N_4 [100]. Likewise, a graphitic carbon nitride g-C_3N_4 and TiO_2 coupled by facile calcination method to form macro/mesoporous g-C_3N_4/TiO_2 hetero-composite (CNT) was developed. The heterojunction material demonstrated a higher surface area, narrow bandgap and interesting photocatalytic performance for decomposition of Rhodamine B when compared to single g-C_3N_4 or TiO_2 [101].

In another study, copper oxides and zinc oxide were used as hydride candidates to form a composite with g-C_3N_4 nanosheets. A core-shell heterostructure Cu_2O@g-C_3N_4 photocatalyst was prepared by solvothermal and chemisorption method for H_2 production application. The characteristic performance showed that at 5 wt%, the composite produced 796 μmole g^{-1} of hydrogen gas which was 4 times more than that of pristine Cu_2O [102]. Dongya et al. [103] developed a composite of g-C_3N_4/Cu_2O with p-n heterojunction by hydrothermal route combined with high calcination temperature. The specific surface area of the material increased after the addition of glutamate, which regulated the morphology of the heterostructure and reduced the charge recombination rate during the photocatalytic process. Furthermore, g-C_3N_4 was coated onto Cu_2O nanospheres to form Cu_2O@g-C_3N_4 core-shell composite by solvothermal and chemisorption method. The composite exhibited a significant increase of H_2 evolution at a content of 5 wt% compared to pure Cu_2O or g-C_3N_4 [104]. Pan-Yong et al. [105] prepared a heterostructure g-C_3N_4/ZnO nanorod arrays through electrochemical deposition and thermal condensation methods. The composites showed enhanced structure characteristics with high photocatalytic performance. In addition, the same compound with type II heterojunction achieved by light-assisted method and g-C_3N_4/ZnO composite offered greater stability until 5 cycles of photocatalytic H_2 production in the visible light region [106].

4.4. Preparation of ternary composite of g-C_3N_4

Most of the mesoporous structures are formed by the heterojunction of pure g-C_3N_4 combined with high conductive materials such as graphene or carbon nanotube. In addition, it could be structured with many semiconductors to boost photocatalytic activity. A ternary composite of g-C_3N_4, ZnO and ethyl cellulose to form OEC/g-C_3N_4/ZnO was fabricated by the polymerization and hydrothermal method. The prepared composites had high specific surface area, stability, lifetime and outstanding catalytic activity for methylene blue degradation [107]. Furthermore, ZnO nanospheres, g-C_3N_4 and graphene oxide was prepared to form a ternary composite of three materials by the co-precipitation method. The ZnO nanospheres improve the electronic properties of the composite which enhances visible light absorption. Also, the graphene oxide (GO) improved the photocatalytic activity, stability, charge transportation and separation in the ternary composite ZnO-g-C_3N_4/GO [108]. Moreover, a ternary composite of g-C_3N_4/ZnO@α-Fe_2O_3 photocatalyst was prepared by direct pyrolysis and sol–gel method. The nanocomposite illustrated excellent photocatalytic degradation of tartrazine dye (Acid Yellow 23) than simple g-C_3N_4, ZnO and ZnO@α-Fe_2O_3 [109].

Even though the g-C_3N_4 has many advantages such as electronic bandgap, easy processing, economical cost and environmental friendliness, however pure g-C_3N_4 has many drawbacks including limiting the visible light utilization, low specific surface area and rapid charge carrier recombination. To overcome this problem, the scientist tried to reconstruct the materials by heterostructure of g-C_3N_4 with other materials. The g-C_3N_4 based heterojunction may improve the efficiency to utilize the visible light photocatalysis which is reflected in environmental applications. The heterostructure of g-C_3N_4-based photocatalysts could be classified as type II heterojunction, Z-scheme, p-n heterojunction, g-C_3N_4/metal heterostructure and g-C_3N_4/carbon heterostructure [110]. As the g-C_3N_4 shows semiconductor properties, the heterostructure depends on the bandgap and electronic affinity. Heterostructure semiconductors could be classified into three types: type-I, type-II and type-III as shown in Fig. 3. The two semiconductors could form type-II band alignment heterojunction if the position of valance bands of semiconductor 2 is higher than semiconductor 1, and the process in the conduction band and valance band follow the same direction. In another word, the potential difference between 1 and 2 semiconductors would produce a band bending at the heterojunction, which photo-stimulates to build a field leading to movement of electron–hole in opposite direction without recombination. Therefore, the formation of type-II heterojunctions enhanced the charge carrier separation and improved the photocatalytic activity. In addition, the UV-active semiconductors like TiO_2 and ZnO_2 could be coupled with other visible light active semiconductors [111].

5. Methods for structural characterization of g-C3N4

The characterization methods are principally focused on two important factors, which include structural characterization and performance characteristic properties. Fig. 4a shows the X-ray diffraction (XRD) pattern of the g-C_3N_4, and Fig. 4b demonstrates the infrared (IR) absorption peaks at 3,363.56 cm^{-1} attributed to NH_2 in the same material. Moreover, the IR peaks at 1,271.09 cm^{-1} for the C–N bonds and the sharp peaks at 1,617.95 cm^{-1} indicate the crystallinity of g-C_3N_4.

Fig. 5a shows the powder XRD pattern of the two phases of graphitic carbon nitrides of the tubular carbon nitride structure with the two peaks at about 27.4° and 17.4°, whereas Fig. 5b shows the XRD pattern for the pristine g-C_3N_4 showing the intensive peaks at about 27.4°. However, the same XRD analysis for different precursors such as melamine (MCN), urea (UCN) and thiourea (TCN) to form graphitic carbon nitride showed the same strong peaks at $2\theta = 27.4°$, which is caused by the interlayer aromatic system and second weak peak at $2\theta = 13.1°$, is attributed to the in-plane structure of the triazine units. The high intensity of the peak of the g-C_3N_4 in case of melamine precursor (MCN) is due to the formation of more crystallinity product in contrast to the other precursors [114]. Yuewei et al. [44] reported that during the polymerization process of urea, thiourea and dicyanamide, they would change to melamine before the formation of graphitic carbon nitride. According to transmission electron microscopy (TEM)

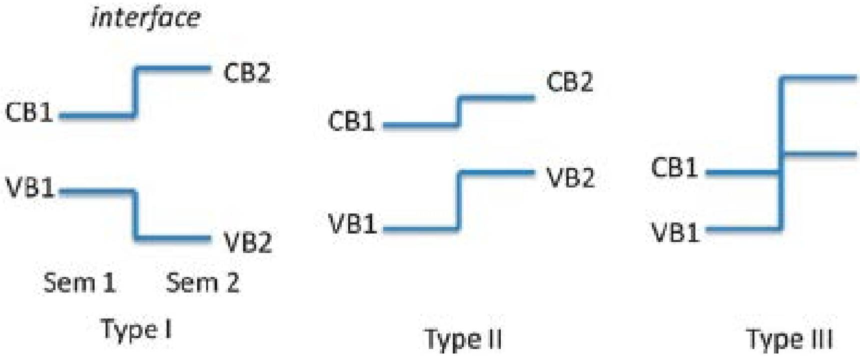

Fig. 3. Schematic diagram of three types of heterojunctions in semiconductors [111].

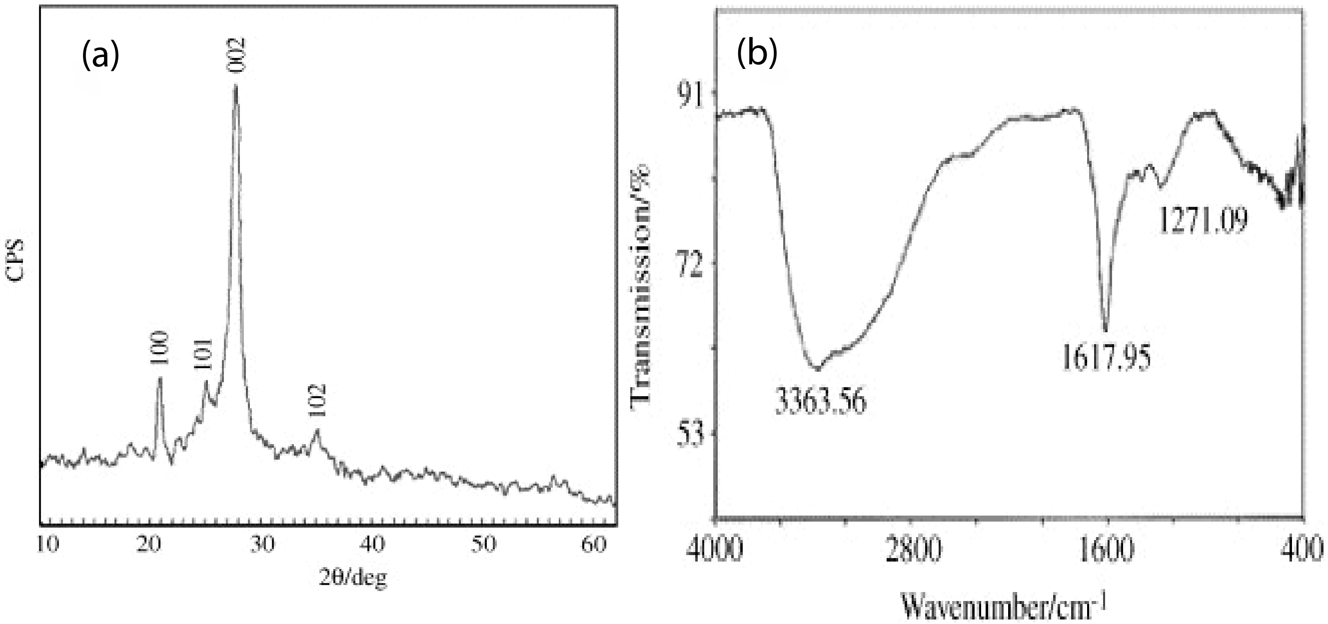

Fig. 4. (a) X-ray diffraction pattern and (b) IR spectrum for the graphitic carbon nitride [112].

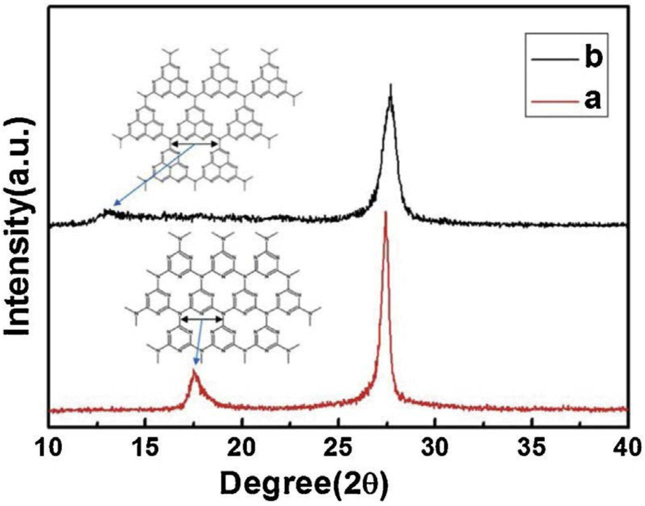

Fig. 5. XRD pattern of (a) tubular carbon nitride and (b) the bulk g-C_3N_4 [113].

images in Fig. 6, the pore size of the g-C_3N_4 that comes from TCN and UCN are larger than that of the melamine (MCN) precursor. However, experimentally, the yield obtained from MCN is higher than the other two for the same amount of all three precursors.

5.1. Optical and surface properties of g-C_3N_4

Carbon nitride is a medium bandgap semiconductor material and since both HOMO and LUMO positions are exciting, the electrons have more potential to transfer [116]. In order to study the optical features for the precursors MCN, TCN and UCN, a UV-Vis diffuse reflectance spectroscopy (UV-DRS) were used. Fig. 7a represents the absorption edge and the corresponding photon energy is shown in Fig. 7b for the samples prepared from the different precursors. Bandgap estimation from the Tauc plot was observed to be about 2.70 eV for TCN and MCN and 2.67 eV for UCN. On the other hand, Fig. 7c confirmed the liquid N_2 adsorption–desorption analysis and pore size distribution curves.

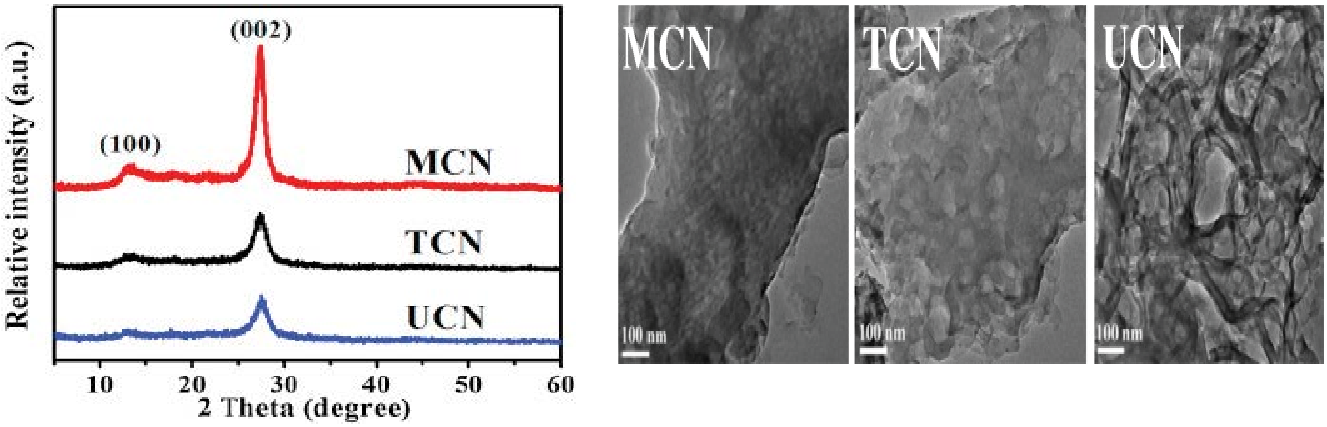

Fig. 6. Powder XRD pattern and the TEM images of the MCN, TCN and UCN [115].

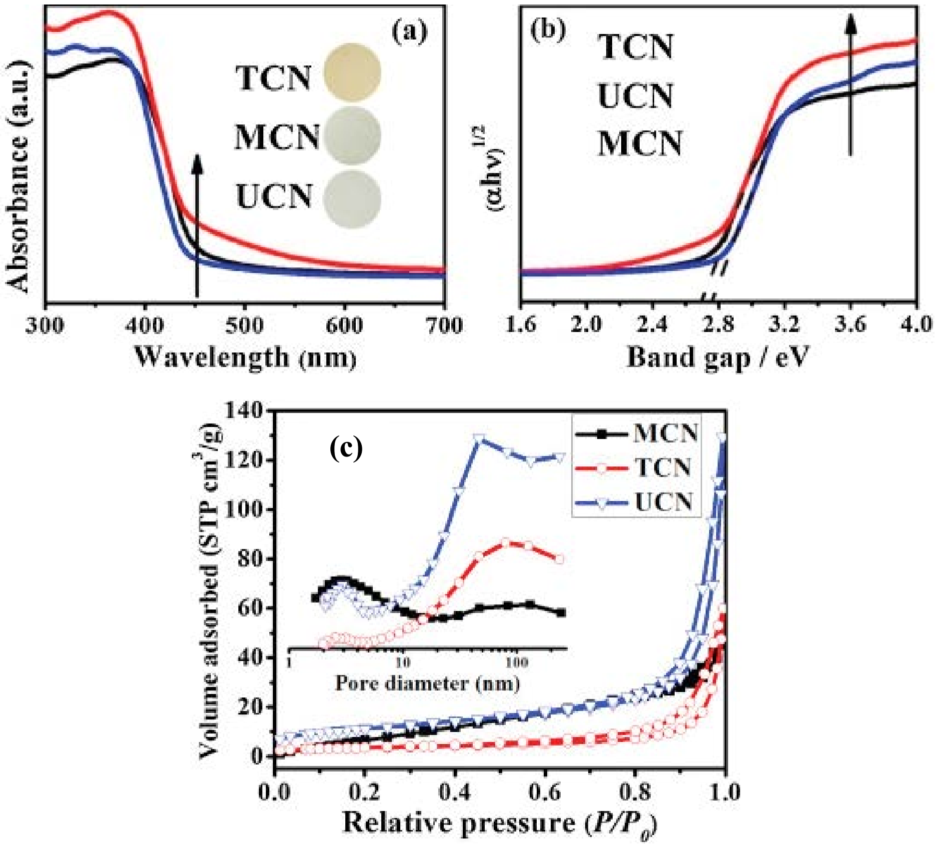

Fig. 7. (a) UV-Vis DRS, (b) plot of $(\alpha.h.\nu)^{1/2}$ vs. photon energy and (c) N_2 adsorption–desorption isotherm and pore size distribution Barrett, Joyner, and Halenda curves for UCN, TCN and MCN [115].

All three samples showed mesoporous structure according to type-II isotherm with H_3 hysteresis loop.

In another report, g-C_3N_4 nanosheets were prepared from melamine via the thermal oxidation etching method [117]. The bulk and nanosheets of g-C_3N_4 were studied by energy-dispersive X-ray spectroscopy (EDX) and scanning electron microscopy (SEM) measurement as present in Fig. 8. A sheet structural morphology of g-C_3N_4 appears to be smoother and softer than the bulk as shown in Fig. 8c.

5.2. Graphitic carbon nitride composites as photocatalysts

5.2.1. Advance oxidation process (AOP)

Advanced oxidation processes (AOPs) are the methods performed at room temperature and are based on in-situ generation of powerful oxidizing agents like hydroxyl radicals (•OH) at an adequate concentration to effectively oxidize pollutants [118]. Based on the source of the production of hydroxyl radicals, AOPs could be

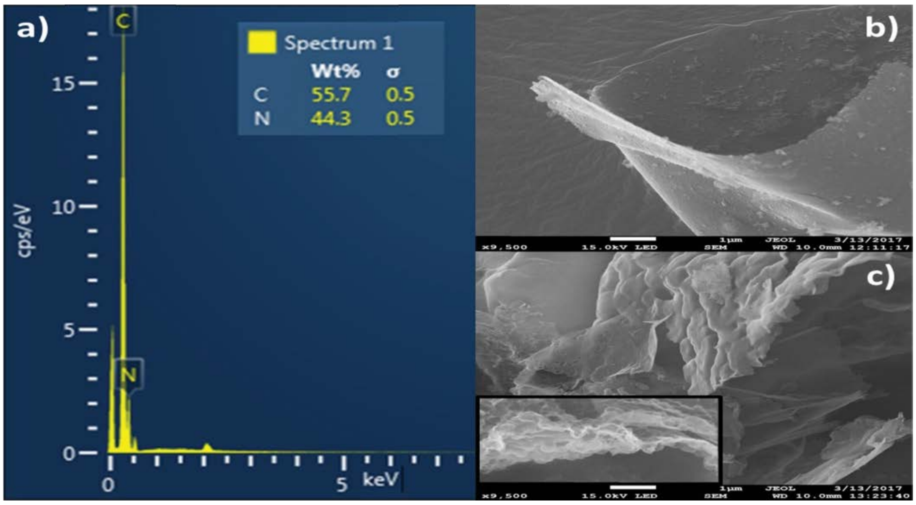

Fig. 8. (a) EDX spectrum of the g-C_3N_4 nanosheet, SEM images of g-C_3N_4 (b) bulk and (c) nanosheets [117].

classified as chemical, photochemical, sonochemical and electrochemical processes [119]. Ultraviolet (UV) irradiation is used in photochemical AOPs to degrade wastewater through coupling with a strong oxidant such as ozone (O_3), hydrogen peroxide (H_2O_2) and catalysis with Fe^{3+} or TiO_2. A photolysis process is a chemical process in which chemical bonds are broken by the transfer of light energy either direct or indirect to these bonds [120]. Recently, solar energy has been used as a free renewable energy source for the degradation of pharmaceutical waste. Solids that can promote reactions in the presence of light and are not consumed in the overall reaction are referred to as photocatalysts and should be: (1) photoactive, (2) chemically and biologically inert, (3) photostable (anti photo corrosion), (4) inexpensive, (5) non-toxic [121]. In the conducting band (CB), the redox potential of the photogenerated electrons must be adequately negative to be able to reduce adsorbed O_2 to superoxide [122].

5.3. Volatile organic compounds

There are many definitions for the VOCs and are similar with a little change. VOCs are organic compounds, with a vapor pressure of about 10.3 Pa at normal temperature (293.15°K) and atmospheric condition (101.325 kPa). It has a large group of carbon compounds that is easily evaporated [123]. VOCs are one kind of air pollutants with boiling points ranging from 50°C to 260°C at room temperature and under atmospheric pressure [124]. The World Health Organization recommended the temperature range from 240°C to 260°C for VOCs [125]. According to the United States Environmental Protection Agency (US EPA), it is defined as a substance that has a vapor pressure of more than 0.1 mm Hg. The Australian National Pollutant Inventory (NPI) defines VOCs as any chemical based on carbon chains or has a ring with a 2 mm Hg vapor pressure at 25°C. The EU defined VOCs as chemicals with 0.074 mm Hg vapor pressure at 20°C.

There are many examples of VOCs such as alcohols, aldehydes, ketones, alkenes and many other aromatic compounds. VOCs emissions originate from different sources such as refining oil, material production, pharmaceutical industry, pesticide manufacturing, transport and fuels usage [126]. As a result, an accumulation of these pollutants takes place in the soil, water and air. The extending effects to the ecosystem and environment have caused a growing concern about the potential toxicity and carcinogenicity of the VOCs [127]. As a result, finding solutions to solve these challenges will be very critical to save the nature and environment. Today, there are many techniques to remove VOCs such as adsorption and photocatalytic degradation of VOCs [2]. However, the cost of treatments and the sustainability of the processes are the most important challenges facing the remediation of VOCs. Reduction methods were used to minimize the impact of VOCs emission and could be classified into two main types. First, non-destructive or recovery routes like the use of membrane separation and condensation process. The second method is the destructive route using a technique such as photocatalytic oxidation, ozone catalytic oxidation and biological degradation. Among all of these methods, the photocatalytic degradation and adsorption method is the top effective routes, due to the low energy consumption and use of renewable environmentally friendly resources [128]. Solar light is one of the abundantly available renewable sources of energy that can be used to activate photocatalytic materials and add to the sustainable use of natural resources. The shortage of photocatalysts with maximum quantum efficiency in the visible light range may inhibit the real-life application of photocatalysis. The preparation of photocatalysts with a broad light absorption range, high charge carrier separation and low deactivation will be an innovative method to improve the quantum efficiency of the catalysts using readily available energy sources [129]. Table 3 illustrates some common VOCs and their sources and properties.

5.3.1. Indoor VOCs

Indoor volatile organic compounds are carbon compounds that contain organic chemicals coming from the

Table 3
Types, sources and properties of the volatile organic compounds [124–126]

VOCs	Boiling point (°C)	Vapor pressure (kPa)@T	Sources
Aliphatic hydrocarbons			
Ethane	–88.5	–	Automobile exhaust Asphalt application Biomass combustion Petroleum refinery Agricultural products Chemical processes
Propane	–42.09	1,306.46 (20°C)	
Butane	–0.5	106.39 (0°C)	
n-Hexane	69	15.96 (20°C)	
n-Heptane	98.42	4.98 (21°C)	
Ethylene	–103.9	–	
Propylene	–47.4	101.08 (–47°C)	
Acetylene	–84	4,460 (20°C)	
1,3-Butadiene	–4.4	245.31 (21°C)	
Aromatic hydrocarbons			
Benzene	80.1	22.9	Coal combustion Automobile exhaust Petroleum refinery Architectural materials
Toluene	110.6	2.66 (18°C)	
Meta-xylene	139.2	1.33 (28°C)	
Para-xylene	138.2	1.33 (27°C)	
Ortho-xylene	142.8–145	1.33 (32°C)	
1,2,4-Trimethylbenzene	168	0.65	
Styrene	146	1.26 (28°C)	
Halocarbons			
Dichloromethane	40	58.52 (25°C)	Waste materials from water purification and evaporation Industrial processes
Trichloromethane	61.3	13.30 (10°C)	
1,2-Dichloroethylene	60.2	23.94–35.24 (20°C)	
1,2-Dichloroethane	83.5	13.33 (29°C)	
Trichloroethylene	87.2	10.27 (25°C)	
Chlorobenzene	132.2	1.57 (25°C)	
Alcohols, aldehydes, ketones			
Methanol	64.7	13.30 (21°C)	Architectural materials Industrial products such as treated wood resins, cosmetic, plastic adhesive, printing ink, cleaning agent Vehicle emission
Ethanol	78	7.32 (25°C)	
Isopropanol	82.5	5.33 (23.8°C)	
Formaldehyde	–19.5	1.33 (–88°C)	
Acetaldehyde	21.1	101.32	
Acetone	56.5	23.94 (20°C)	
Ethers, phenols, epoxy compounds phenol			
Phenol	181.9	0.03 (20°C)	Leakage from underground storage tank Watercrafts exhaust Coal chemical industry Oil refinery
Diethyl ether	34.6	58.79 (20°C)	
Ethylene oxide	10.8	145.64 (20°C)	
Esters, acid compounds			
Ethyl acetate	77.2	9.73 (20°C)	Industrial solvents (printing, pharmaceutical, petrochemical, etc) Coal chemical industrial
Butyl acetate	126.5	1.33 (20°C)	
Acetic acid	117.9	1.52 (20°C)	

indoor origin such as building materials, computer goods, furnishings, smoking, cooking, garages, indoor chemical reactions and outdoor VOCs. Usually, the pollution concentration from the indoor VOCs are present at low concentration. However, the accumulation of these chemicals in the indoor atmosphere for a long time could be hazardous to human health. VOCs are the major group of indoor air pollutants, which significantly impact indoor air quality (IAQ) and influence human health [130]. Poor air quality ventilation is an environmental problem and therefore, it is necessary to reduce the accumulation of VOCs in the buildings by specific air circulation or falter devices with special materials systems.

5.3.2. Outdoor VOCs

Outdoor volatile organic compounds evolve due to human activities, industries and transports that cause hydrocarbon emissions to the surrounding environment from many sources like solvents, vehicles and refineries [131]. Furthermore, outdoor air pollution has more influence on the globe. Many of these outdoor VOCs are considered as cosmogenic to the human and have contributed for environmental pollution problems such as global warming, ozone layer depletion and smog formation. As an example of two big industrial countries with a huge human population, a comparative study on the air quality in Japan and China to investigate the indoor and outdoor VOCs released in summer and winter during 2006 till 2007 [132] was undertaken. Fig. 9 shows the ratio of the concentration of indoor (living room) to outdoor for some VOCs (benzene, toluene and xylene) in the two countries. In the summer season, the concentration for the three types of VOCs varied and was often above 1.0 w whereas those in Japan were mostly 1.0 and the ratio in winter was like those in summer except xylenes. In China, xylene showed a large amount in summer than winter. The study is just an example of the reflection on the amount of VOCs in the air. Another example of outdoor VOC is methyl tert-butyl ether (MTBE). It is a famous gasoline additive that is mostly used to minimize the CO_2 released in vehicles. But, the leakage of the fuel containing MTBE to the groundwater could have harmful environmental influences since it is highly soluble in water (0.35–0.71 M) [133]. In 2015, another study reported that the pollution emissions in China approached 31.12 million tons in the year 2015 and the majority came from industrial bases such as pharmaceutical plants, wastewater treatment, petrochemical plants and miscellaneous tanks accounted for about 50% of the total emission in this country [124,134]. About 43% of the anthropogenic cause of VOCs comes from industrial processes, especially petrochemical and chemical processing. In addition, about 28% of the VOC emissions come from transportation which is accounted for by the huge population in China [135].

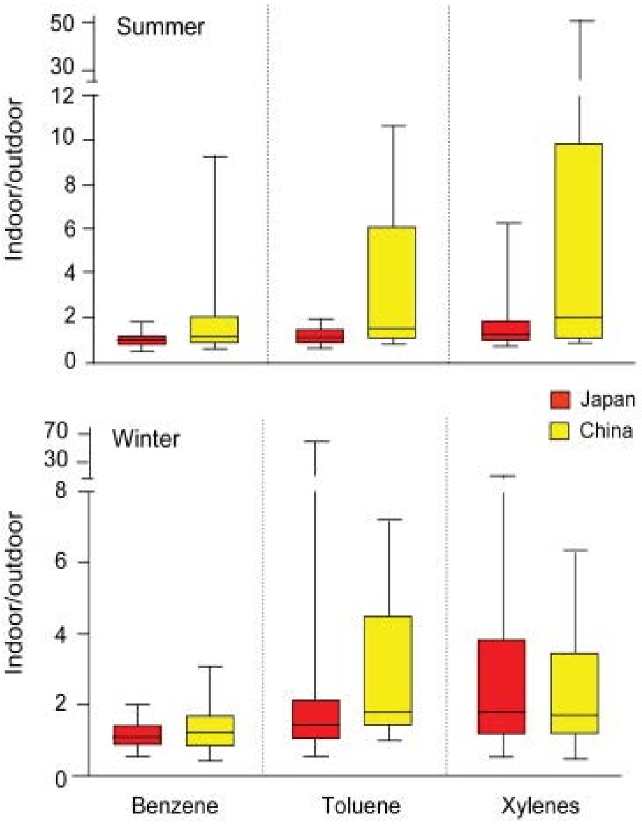

Fig. 9. Indoor to outdoor ratios of concentration for some VOCs in Japan and China for the year 2006 to 2007 [132].

5.4. PCO by heterogeneous photocatalytic oxidation of VOCs

Photocatalytic oxidation (PCO) is an interesting technique for VOCs removal and has the ability to degrade the VOCs even at low concentrations [136]. It is an attractive and promising technology for environmental remediation and air purification. It has the ability to oxidize the organic compounds to water, simple mineral acids and carbon dioxide at low temperatures [137]. This technique consisted of two important steps, first, the VOCs are transferred to the reaction surface, then decomposed by the photocatalyst. Consequently, the VOC mass transfer rate, the reaction surface area and the reaction rate are the crucial performance variables of the PCO reactors [138]. The photocatalyst reaction is initiated when the light hits the surface of the semiconductors to excite the electrons. The photoexcitation depends on the energy of the photon which must be greater or equal to the bandgap of the semiconductor [139]. During photoexcitation, the electrons are transferred from the lower energy valance band (VB) to the higher energy (e^-) conduction band (CB) to result in a hole (h^+) formation taking place in the (VB). Meanwhile, the recombination of electrons and holes (e^-/h^+) is a competitive process that could take place and terminate the photocatalytic reaction. The charge transfer rate is related to the interaction between the surface of the photocatalyst and the organic pollutant. However, modification of the photocatalysts can affect charge transfer and recombination in the photocatalysis process [140]. Trapping the excited electrons and holes will result in the formation of reactive species like hydroxide or superoxide radicals [141].

It is well known that the photocatalytic performance might be substantially affected by several variables, like specific surface area, porosity (pour structure and volume), crystal size and phase. In addition, the dimensionality related to the structure of the photocatalyst might impact its characteristics and functions, including photocatalytic activity, adsorption, reflectance and carrier transportation [142]. Besides, the photocatalytic oxidation process for the VOCs compounds has many operating parameters such as airflow rate, residence time, relative humidity, the type and the concentration of VOCs, light source and intensity that should be optimized [143].

5.5. Effects of operating variable on photocatalytic activity

5.5.1. Airflow and resident time

Transferring the pollutant mass from gas to the surface of photocatalyst involves different methods and is affected by airflow, the pollutant type and the natural properties of the photocatalyst. For example, in the case of the photocatalyst, the influence of the increasing flow rate could have two-sides: (i) the residence time of the reactant VOCs molecules inside the reactor decrease, which lead to lower the adsorption and conversion as well, (ii) the second argument is that there might be enhanced mass transfer between the air and photocatalyst surface to result in favorable PCO process rate [144]. Moreover, the airflow rate could impact the amount of by-products formation during PCO reactions. A report by Jeong et al. [145] used TiO_2 (P25) as a photocatalyst for the degradation of benzene and toluene. The performance showed that as the flow rate increased from 1.0 to 4.0 L min^{-1} in the absence of the photocatalyst, the conversion of 0.6 p.p.mv of the sample decreased gradually taking into account the decrease of the residence time from 33.0 to 8.3 s which minimized the contact time of the VOCs and hydroxyl free radicals. Nevertheless, in the presence of the photocatalyst TiO_2, the conversion of VOCs declined as the flow rate decreased from 1.0 to 3.0 L min^{-1}, then stabled even under a higher flow rate. Also, similar behavior was noticed in another sample with a concentration of 10 p.p.mv. Therefore, the photodegradation might be enhanced by increasing the contact time between the reactants and the photocatalyst.

5.5.2. Humidity

The relative humidity (RH) and percentage of toluene conversion in the presence and absence of TiO_2 under UV irradiation were reported. In both cases, the conversion of toluene improved with increasing relative humidity. Even so, at all the relative humidity levels, the toluene conversation process was higher in the presence of TiO_2. In another study on photodegradation of toluene by TiO_2 photocatalyst, it was noticeable that the behaviors of conversion and mineralization as a function of relative humidity (RH) were fundamentally different. At the lower range of 0%–20% of RH, the conversion appeared to be independent of humidity. However, higher water concentration is decreased from 95% to 85%, which is due to the competition of adsorption between water molecules and toluene [146].

5.5.3. Pollutant type and concentration

An increase in the concentration of the VOCs has a direct effect on the photocatalytic oxidation reaction due to several related facts. First, the number of the VOC molecules adsorbed on the surface of the photocatalyst increases the reaction kinetics. Secondly, a decrease in the reaction between the reactive species of the pollutant molecules results in lower VOCs molecules from the degradation process [147]. Thirdly, a growing number of by-products or intermediates while during the photoreaction can minimize the active sites thus hindering the oxidation process. Boulamanti et al. [148] studied the effect of VOCs concentration on the oxidation rates on C_5-C_7 alkanes in the gas phase and the reaction increased, in the following order: pentane, iso-pentane, hexane, iso-hexane and heptane. It is clear that the iso-isomers oxidized faster than the linear forms of the same compounds and the presence of tertiary carbon atoms enhanced the reaction. Heptane had the highest oxidation rate which indicated that a large molecular chain results in a favorable oxidation rate.

5.5.4. VOCs properties

The effects of concentration of the VOCs contaminants differ due to the different properties such as boiling point, vapor pressure and molecular size, which could have an impact on the degradation performance [149]. The higher the concentration of VOCs, the higher the adsorption rate, which increases the reaction kinetics and reduces the pollutant conversion to CO_2 in the photocatalytic process. According to the research by Li et al. [150], photocatalytic efficiencies decrease gradually with increasing toluene initial concentration under the same reaction time, although the formation rates of H_2O and CO_2 increased. Another study showed that the photocatalytic efficiency of graphene oxides (GO) coupled with TiO_2 to form GO-TiO_2-400 for the degradation of 2-ethyl-1-hexanol (2E1H) as an example of VOC, decreased gradually from 83% to 61% as the initial concentration was increased from 0.1 to 1.5 ppm [151]. It might be suggested that decreasing the initial concentration may affect the adsorption during the VOC photodegradation process. The VOCs with higher molecular weight will be difficult to degrade since many oxygen atoms are needed for total oxidation. Moreover, the oxidation rates of three VOCs like m-xylenes, o-and p-xylene were different showing that stability has an effect [152]. Generally, the VOC properties such as molecular weight, stereochemical structure, polarity and kinetics should be studied during the adsorption process [2].

5.5.5. Intermediate

Normally, the degradation process of the VOCs by photocatalytic oxidation would form CO_2 and H_2O. However, during the reaction process occasionally, some intermediate products could be formed. These intermediates compounds can be harmful and extent their effect on humans and the environment. In addition, they can deactivate the catalyst through saturation and poison the catalyst surface. Consequently, it is important to study the intermediates or by-products formation during the photocatalytic process [153–155]. Table 4 provides a summary of some intermediates that are formed from the VOCs photodegradation.

5.5.6. Light intensity

It is well known that light intensity is a crucial factor in influencing the process of the reaction rate of VOCs [159]. In general, increasing the intensity of light would increase the photocatalytic oxidation and decomposition rate [160]. El-Roz et al. [161] used TiO_2 nanotube (TNT) to investigate photooxidation of methanol, n-hexane and carbon monoxide. It was found that methanol conversion was completed before the others, which indicated that the selectivity was affected by light intensity. Moreover, when intensity has increased the production of oxidant species was also enhanced which was shown by the high amount of carbonyl species at the beginning of the irradiation. Consequently, an increase in the UV-irradiation intensity caused an increase in the activity and selectivity of the photocatalyst materials. There is, therefore, a need for the selection of appropriate light sources to conduct total mineralization of VOCs pollutants into other environmental species like water, CO_2 and mineral acids [162].

5.5.7. Coupling material effect

Changing the structure of materials such as TiO_2 by modifying with other materials to improve the structural and textural properties especially for environmental applications is a promising idea. That includes doping TiO_2 by metal or nonmetal, co-doping with varieties of elements and coupling with semiconductors like g-C_3N_4 and Fe_2O_3. Broadly, this improves the photoexcited charge separation and modifies the absorption light towards the visible light region.

Development of photocatalysts that efficiently utilize the visible portion of the light is essentially recommended since ROS ($^{\bullet}$OH, O_2^{-}, $^1O_2$, etc.) are produced through absorption of ubiquitous ambient visible light. Various methods have been employed to improve the visible light absorption of TiO_2, such as metal modification (doping and nanoparticle loading), non-metal doping, formation of heterojunction with other semiconductors, sensitization and introduction of defect sites [163]. Among these methods, the coupling of TiO_2 with smaller bandgap semiconductors to form heterojunction nanocomposites that can absorb visible light allows the visible light-excited electrons (or holes) to be transferred to TiO_2 when the semiconductor CB (or VB) is located at a more negative (or positive) potential than that of TiO_2. Such modification techniques have solidified TiO_2 as the most popular and successful base material for visible light photocatalysis. g-C_3N_4, with a bandgap between 2.6 eV and 2.8 eV shows relatively low activity for degrading pollutants because its low VB potential (1.4 eV vs. NHE) is not enough for generating hydroxyl radicals [164]. To overcome this, various heterojunction structures based on g-C_3N_4 have been developed. Besides tuning the photocatalysts to harvest visible light, morphology control is another factor that needs careful consideration in the design of photocatalysts for VOCs degradation. TiO_2 with various morphologies such as dispersed powder, thin-film, pellets and honeycomb shape was synthesized and evaluated for the degradation of various VOCs (ethylene, propylene, and toluene). The dispersed powder and thin film TiO_2 showed higher VOC degradation activity because more TiO_2 surface was exposed to VOCs, O_2 molecules and light irradiation compared to pellets and honeycomb structures [165].

In addition, porous structures are desirable as higher photocatalytic activity and durability for VOC degradation have been reported [166]. The best design for photocatalytic systems for VOCs degradation is the immobilized thin film form on a substrate. The densely packed immobilized photocatalyst nanoparticles in the film, allow O_2 and VOC molecules to diffuse slowly to the active sites of the photocatalyst through interstitial space in an immobilized film. However, the densely packed photocatalyst film limits the supply of O_2 hence *in-situ* generated recalcitrant intermediates of VOC degradation, which are the main cause for photocatalyst deactivation, may not be easily removed [167]. The subsequent section provides details on the various g-C_3N_4 based nanocomposite photocatalysts for VOCs degradation.

6. Graphitic carbon nitride g-C3N4 composite photocatalyst for VOCs degradation

Semiconductors such as titanium dioxide TiO_2, zinc oxide (ZnO), zinc sulfide (ZnS) and cadmium sulfide (CdS) are very commonly used as photocatalysts for VOCs degradation [168]. Among them, TiO_2 is wildly studied due to its availability, costly-effective and chemical stability. In addition, it has a powerful ability to mineralize the organic

Table 4
Summary for some intermediate and active species from VOCs photodegradation

VOCs	Intermediates	Detection instruments	Ref.
Toluene	Formic acid, benzaldehyde, benzyl alcohol, $O_2^{-\bullet}$ and $^{\bullet}$OH	GC-MS, ESR	[156]
Toluene	Formaldehyde, acetaldehyde, acetone, 2-butanone, o-cresol and benzaldehyde	FT-IR, GC-MS	[157]
Toluene	Hydrocarbons	FT-IR	[158]
Benzene	Phenol, malonic acid and benzenediol	FT-IR	[159]
Acetylene	Carboxylic acids, CO	GC and HPLC	[160]
Limonene	Acetaldehyde, methacrolein, 2,3-dihydrofuran, formaldehyde, acetone, 2-pentanone, acetic, 1-butanol, ethanol and CO	GC, HPLC and FT-IR	[161]

pollutant by generating active species such as $OH^{\bullet}$ and $O_2^{\bullet-}$ under light illumination [169]. Anatase TiO_2 exhibits higher photoactivity than the others due to the structural arrangement and the abandoned formation of the Ti-O-Ti bond at the surface [170]. However, TiO_2 has a large bandgap of 3.2 eV, which can minimize the response to visible light.

Several studies have reported the application of TiO_2 as a photocatalyst for the degradation of various VOCs. Assadi et al. [171] reported the elimination of isovaleraldehyde by UV/TiO_2 photocatalysis where different reactors configurations and scales (photocatalytic cylindrical reactor, planar reactor, and pilot unit) were evaluated for their effectiveness. Increasing the flow rate and the UV intensity was reported to result in increased removal capacity in the pilot unit. Degradation by-products were identified as propionic acid, acetone, and acetic acid. In another study, the effect of different operating parameters on a continuous photocatalytic reactor for isovaleraldehyde oxidation was evaluated and a chemical degradation pathway was proposed [172]. A cylinder and flat-plate photoreactor at different air gaps (20–60 mm) and gas residence times (0.67–5.0 s) and a plug flow reactor system was developed to perform kinetic studies of (i) isovaleraldehyde removal, (ii) selectivity of CO_2 and (iii) by-products formation and removal. The planar reactor was equipped with eight UV lamps and coated TiO_2 nanoparticles. An increase in relative humidity led to more photodegradation of the pollutants and the presence of water vapor was beneficial at low concentrations due to the formation of OH radicals that contributed to the increased photodegradation. In yet another study, the synergetic effect of dielectric barrier discharge (DBD) plasma and immobilized TiO_2 was reported for indoor treatment of butyraldehyde at pilot scale under UV irradiation [173]. The combination of these two technologies led to an enhancement of butyraldehyde abatement compared to the separate systems at pilot scale and CO_2 selectivity was significantly improved when compared to the DBD plasma alone. Coupling of plasma and photocatalyst process was reported to improve VOC decomposition, by-products formation and energy yield. The same group also reported on the pilot to industrial-scale pollution removal in exhaust gases from animal quartering centers by combining photocatalysis with surface discharge plasma [174]. Results showed that process combination leads to an enhancement isovaleraldehyde removal compared to the separate systems even at a high flow rate of 250 $m^3\,h^{-1}$. The synergistic combination of TiO_2 photocatalysis with plasma technology is a promising method for removing air pollutants. In an effort to evaluate the feasibility of VOC's removal at a large scale, a comparative study between laboratory and large pilot scales for VOC's (isovaleraldehyde) removal from gas streams in continuous flow surface discharge plasma was reported [175]. Increasing both the flow rate and specific energy leads to improved removal capacity. It was concluded that plasma reactor scale-up for pollutant removal is feasible. Zou et al. [176] reported TiO_2–SiO_2 based pellet photocatalysts with high surface areas of 274.1–421.1 $m^2\,g^{-1}$ in a fixed-bed reactor installed with a UV blacklight lamp for the degradation of toluene. The catalyst pellets with a higher surface area (421 $m^2\,g^{-1}$) achieved higher conversion efficiency (100%) for a longer period and only CO_2 and water were the final products. Yang et al. [177] VOC reported the removal of manure gaseous emissions with UV Photolysis and UV-TiO_2 photocatalysis. The effects of the UV dose, wavelength, TiO_2 catalyst, air temperature and relative humidity were tested at lab scale on a synthetic mixture of nine odorous VOCs and real poultry manure off-gas. The treatment effectiveness or % conversion was proportional to the light intensity for synthetic VOCs mixtures and followed an order of $UV_{185+254}$ + TiO_2 > UV_{254} + TiO_2 > $UV_{185+254}$; no catalyst > UV_{254}; no catalyst.

Despite these tremendous advancements in the removal of VOCs using TiO_2 and UV radiation, the use of UV lamps is still considered a challenge from a cost point of view. Also, the excited charge carriers in the TiO_2 have a high recombination rate which also inhibits the photocatalytic performance. Therefore, coupling the TiO_2 with other semiconductors such as g-C_3N_4 can improve the structure and photochemical properties [178].

Xiao et al. [179] prepared nanostructured photocatalytic materials from graphitic carbon nitride and TiO_2 to form TiO_2@g-C_3N_4 composite by one-step calcination route. The XRD patterns of the pure TiO_2, g-C_3N_4 and TiO_2@g-C_3N_4 composites are shown in Fig. 10. A sharp peak around 27.4° was attributed to the interplanar stacking of graphite aromatic rings and the peak at 13.1° from the in-plane structure of repeating patterns. In addition, a dominant anatase phase and a few rutile phase peaks are observed, which indicates the characteristics diffraction patterns of TiO_2 (P25). Moreover, the XRD pattern displayed both diffraction peaks of P25 and g-C_3N_4 in all the samples of TiO_2@g-C_3N_4 composites, which indicates the formation of the heterostructure composite.

The photocatalytic degradation of phenol by TiO_2@g-C_3N_4 composite materials under various light sources were examined. The photocatalytic performance for phenolic degradation showed a reliable degradation with various light intensities and a higher photocatalytic activity was observed at higher light intensity. Furthermore, results illustrated that the photogenerated holes (h^+) and superoxide radical anions ($^{\bullet}O^{2-}$) were the responsible active species for the photocatalytic degradation process. Additionally, the synergistic mechanism was proposed based on the bandgap energy value of the photocatalyst material.

Zhang et al. developed a decorated spinel $ZnFe_2O_3$ nanoparticles on g-C_3N_4 sheets to form (CN-ZnFe) composites by one-step solvothermal method [180]. The material exhibited a magnetic property and showed interesting photocatalytic activity due to the loading of $ZnFe_2O_4$ nanoparticles. In addition, the measured BET surface area was about 48.8 $m^2\,g^{-1}$ for $ZnFe_2O_4$ photocatalyst which was greater than that of CN (25.6 $m^2\,g^{-1}$). Different mass ratios of g-C_3N_4 (CN) were used to prepare the composites of x-CN-ZnFe such as 80 CN-ZnFe, 160 CN-Fe and 320 CN-Fe, where x was the mass of the CN used. The photocatalyst 160 CN-ZnFe displayed the optimum activity and unique properties, which were ascribed to the synergistic effect of the two components, particle size and charge carries separation. Moreover, more than 33% degradation of phenol was observed by 160 CN-ZnFe photocatalysts under visible light illumination when compared to 10% degradation by pristine g-C_3N_4 and there was no observed degradation by

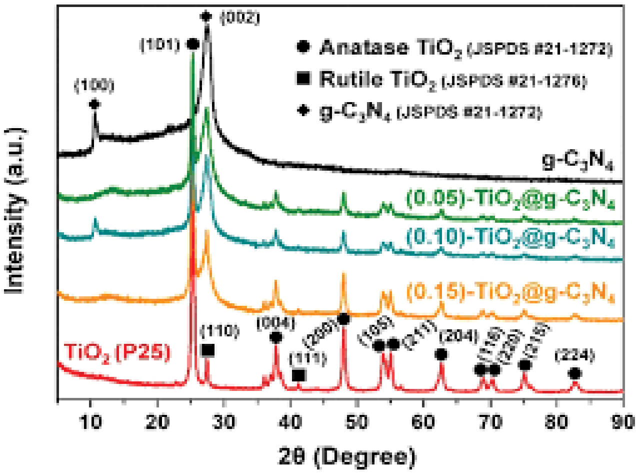

Fig. 10. XRD patterns of TiO_2 (P25), g-C_3N_4 and TiO_2@g-C_3N_4 heterostructure composites [179].

visible light photolysis. This was due to the doping effect of CN-ZnFe nanoparticles on the enhancement of photocatalytic activity under visible light irradiation. Jo et al. [108] reported a nanocomposite prepared by facile co-precipitation method, which contained ZnO, g-C_3N_4 and graphene oxide (GO) to form ZnO-g-C_3N_4/GO ternary photocatalyst. Pristine g-C_3N_4 appeared as a thin and porous structure and the ZnO nanospheres on the ZnO-g-C_3N_4 composite were well dispersed over the composite. The surface morphology of the ternary ZnO-g-C_3N_4/GO composite showed clear dispersed ZnO nanospheres on the GO surface which makes a layer attached to the g-C_3N_4.

Pure ZnO has absorption edge at 396 nm which is equal to 3.13 eV bandgap energy value, whereas pure g-C_3N_4 shows the absorption edge at a wavelength of 470 nm (2.63 eV). Meanwhile, a significant redshift was noted for the ZnO-g-C_3N_4 composites and exhibited a maximum absorption at 468 nm (2.67 eV) with g-C_3N_4 loading up to 50%. However, loading of the additional amount up to 70% of g-C_3N_4 in the composite materials altered the absorption edges leading to a shift towards a lower wavelength region of around 462 nm (2.68 eV). There was an increase in the absorption of visible light at 517 nm (2.39 eV) by ternary composites of ZnO-g-C_3N_4/GO compared to other samples, which indicated an enhanced redshift by 10% GO content. This was due to the effect of graphene oxide delocalization.

It is very essential to form a composite photocatalyst using two different types of semiconductors. Efficient heterojunction photocatalysts and suitable coupling of the band energy level of the conduction and valance bands in the semiconductors enhance charge separation and transfer of charge carrier electron-hole pairs [181]. Katsumata in his research was prepared g-C_3N_4/WO_3 composite by physical mixing method to evaluate the catalytic photodegradation of acetaldehyde gas [182].

The composite exhibited the high activity for photodecomposition of acetaldehyde gas under visible light irradiation into CO_2 molecule within 24 h. The degradation mechanism of the g-C_3N_4/WO_3 photocatalyst for the degradation of CH_3CHO gas is shown in Fig. 11 where

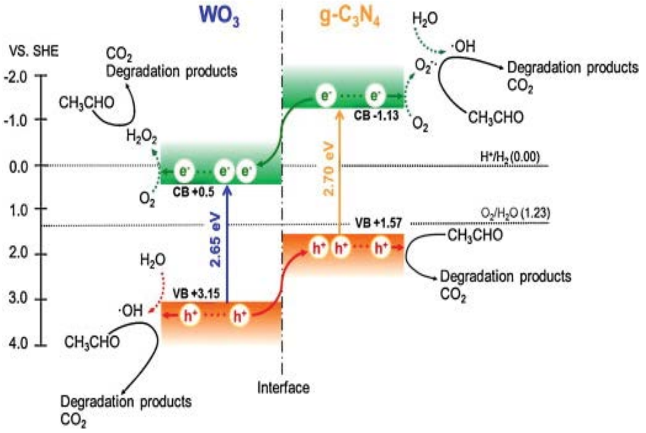

Fig. 11. Proposed mechanism for the degradation of CH_3CHO by g-C_3N_4/WO_3 photocomposition under visible light illumination [182].

some of the photogenerated holes on the surfaces of WO_3 which has oxidation potential (+3.15 V vs. SHE) directly reacted with CH_3CHO molecules that were adsorbed on the surfaces of WO_3 particles or may have reacted with a surface-bound water molecule to form •OH radical species. The other photogenerated holes (h^+) were transferred to the g-C_3N_4 surface and directly degraded the CH_3CHO molecules adsorbed on the g-C_3N_4 surface. Meanwhile, the photogenerated electrons in the g-C_3N_4 surface reacted with oxygen to form $O_2^{\bullet-}$. The formed superoxide anion reacted with the water molecules to form hydroxyl radicals (•OH). Some of the electrons transferred to the WO_3 surface and reacted with O_2 to form H_2O_2. The oxygen active species like •OH, $O_2^{\bullet-}$ and H_2O_2 that were generated on the surfaces of the g-C_3N_4/WO_3 composite were distributed and spread by the gas phase and degraded the CH_3CHO molecules.

Research can able to incorporate the V_2O_5 into the organic semiconductor g-C_3N_4 to obtain a heterostructure V_2O_5/g-C_3N_4 (VOCN) photocatalyst by solvothermal method followed by thermal treatment [183]. The composite demonstrates a strong absorption in the visible region, high specific surface area and enhanced the separation of photo-induced charge carriers (e^-/h^+), which supported the improvement in photodegradation of ortho-dichlorobenzene (o-DCB).

Fourier-transform infrared (FT-IR) spectra of the VOCN composite reveal both feature peaks of g-C_3N_4 and the V_2O_5, with the enhancement in the peak intensity as the amount of V_2O_5 particles increased in the VOCN composites.

Photoluminescence (PL) spectra of undoped V_2O_5, pure g-C_3N_4 and VOCN composites at an exciting wavelength of 380 nm showed that the VOCN composites had an extremely low emission intensity, which indicated the decrease in the irradiative recombination of the charge, carries in the VOCN. This improved the separation of photo-induced electron-hole pairs allowed them to participate in the surface of VOCN catalyst for effective photocatalysis as shown in Fig. 12. The 2% VOCN illustrates the highest photocatalytic degradation (62.4%) compared

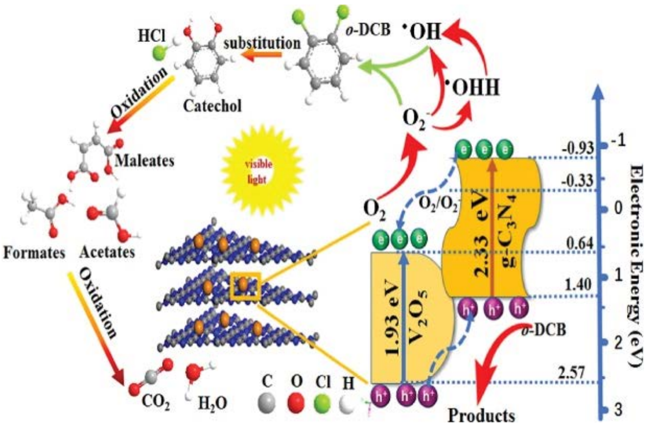

Fig. 12. Schematic bandgap match and (e^-/h^+) separation of 2% VOCN [183].

to pristine g-C_3N_4 and V_2O_5. All the reactions followed the 1st order kinetic reaction curve with a rate constant of 2.8 times higher over 2% VOCN than pure g-C_3N_4 and that indicates the effect of coupling with the V_2O_5 on the photocatalytic degradation.

Improving the photoconversion efficiency in the g-C_3N_4 by coupling with suitable semiconductors to synthesize a heterojunction is an effective strategy. The formation of heterojunction would result in efficient charger transfer through the heterointerface, leading to locative separation of charge carriers and enhance the overall photocatalytic process. The g-C_3N_4 nanosheet provides favorable platform for supporting doped materials on the surface. Li et al. [184] used solvothermal techniques to prepare different TiO_2 nanostructures on the surface of graphitic carbon nitrides like 0-dimensional nanoparticles, 1D nanowires, 2D nanosheets and 3D mesoporous crystals. Among all the nanostructures, seed-grown Meso-TiO_2/g-C_3N_4 showed a high photocatalytic activity under visible light irradiation for the degradation of organic pollutants such as methyl orange and phenol. The pores arising from gaps between Meso-TiO_2 microspheres that are sandwiched and surrounded by g-C_3N_4 nanosheets, resulted in enhanced charge transfer across the composite.

A coral-like structure of $BiVO_4$/g-C_3N_4 photocatalyst prepared by a calcination technique for photocatalytic degradation of toluene was reported [185]. Fig. 13a shows the FT-IR spectra of pure g-C_3N_4 (CN), pure $BiVO_4$ (BVO) and $BiVO_4$/g-C_3N_4 (BVC) composite. The BVC samples spectra represent both characteristic peaks of pure CN and BVO, also it is noticeable that the intensity of VO_4^{3-} peak at 744 cm^{-1} increased as the BVO mass ratio (0.5%, 1%, 3%, 5%, 10%) content become greater in the BVC samples.

Additionally, the phase structure and morphology of the samples are shown by SEM images in Fig. 13Ba–d. The BVO composite revealed regular polyhedral structures due to a dispersive mechanism of sodium dodecyl sulfate (SDS). The CN sample has different nanosized crystals of stacked layers. After adding 3% BVO to form the BVC-3 composite, a coral-like structure with about 80 nm in diameter was obtained as in Fig. 13Bc. Furthermore, when the content amount of $BiVO_4$ increased to 3% in the composite of BVC-3, the highest specific surface area up to 33.9 $m^2\,g^{-1}$ and pour volume of 0.291 $cm^3\,g^{-1}$ were observed.

Fig. 14a shows the degradation of toluene over different photocatalysts and the results indicate that the BVC-3 sample presented the best photodegradation of toluene between the samples. After 8 h of the degradation reaction under visible light irradiation, the BVC-3 composites reached the mineralization rate of about 68.2% and had the highest CO_2 production as shown in Fig. 14b. In addition, the proposed Z-scheme for the photocatalytic activity by BVC composite is shown in Fig. 14c. The superoxide ($O_2^{\bullet-}$) and hydroxyl radical ($^\bullet$OH) active species were produced with electrons (e^-) in the CB of the g-C_3N_4 surface.

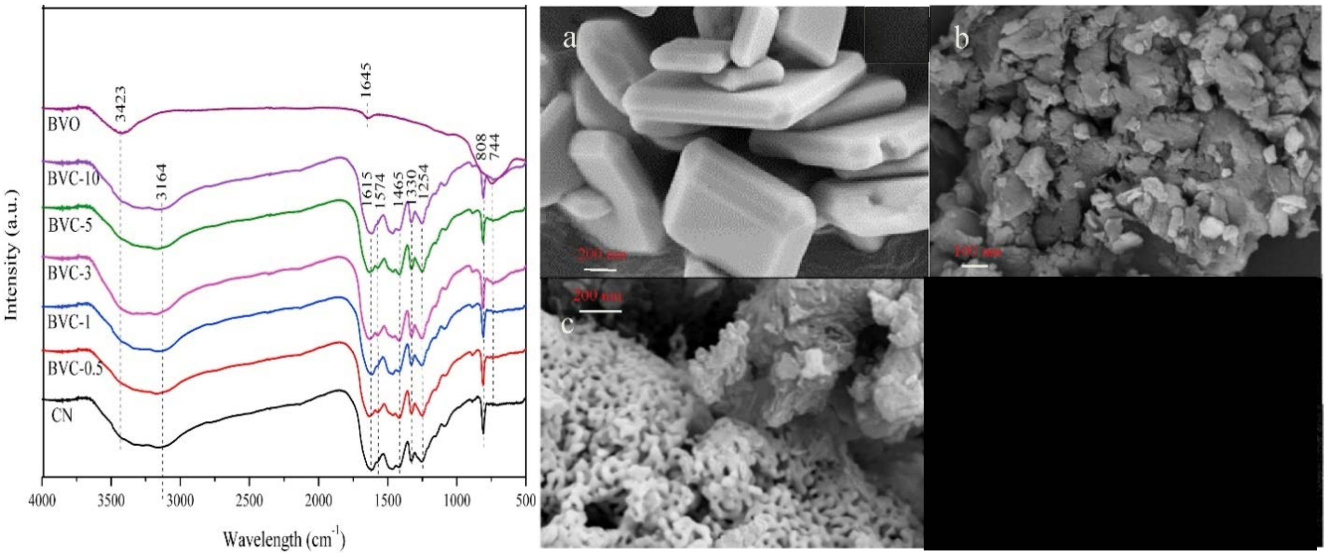

Fig. 13. (A) FT-IR spectra of the CN, BVO and BVC samples and (B) SEM images of (a) CN, (b) BVO, and (c) BVC-3 composite and [185].

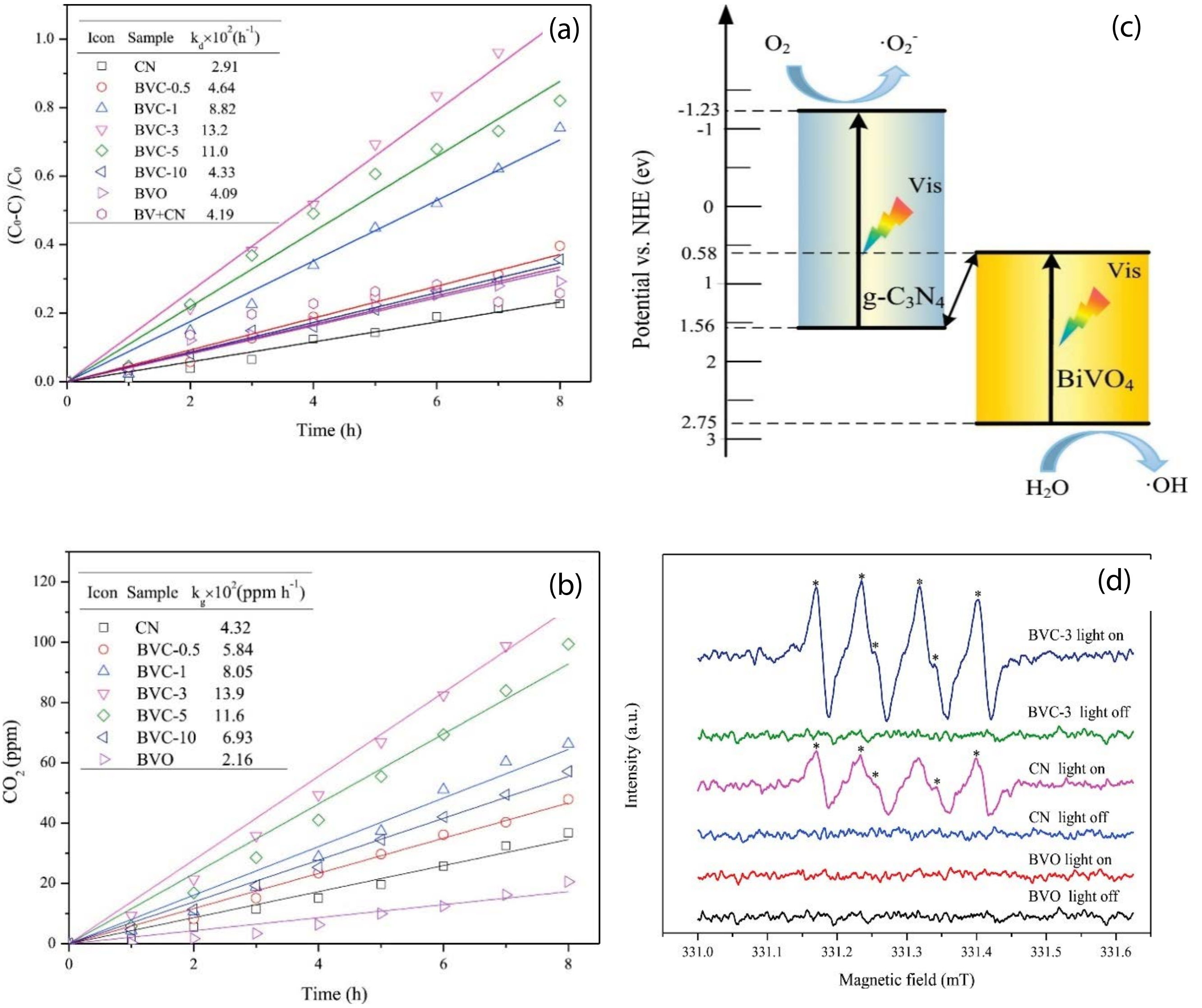

Fig. 14. (a) Toluene degradation over prepared photocatalysts under visible light, (b) CO_2 generation, (c) schematic proposed mechanism over BVC composite and (d) ESR spectra of prepared samples with DMPO-CH_3OH under $\lambda > 400$ nm irradiation [186].

Meanwhile, the holes (h^+) were generated in the VB of $BiVO_4$. Therefore, the holes, $^{\bullet}OH$ and $^{\bullet}O_2^-$ generated at the photocatalyst surface were the main active species for the degradation of toluene. To investigate the presence of superoxide and hydroxyl radicals in the mechanism and the possible Z-scheme by the presence of superoxide and hydroxide radicals [186], the electron spin resonance spectroscopy (ESR) analysis for CN, BVO and BVC-3 with DMPO-CH3OH as a trapping candidate were examined in Fig. 14d. The peak intensity of $^{\bullet}O_2^-$ for BVC-3 samples was higher than CN, which could be ascribed to extra generation of superoxide radicals on the surface of BVC-3 than CN. Likewise, the charge carriers which represents the electrons in the CB of CN and the holes in VB of $BiVO_4$ were competently separated and more electrons generated in CB at CN surface converting O_2 to $^{\bullet}O_2^-$. The TA-PL experiment of the BVC-3 photocatalyst and ESR analysis showed that the $^{\bullet}OH$, $^{\bullet}O_2^-$ and holes (h^+) were the main reactive species for toluene degradation.

In another study, Cu-$NiWO_4$ was hybridized with graphitic carbon nitride to produce a Cu-$NiWO_4$/g-C_3N_4 composite. As shown in Fig. 15a, the incorporation of Cu^{2+} into the $NiWO_4$ crystal led to the replacement of Ni element and disorder in the $NiWO_4$, which caused broadening and left shifting of the peak in the XRD pattern. Further, the addition of g-C_3N_4 into the $NiWO_4$ or Cu-$NiWO_4$ had no effect on the crystallinity and the XRD analysis displayed the formation of Cu-$NiWO_4$/g-C_3N_4 hetero-composite. Moreover, the PL peak intensities related to the lifetime of electron photo-induced formation on the prepared materials is shown in Fig. 15b. The Cu-$NiWO_4$/g-C_3N_4 material reveals the lowest PL result which indicated the enhanced separation of charge carriers and minimum e^-/h^+ recombination among the prepared photocatalysts.

The single components and the possible Z-scheme material (Cu-$NiWO_4$/g-C_3N_4) for the photocatalyst were evaluated for the degradation of n-hexane as shown in Fig. 16a. The optical properties were enhanced in the Z-scheme due

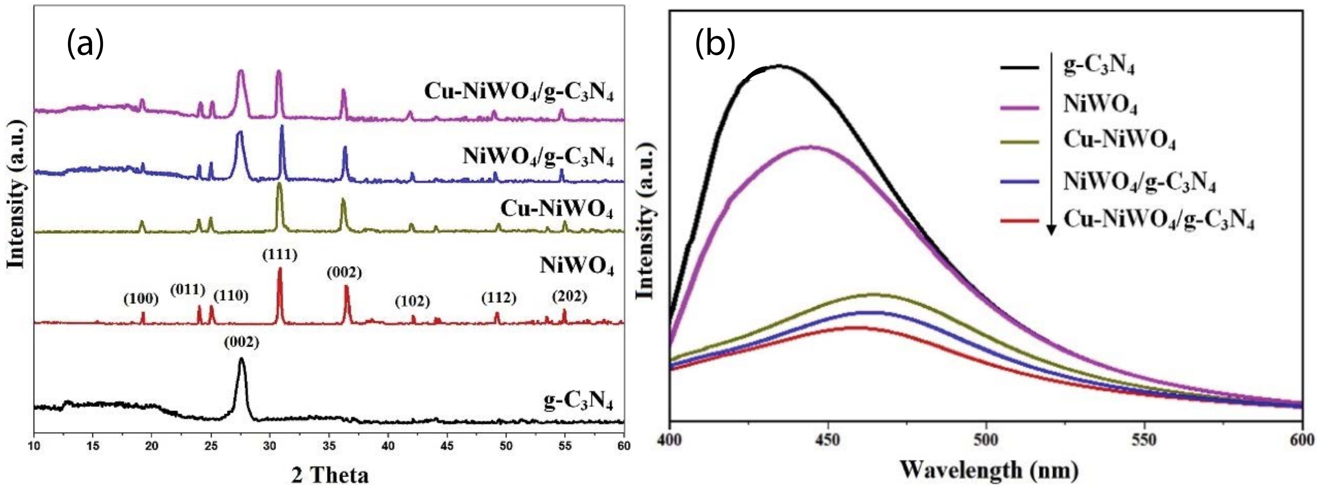

Fig. 15. (a) XRD pattern and (b) PL spectra of the prepared g-C_3N_4, $NiWO_4$, Cu-$NiWO_4$, $NiWO_4$/g-C_3N_4 and Cu-$NiWO_4$/g-C_3N_4 photocatalysts [16].

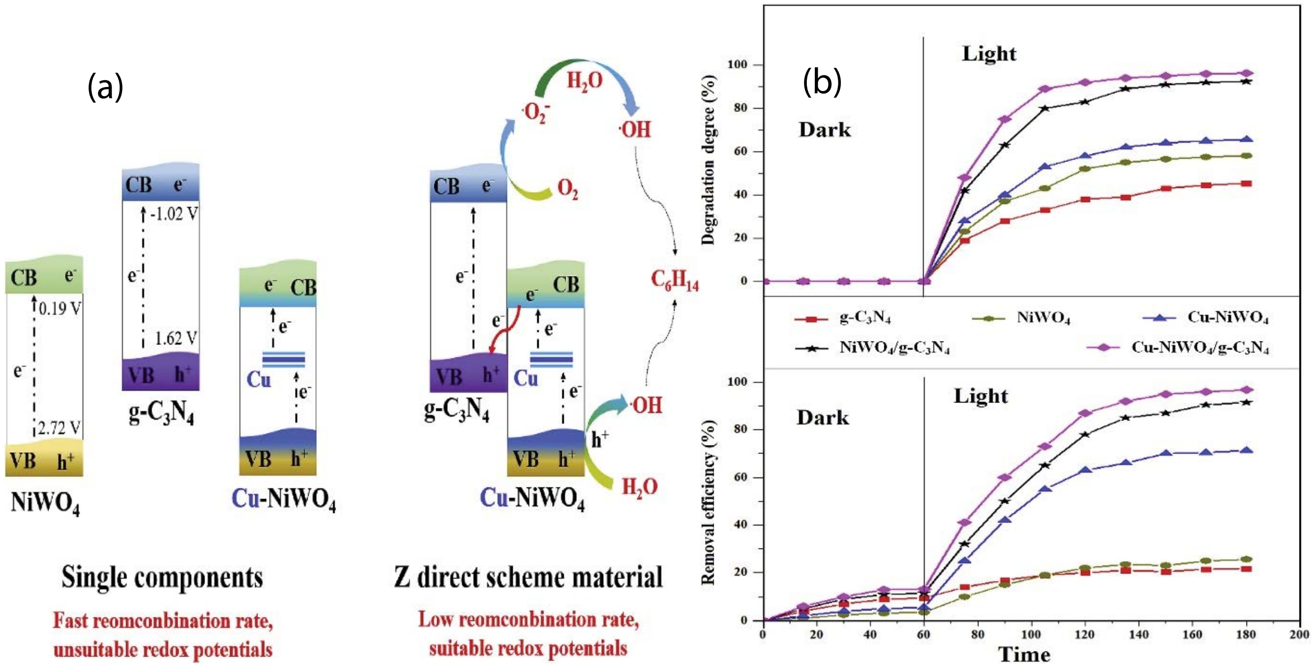

Fig. 16. (a) Proposed Z-scheme of prepared Cu-$NiWO_4$/g-C_3N_4 and (b) removal and degradation efficiency of n-hexane by prepared photocatalysts [16].

to the reduction in recombination rate for photo-induced electrons–holes compared to single materials. Furthermore, the Cu dopant in the Cu-$NiWO_4$ might have narrowed the energy bandgap and improve the absorption of visible light. Therefore, the addition of graphitic carbon nitride to the Cu-$NiWO_4$ could lower the energy level of the bandgap and enhance the absorption ability of the visible light for better photocatalytic activity in the Cu-$NiWO_4$/g-C_3N_4 composite. Likewise, the removal performance and degradation of the n-hexane (VOC) over the prepared photocatalyst which was conducted in the dark condition for 60 min and 2 h under visible light irradiation are shown in Fig. 16b. The Cu-$NiWO_4$/g-C_3N_4 photocatalyst showed the highest removal (96.8%) and degradation (96.3%) performances with enhanced stability during the removal reaction process.

Ag_3PO_4 is a high oxidative semiconductor material that has a photocatalytic activity under visible light irradiation less than 530 nm with a superior crystal structure of rhombic dodecahedrons and higher activity than other structures like cubes or spheres [187]. Shen et al. [188] used Ag_3PO_4 particles to couple with g-C_3N_4 sheets by deposition precipitation method at normal temperature to prepare g-C_3N_4/Ag/Ag_3PO_4 composite for phenol degradation. Fig. 17a and b illustrate the SEM images of the smooth surface sheets of g-C_3N_4 and the regular rhombic dodecahedral structure morphology of Ag_3PO_4 particles. Besides, the Ag_3PO_4 particles were anchored onto the surface of g-C_3N_4 sheets while forming the g-C_3N_4/Ag/Ag_3PO_4 composite (AC 1.0) as shown in Fig. 17c and d.

Fig. 18a shows the kinetic constant (*k*) calculated values for all the prepared samples. The $AC_{1.0}$ composite presents optimum photocatalytic activity with the highest degradation rate of 1.13 min^{-1}. Furthermore, within 4 min of the reaction process, the $AC_{1.0}$ photocatalyst demonstrates a significant photo-decompose of phenol with 100% degradation compared to pure g-C_3N_4 (9%) and Ag/Ag_3PO_4 (83%) as shown in Fig. 18b. Moreover, the $AC_{1.0}$ composite exhibited the highest stability and photocatalytic activity as shown in Fig. 18c, where after 5 cycles, about 75% of phenol was degraded within 5 min.

Semiconductor photocatalysts could be extended for smart uses in many future applications. Li et al. [189] reported the preparation of g-C_3N_4@Cs_xWO_3 nanocomposites series by ultrasonic-assisted method, which had the ability to isolate the UV-light and penetrate visible light and near-infrared. These features can be applied in smart window coating for green indoor condition applications.

Fig. 19a shows the XRD analysis of the crystallographic structure of different synthesized samples by varying the amount of g-C_3N_4 to be 10, 40, 70, 100 and 140 mg and incorporated with a fixed amount of Cs_xWO_3 to formed xCNCWO, where x is the mass of g-C_3N_4 added. The 40CNCWO nanocomposites showed similar XRD patterns with the pure Cs_xWO_3 materials. In addition, a diffraction peak of g-C_3N_4 overlaid with the peak structure of Cs_xWO_3, but less amount of g-C_3N_4 did not have a substantial effect on the phase and crystal in the CNCWO composite. Furthermore, investigation of the photocatalytic activity by the radical species trapping during the degradation of formaldehyde (HCHO) in presence of 40CNCWO photocatalyst is shown in Fig. 19b. A potassium dichromate, para-quinone (BQ), salicylic acid and sodium oxalate were used for the trapping of e^-, $^{\bullet}O_2^-$, $^{\bullet}OH$ and h^+, respectively. Obviously, that BQ reacts with $^{\bullet}O_2^-$ and produces more CO_2 than other scavengers. Therefore, $O_2^{\bullet-}$ was the main reactive species during the photocatalytic process. The detail for the process of photocatalytic oxidation (PCO) over CNCWO photocatalyst is provided in Fig. 19c, where the irradiation with UV-light generated holes in the VB of the g-C_3N_4. Meanwhile, electrons photogenerated in the CB of Cs_xWO_3, and the Z-scheme heterostructure in the CNCWO nanocomposite prevented the electron–hole recombination, which led to enhanced photocatalytic decomposition of the VOCs.

Heterostructure of g-C_3N_4/Ag/TiO_2 microspheres was prepared through doping Ag to form Ag/TiO_2 microspheres by photo-deposition method followed by encapsulating g-C_3N_4 into Ag/TiO_2, and the Ag nanoparticles acted as interlayer mediator between the g-C_3N_4 and TiO_2 surface [190]. In this ternary composite, the components were bridging with each other as shown by TEM images in Fig. 20. The broken microsphere cross-section shows the three layers with an outer g-C_3N_4 layer for about 80 nm, and also TiO_2 and Ag as interlayers with about 5 nm nanoparticles size for the Ag nanoparticles as shown in Fig. 20a–d.

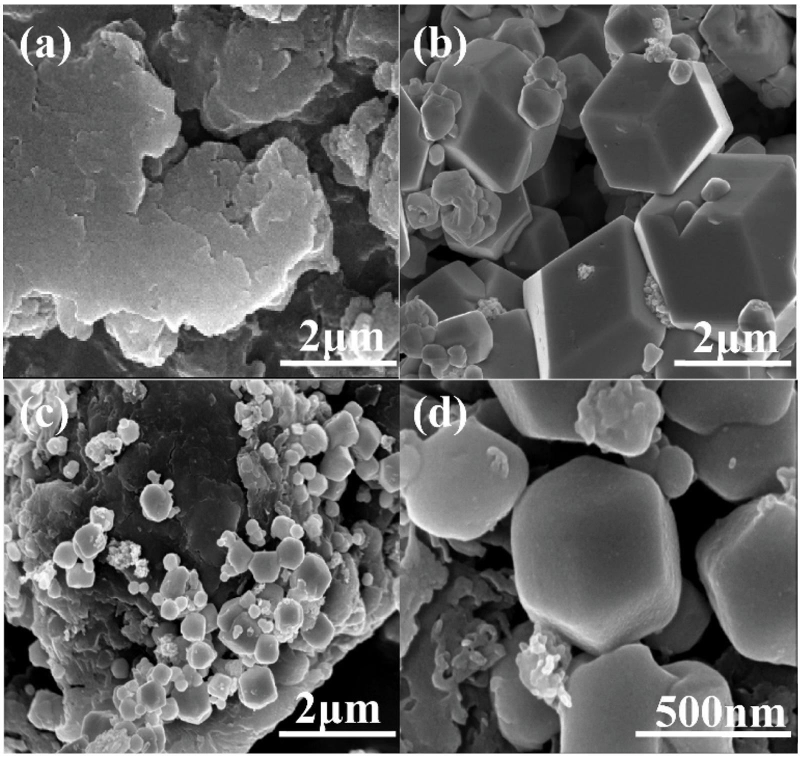

Fig. 17. SEM images of (a) pure g-C_3N_4, (b) Ag_3PO_3 particles, and (c & d) $AC_{1.0}$ composite [188].

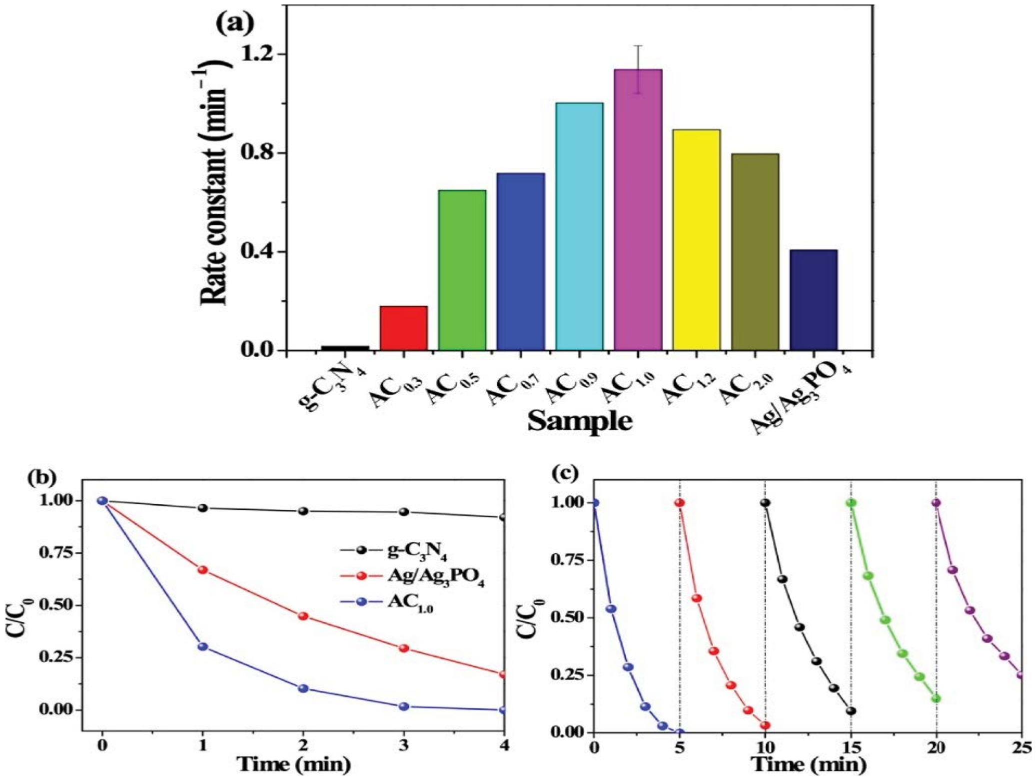

Fig. 18. (a) The kinetic constant of all samples, (b) phenol degradation over g-C_3N_4, Ag/Ag_3PO_4 and $AC_{1.0}$ samples and (c) cyclic stability of $AC_{1.0}$ [188].

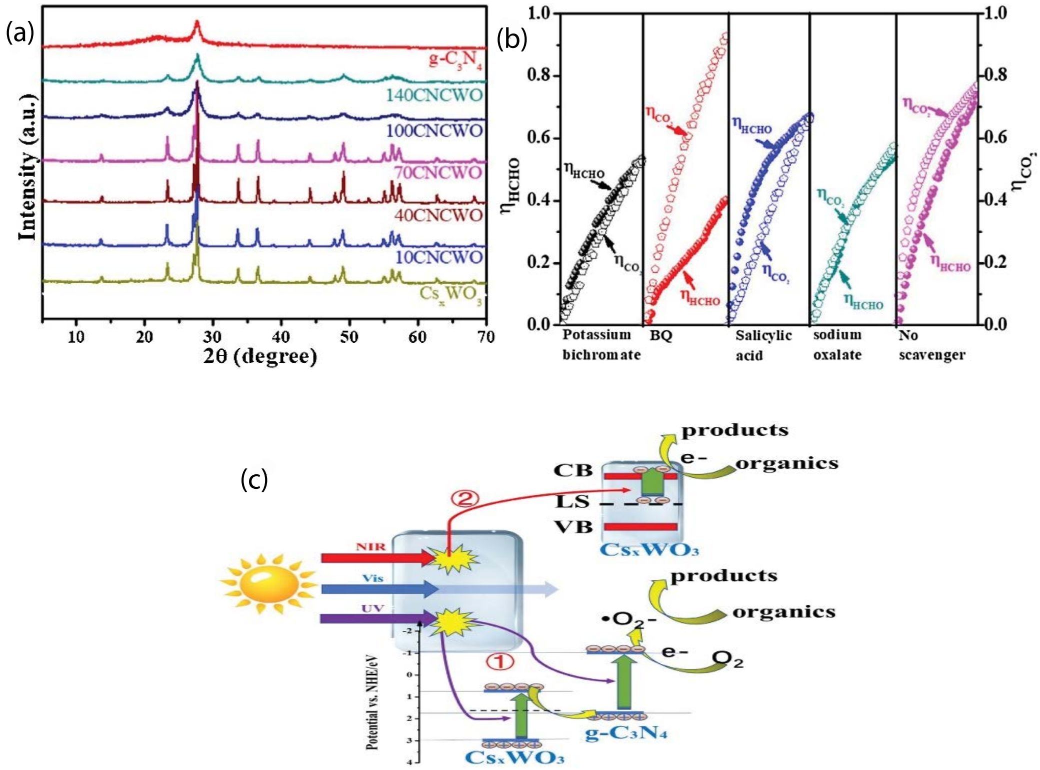

Fig. 19. (a) XRD patterns of prepared samples, (b) trapping experiments of active species while degradation of HCHO over 40CNCWO and (c) propose Z-scheme of CNCWO heterostructure [189].

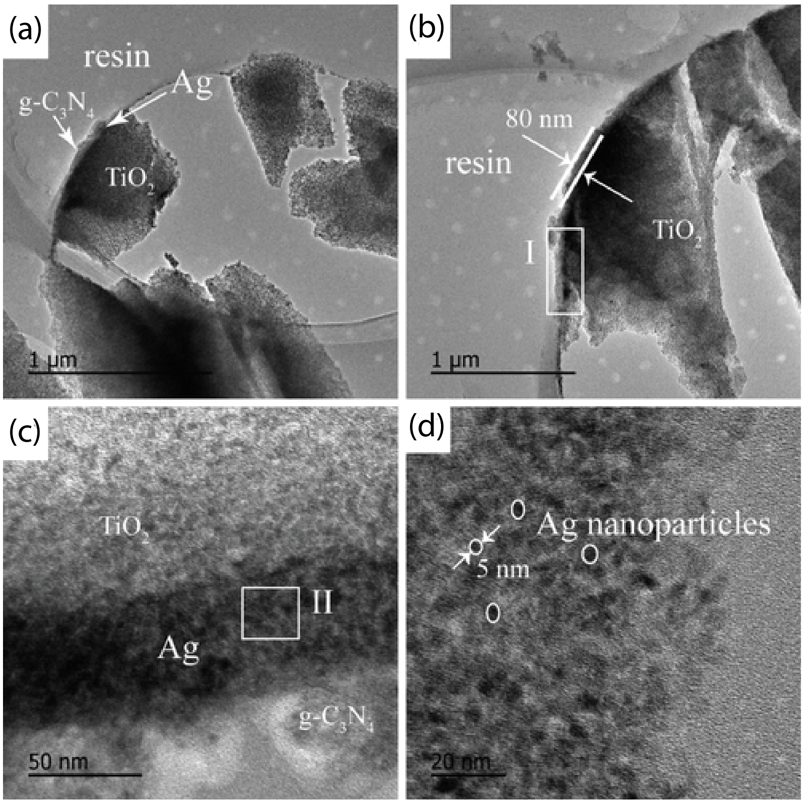

Fig. 20. TEM images of g-C_3N_4 (4%)/Ag/TiO_2 microspheres composite photocatalyst, (a and b) broken section of the microsphere and (c and d) enlarged view area I and II [190].

PL emission demonstrated peaks of all prepared samples and indicated that the intensity peaks of g-C_3N_4/TiO_2 microspheres, Ag/TiO_2 microspheres and g-C_3N_4 (4%)/Ag/TiO_2 composite were much lower than g-C_3N_4. Specifically, the g-C_3N_4 (4%)/Ag/TiO_2 hetero-composite illustrates that the no emission peak at a wavelength of 460 nm, indicating the minimum recombination rate of electron-hole pairs that led to the highest photoactivity.

In another report, Gong et al. [191] used Ag noble metal as an electron mediator in the preparation of Ag_2CrO_4/Ag/g-C_3N_4 composite synthesized by facile in-situ growth route and photoreduction technique. The nanocomposite showed that the photoactivity of the degradation of 2,4-dichlorophenol (2,4-DCP) was about 5.2 times higher than over single g-C_3N_4 due to the impact of photogenerated electrons in the CB which reacted with the Ag^+ to form a metallic Ag. The presence of metallic Ag at the composite supported the heterojunction between Ag_2CrO_4 and g-C_3N_4 to operate as an electron mediator for the photogenerated charges. The transient photocurrent response for the photoelectrochemical analysis of the prepared samples is shown in Fig. 21a. Obviously, the photocurrent intensity of Ag_2CrO_4/Ag/g-C_3N_4 (ACN) was about 4.4 times higher than that of the g-C_3N_4 electrode. Furthermore, the electrochemical impedance spectroscopy (EIS) of the photo-composite reveals a lower charge transfer resistance and photogenerated charge recombination rate when compared to g-C_3N_4 as illustrated in Fig. 21b.

In addition, the degradation of 2,4-DCP under visible light irradiation (λ > 420 nm) over-prepared samples are shown in Fig. 21c. Apparently, the degradation efficiency increased gradually as the Ag_2CrO_4 nanoparticles loading was increased from 1%–10% in the composite, then it decreased when the content was increased to 30% in the composite. Additionally, the 10 ACN composite showed the highest photocatalytic activity among all different synthesized samples. Further, confirmed by the mineralization of 2,4-DCP in the photodegradation process indicated the change of total organic carbon concentration (TOC) as shown in Fig. 21d. The TOC removal by 10 ACN composite achieved 62% after 2 h reaction time compared to 19% removal over pure g-C_3N_4.

Fig. 22 depicts the mechanism of the photocatalytic degradation of 2,4-DCP over Ag_2CrO/Ag/g-C_3N_4 (ACN) composite. The photoexcited electrons in the CB of Ag_2CrO_4 were transferred through the metallic Ag and to the holes in the VB of g-C_3N_4. Meanwhile, the O_2 adsorbed on the surface of g-C_3N_4 reduced to $^{\bullet}O_2^-$ by the electrons in the CB and reacts with 2,4-DCP that was mineralized to CO_2 and H_2O. Besides, the photogenerated holes in VB of Ag_2CrO_4 further degraded the organic pollutant into CO_2 and water. The Ag nanoparticles played a significant role in the enhancement of the photocatalytic activity by serving as a redox mediator and minimizing the electron-hole recombination.

The efficient photocatalysts by hybrid materials need to be enhanced in the three main aspects: (i) heterojunction formation between the two or more content materials, (ii) strong visible light absorption and (iii) superior separation of photoinduced electron-hole pairs. Ren et al. [192] synthesized

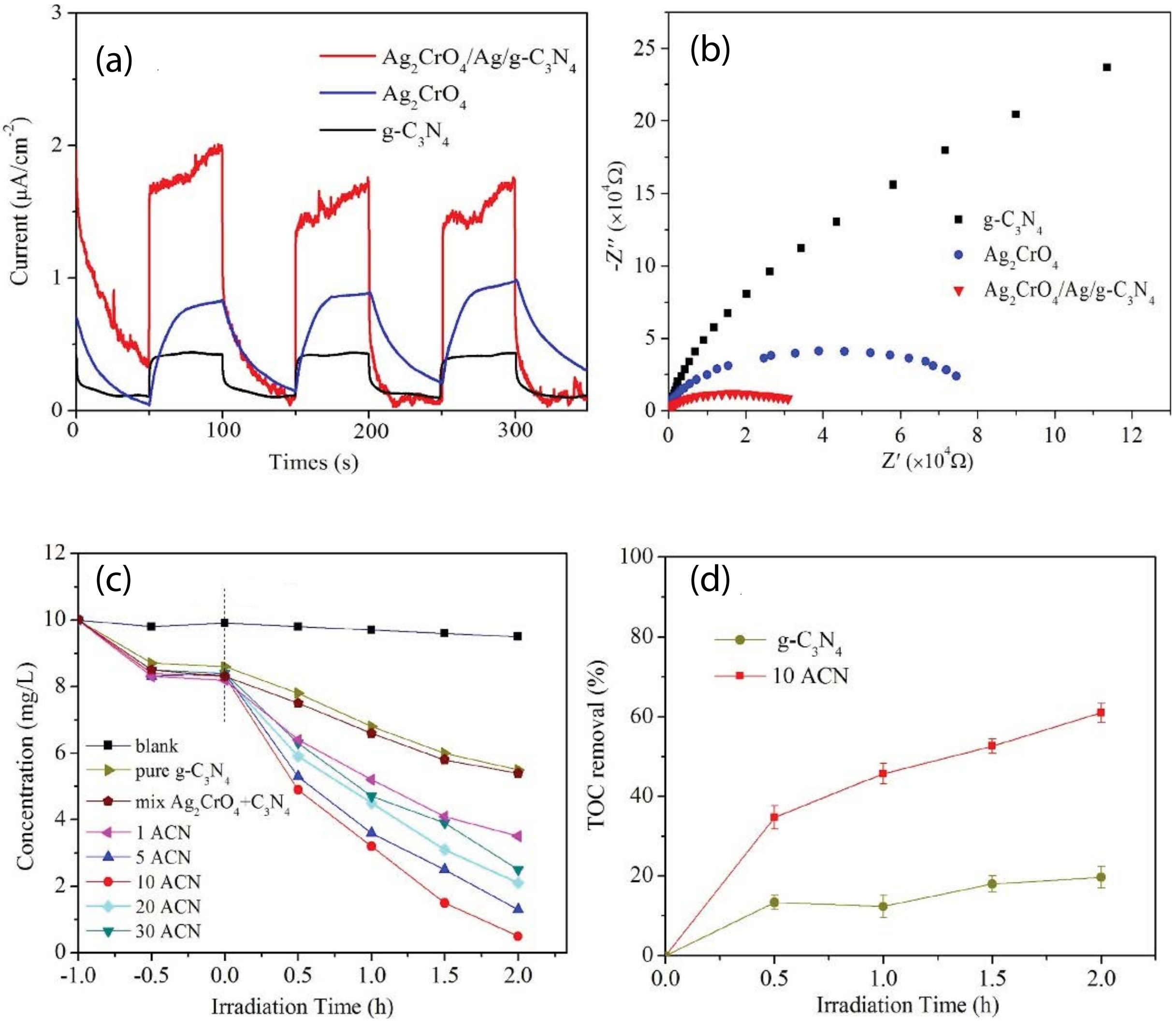

Fig. 21. (a) Transient photocurrent density and (b) EIS of different samples electrodes, (c) photocatalytic activities of the 2,4-DCP degradation over prepared samples under visible light irradiation and (d) TOC removal during mineralization of 2,4-DCP [191].

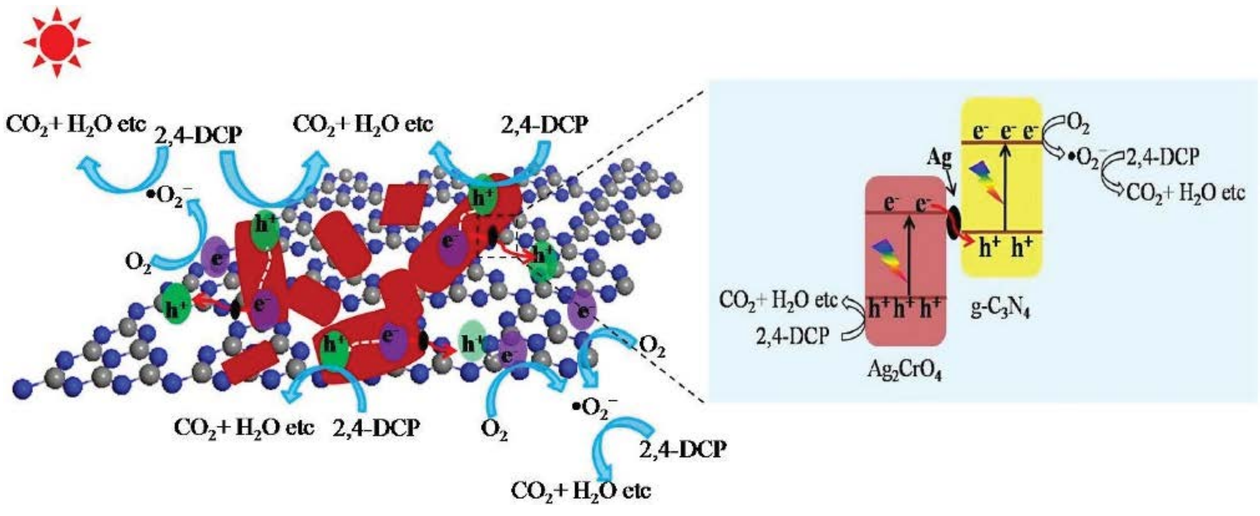

Fig. 22. The possible Z-schematic mechanism of the photodegradation of 2,4-DCP over ACN under the visible light irradiations [191].

$Ag_2O/g\text{-}C_3N_4$ composites by chemical precipitation process forming p-n heterojunction photocatalyst.

The optical properties of the prepared $g\text{-}C_3N_4$, Ag_2O and $Ag_2O/g\text{-}C_3N_4$ composites were characterized by UV-Vis DRS. Fig. 23a shows the substantial response after adding Ag_2O into $g\text{-}C_3N_4$. The composite of the 8:1 mass ratio of the $Ag_2O/g\text{-}C_3N_4$ sample revealed a long-range of light absorption compared to the other samples. Furthermore, the PL spectra investigation at the wavelength of 325 nm for the mitigation, transfer and recombination of the photogenerated electron-hole pairs for the synthesized materials is illustrated in Fig. 23b. The existence of Ag_2O in the composites reduced the intensity of PL emission when compared to $g\text{-}C_3N_4$, which indicated the efficient charge carrier separation in the $Ag_2O/g\text{-}C_3N_4$ hetero-junction.

Limiting the fast recombination rate of electron-hole pairs during the photocatalytic process would be essential for enhancing the absorption of solar light and photocatalytic activity. Bismuth doped graphitic carbon nitride photocatalyst applied for the degradation of environmental pollutants. Zou et al. [193] prepare $BiPO_4/g\text{-}C_3N_4$ nanocomposites by hydrothermal method with simple calcination to improve the stability and efficient absorption of visible light during photodegradation of benzene. Fig. 24a shows the higher conversion (73%) of gaseous benzene over 2 wt% $BiPO_4/g\text{-}C_3N_4$ (Bi-CN) composite after 4 h under visible light irradiation. In contrast, the $BiPO_4$ and $g\text{-}C_3N_4$ samples showed a low photoactivity conversion of benzene of 2% and 11%, respectively. Moreover, the benzene decomposition reaction followed a pseudo-first-order kinetic model with the highest rate constant of about 0.316 h^{-1} over the 2wt% Bi-CN sample as shown in Fig. 24b. In addition, the photodegradation of benzene over 2wt% Bi-CN photocatalyst exhibited more stability until 4-cycles and after 16 h under visible light Fig. 24c.

Likewise, the PL spectroscopy to measure the contribution of the photogenerated (e^-/h^+) of the $g\text{-}C_3N_4$ and the Bi-CN composites with different amount of $BiPO_4$ is shown in Fig. 24d. A high recombination rate indicated PL emission for the $g\text{-}C_3N_4$ sample was observed. However, it was clear that the PL intensity decreased for the Bi-CN samples due to the heterojunction which minimizes the recombination of charge carriers during the photocatalytic reaction. Furthermore, the ESR technique was used to indicate the active species during photodegradation. As shown in Fig. 25a, over 2 wt% Bi-CN, four intensive peaks of DMPO-$^{\bullet}OH$ (aqueous dispersion) were detected, and the other six peaks of DMPO-$O_2^{\bullet-}$ (methanol dispersion) were indicated under the visible light irradiation (Fig. 25b). Consequently, both $^{\bullet}OH$ and $O_2^{\bullet-}$ active species were delivered on the surface of Bi-CN.

Fig. 25c illustrates the proposed photocatalytic process for the degradation of benzene over $BiPO_4/g\text{-}C_3N_4$ (Bi-CN) composite under visible light irradiation. The photogenerated electrons in the CB of $g\text{-}C_3N_4$ can be transferred into $BiPO_4$ nanoparticles to accumulate and react with oxygen and water to form $^{\bullet}OH$ and $^{\bullet}O_2^-$ reactive species. Meanwhile, the photogenerated holes in VB of $g\text{-}C_3N_4$ will mineralize the gaseous benzene into CO_2 and water.

According to He et al. [194], bismuth(III) oxide (Bi_2O_3) nanoparticles were fabricated with $g\text{-}C_3N_4$ at room temperature through in situ deposition of quantum-sized nanoparticles forming $Bi_2O_3/g\text{-}C_3N_4$ composite. The morphology suggested no change in $g\text{-}C_3N_4$ samples after deposition of Bi_2O_3. However, the EDX analysis confirmed the presence of Bi and O elements in the composite, which illustrates the deposition of Bi_2O_3 on $g\text{-}C_3N_4$. Moreover, the UV-Vis DRS of the prepared samples showed very close absorption edges for $g\text{-}C_3N_4$ and $Bi_2O_3/g\text{-}C_3N_4$ of 441 and 442, respectively. This indicated that a small amount of Bi_2O_3 nanoparticles would not affect the visible light absorption of $g\text{-}C_3N_4$ in the composite.

The photocatalytic performances of the synthesized samples were evaluated by the degradation of phenol under the visible light irradiation ($\lambda > 400$ nm) as shown in Fig. 26a. Apparently, the $Bi_2O_3/g\text{-}C_3N_4$ composite exhibited a better photodegradation ability than pure Bi_2O_3 and $g\text{-}C_3N_4$. The change of UV spectra of phenol degradation over $Bi_2O_3/g\text{-}C_3N_4$ composite indicated that degradation of phenol due to the heterojunction formation between the $g\text{-}C_3N_4$ and Bi_2O_3 (Fig. 26b). In addition, the proposed mechanism of the

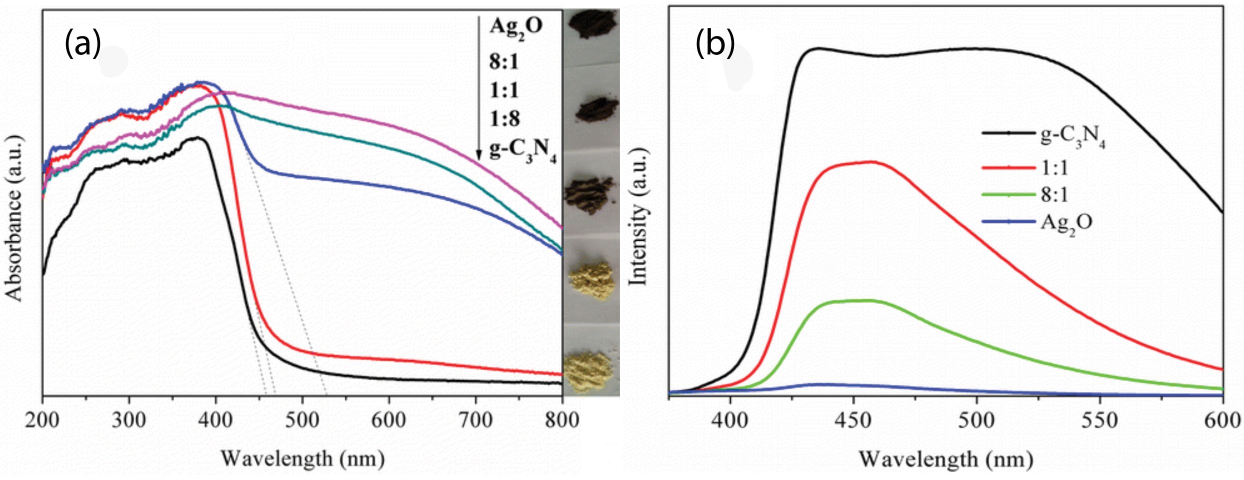

Fig. 23. (a) UV-Vis DRS spectra and (b) PL spectra for the prepared samples of $g\text{-}C_3N_4$, Ag_2O and $Ag_2O/g\text{-}C_3N_4$ with different mass ratios [192].

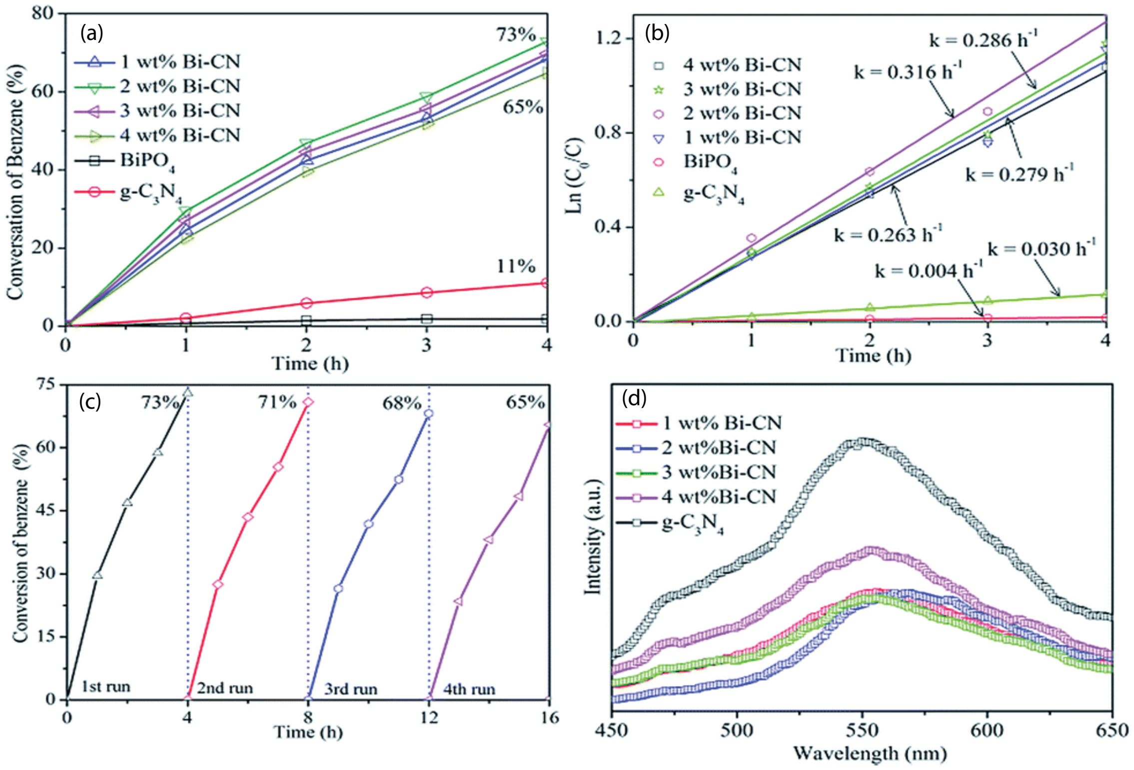

Fig. 24. (a) Photodegradation of benzene and (b) kinetic curve over pure g-C_3N_4, $BiPO_4$ and (1%–5%) Bi-CN composites, (c) cyclic photodegradation of benzene over 2wt% Bi-CN under visible light irradiation and (d) PL spectra of the prepared samples [193].

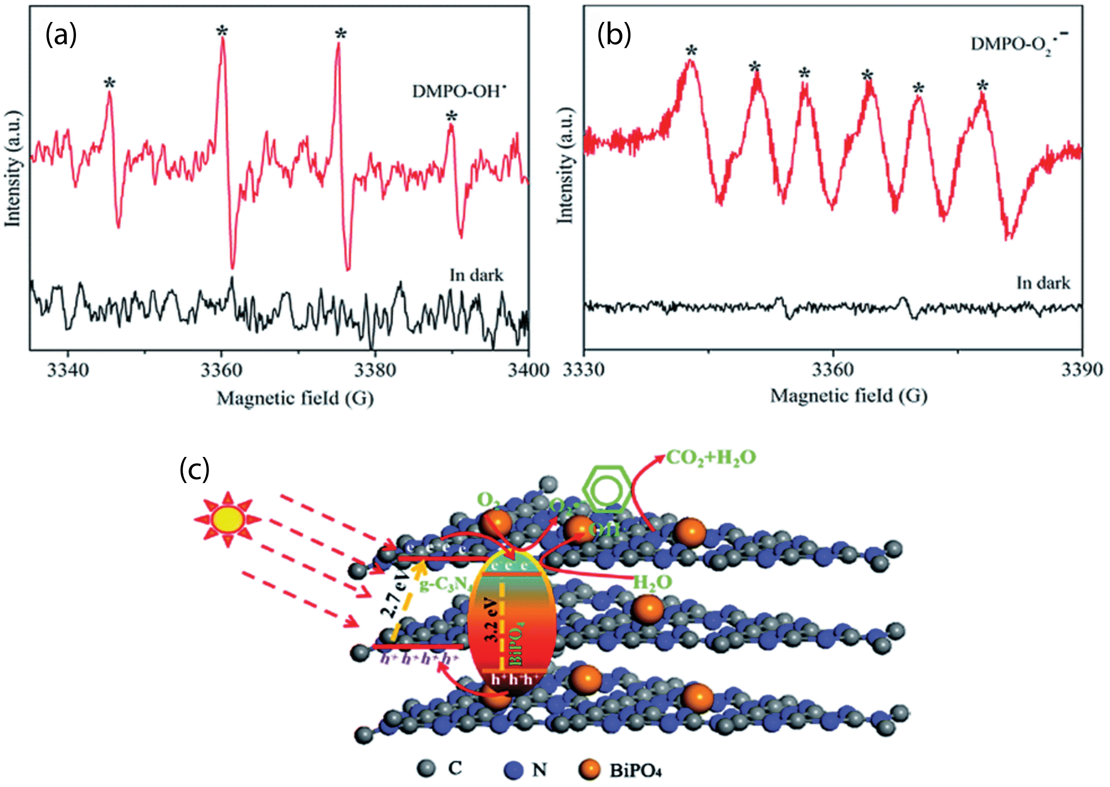

Fig. 25. A possible scheme of the photocatalytic mechanism of photodegradation of benzene over Bi-CN composite [193].

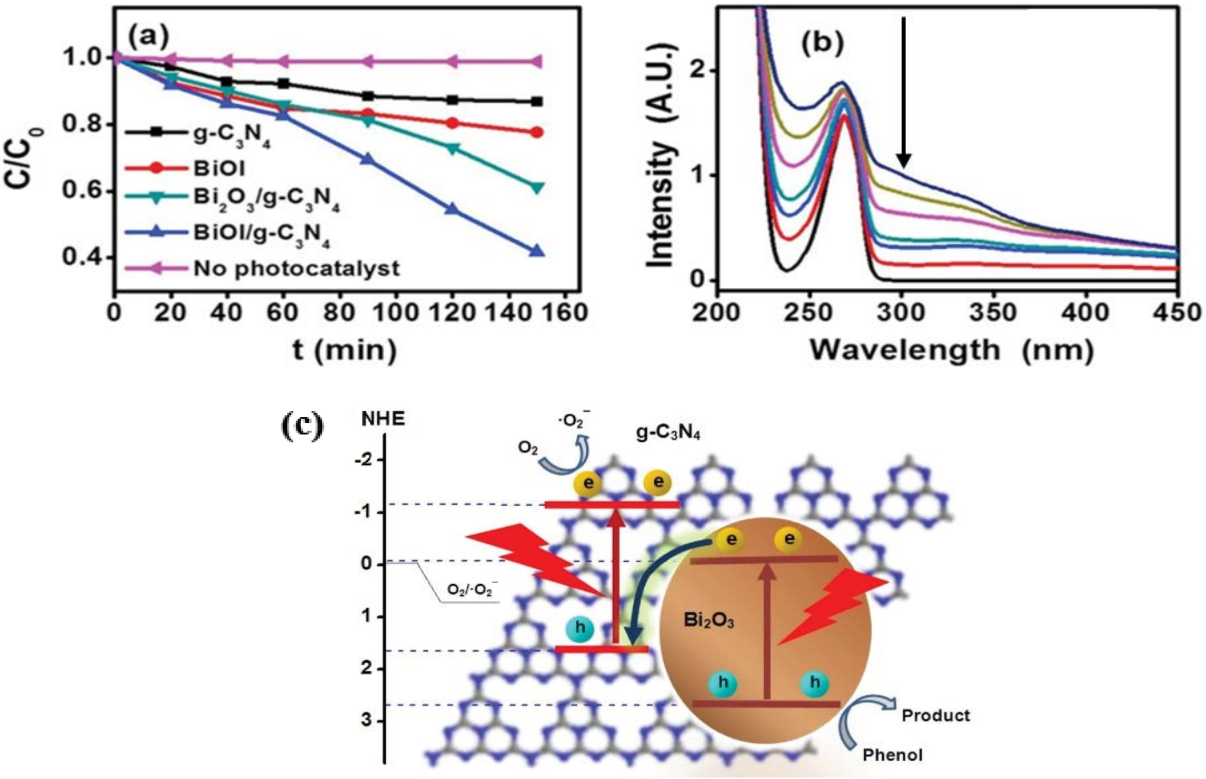

Fig. 26. (a) Degradation of phenol over Bi_2O_3, g-C_3N_4 and Bi_2O_3/g-C_3N_4 composite under the visible light irradiation, (b) UV absorption spectra of phenol over Bi_2O_3/g-C_3N_4 after the visible light irradiation and (c) Z-scheme mechanism of Bi_2O_3/g-C_3N_4 composite [194].

Z-scheme heterojunction in the Bi_2O_3/g-C_3N_4 composite is demonstrated in Fig. 26c. The photogenerated electrons in the CB of Bi_2O_3 were transferred to the VB of the g-C_3N_4 and the electrons in the CB of g-C_3N_4 reacted with O_2 and form $O_2^{\bullet-}$ radicals. In addition, the positive holes in the VB of Bi_2O_3 reacted with phenol molecules leading to oxidation of phenol into water and CO_2.

Dao et al. [195] reported a conjugate semiconductor g-C_3N_4 combined with $NiWO_4$ to form g-C_3N_4/$NiWO_4$ (C/N) composite with different mole ratios for photocatalytic degradation of gaseous toluene. In the XRD patterns of the C/N with mole ratios 1:1, the peaks in Fig. 27a matched with the XRD peaks of $NiWO_4$ material and pure g-C_3N_4 with a shift to a higher angle for the (002) peak. The UV-Vis absorption spectra of g-C_3N_4, $NiWO_4$ and the different composite ratios of g-C_3N_4/$NiWO_4$ materials are shown in Fig. 27b. In addition, it indicates that the visible light absorption of the (C/N) composite was higher than pure g-C_3N_4 and un-combined $NiWO_4$. Further, the estimated bandgaps for the 1C/1N, 1C/2N and 2C/1N composites were 2.25, 2.37 and 2.44 eV respectively, whereas for the g-C_3N_4 and $NiWO_4$ materials the bandgaps were 2.65 and 2.53 eV, respectively.

The PL intensity for the g-C_3N_4/$NiWO_3$ was lower compared to pure g-C_3N_4 and $NiWO_4$. It was due to an effective increase in the lifetime of the photoexcited electron–hole pairs with a lower recombination rate. Additionally, the photoelectrochemical properties for the synthesized samples were stimulated by photocurrent response. No peaks were noticed in the dark condition, but the photocurrent responded after the light excitation due to the electrons and holes production. Obviously, the photocurrent responses for the C/N samples were higher than those of g-C_3N_4 and $NiWO_4$, which could be ascribed to photoexcited electrons and holes recombination in the pure materials. Furthermore, the 1C/1N composite demonstrated the highest photocurrent response among all the prepared materials.

A photolysis experiment was conducted without adding toluene. Fig. 28a shows the removal efficiency and mineralization of toluene over the prepared samples under dark conditions for 60 min and visible light irradiation for 120 min. The 1C/1N photocatalyst demonstrates the maximum removal (95.3%) and mineralization (99.1%) of toluene among all the materials. Moreover, the prepared C/N materials manifested higher stability during photocatalytic degradation of toluene as shown in Fig. 28b.

Research on In_2S_3 nanoform and its composites was synthesized by hydrothermal route for photodegradation of toluene by Zhang et al. [196]. The characterization by the XRD in Fig. 29a shows the presence of four peaks of In_2S_3 that matched the standard of JCPDS NO.25-0390. In addition, the obvious diffraction peaks at 27.5° ascribed to the g-C_3N_4 crystal phase were observed. Moreover, all the peaks of both compounds were indicated in the In_2S_3/g-C_3N_4 composites samples.

The different amount of In_2S_3 compound (20%–60%) in the composite showed higher photocatalytic-degradation of toluene than pure g-C_3N_4 and In_2S_3. However, the optimum amount of 40% In_2S_3/g-C_3N_4 composite displayed the highest degradation efficiency of toluene (86.7%) as shown

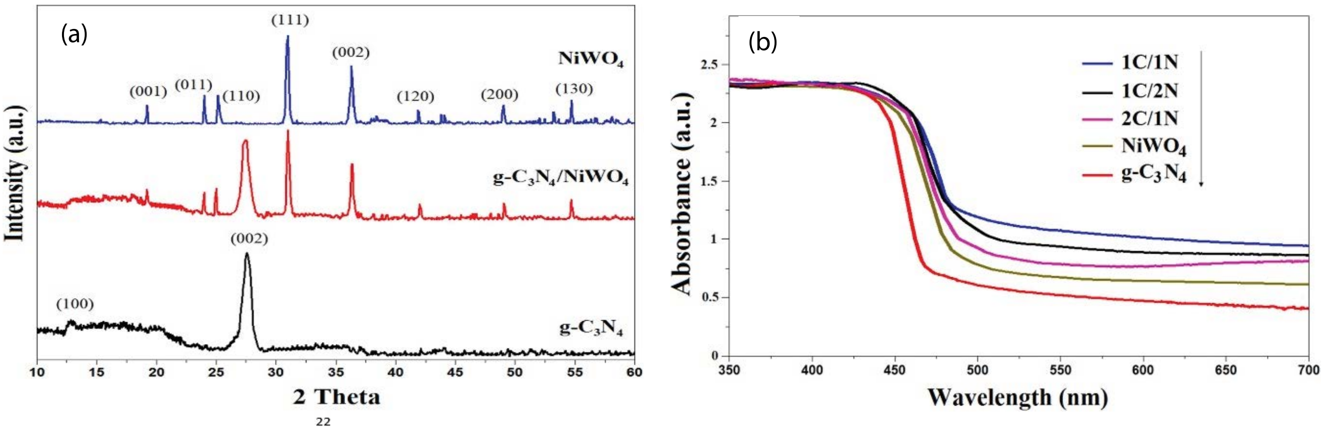

Fig. 27. (a) XRD patterns and (b) UV-Vis absorption spectra of the prepared photocatalysts [195].

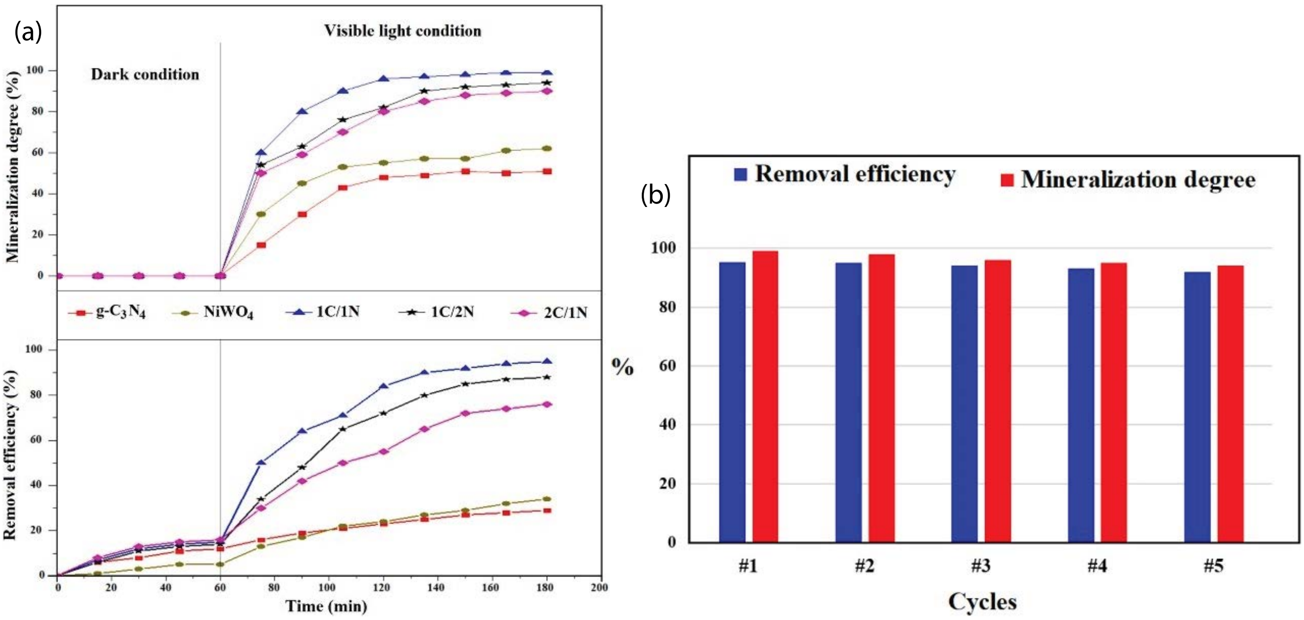

Fig. 28. (a) Removal efficiency and mineralization measurements of toluene over g-C_3N_4, $NiWO_4$ and C/N materials in and (b) cyclic stability of both processes over the 1C/1N photocatalyst [195].

in Fig. 29b. The textural morphology of the prepared samples characterized by SEM analysis demonstrated that the In_2S_3 material had a particle size of about 20 nm with some agglomerates phase. Moreover, the In_2S_3 particles were distributed in the lamellar two-dimensional g-C_3N_4 to form the In_2S_3/g-C_3N_4 composite.

The photo-induced electrons and holes recombination rate effects the degradation process and from Fig. 30a, the photocurrent density of the pure In_2S_3 was about 3.7 μA/cm^2, but it reached about 7.8 μA/cm^2 for the 40% In_2S_3/g-C_3N_4 heterojunction. That reflects the enhancement in the charge separation to minimize the recombination rate. Moreover, the PL intensities for pure In_2S_3 and g-C_3N_4 were greater than that of 40% In_2S_3/g-C_3N_4 composite as shown in Fig. 30b, which confirmed the efficient movement of the charge carriers to boost the photocatalytic process. Furthermore, the possible photodegradation mechanism over 40% In_2S_3/g-C_3N_4 composite is illustrated in Fig. 30c. The irradiation with light generates electrons in the conduction band of g-C_3N_4, that excited the conduction band of In_2S_3. Consequently, the holes can transfer from the valance band of In_2S_3 to the valance band of g-C_3N_4, where water molecules oxidize them to form extra holes and O_2. The electrons in the In_2S_3 may combine with the oxygen to produce $O_2^{\bullet-}$ superoxide anions, that can react with toluene in a redox reaction to form CO_2 and H_2O.

The fabrication of composite materials of BiOI quantum dots on the surface of g-C_3N_4 nanosheets formed a Z-scheme configuration to enhance the photocatalytic activity for the degradation of phenol was also reported [197]. The heterojunction allowed electron-hole transfer in integral electric field between the interfaces of the combined materials.

The FESEM images for morphology characterization hierarchical textural shape comprised of regular nanoplates and the Bi_2O_3/g-C_3N_4 and BiOI/g-C_3N_4 showed similar

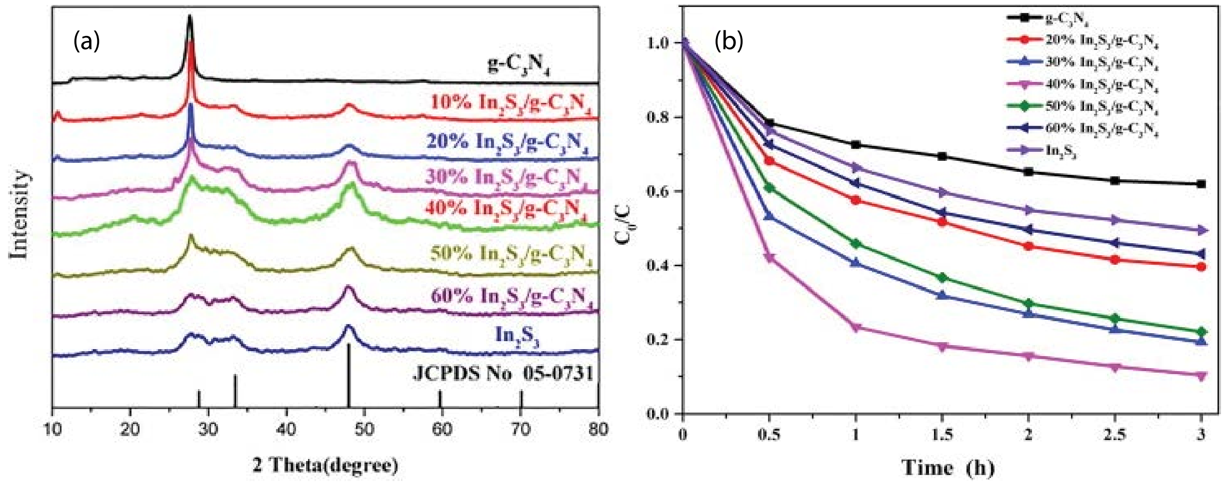

Fig. 29. a) XRD patterns and (b) photocatalytic degradation of toluene by the prepared pure g-C_3N_4, pure In_2S_3 and In_2S_3/g-C_3N_4 composites [196].

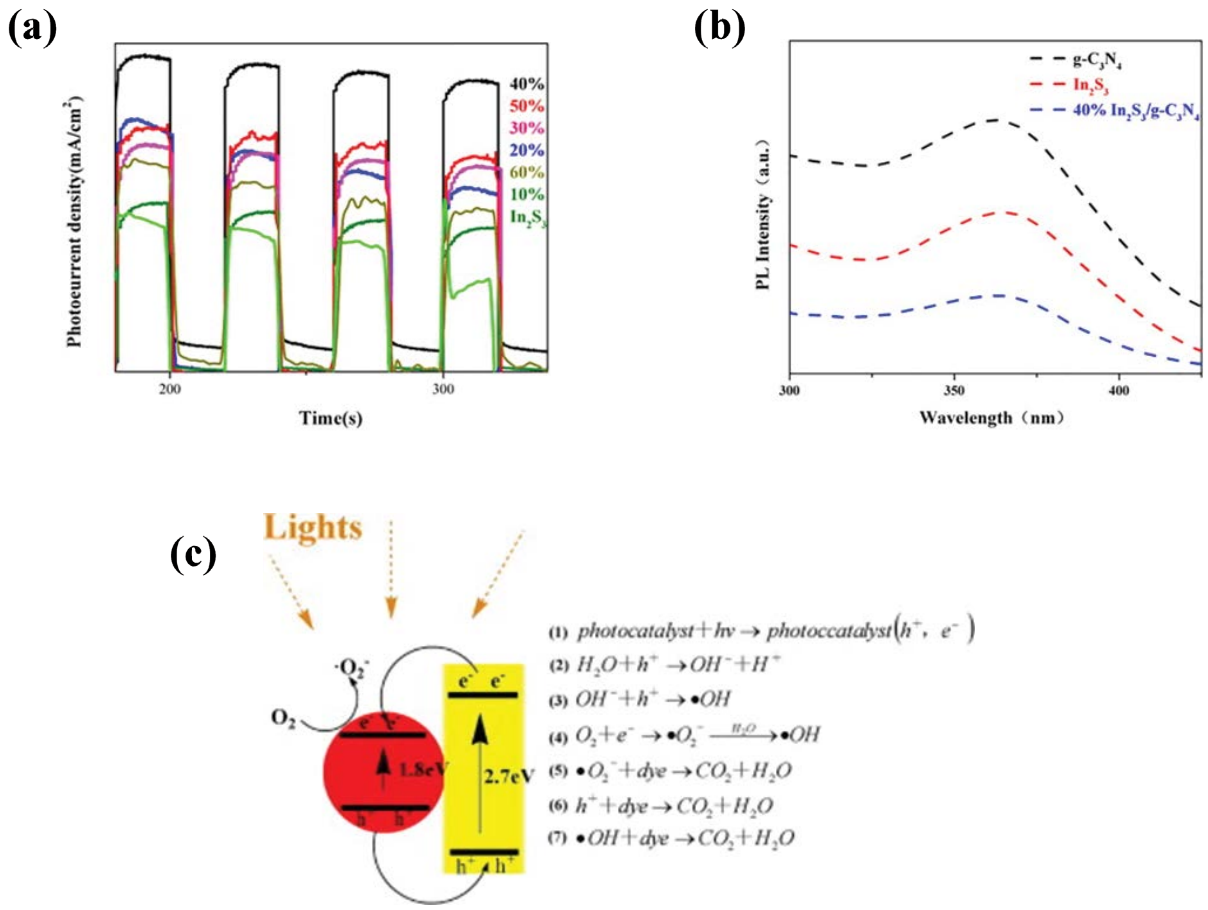

Fig. 30. (a) The photocurrent density and (b) PL spectra of In_2S_3, g-C_3N_4 and 40% In_2S_3/g-C_3N_4 composite and (c) photocatalytic mechanism over In_2S_3/g-C_3N_4 composite under visible light irradiation [196].

morphology which indicated that both BiOI and Bi_2O_3 materials had no impact on the surface of g-C_3N_4.

The X-ray photoelectron spectroscopy (XPS) chemical composition analysis spectra for the prepared samples are shown in Fig. 31. The survey spectrum of the BiOI/g-C_3N_4 showed peaks of C, N, Bi, O and I, which were confirmed with those of pristine BiOI and g-C_3N_4 (Fig. 31a). Fig. 31b shows the binding energy of Bi orbitals in the BiOI, which were shifted due to the electron transfer from BiOI to g-C_3N_4. Furthermore, the redshift of the energy level in the g-C_3N_4 after coupling was attributed to increase in the electron density on the C atom of the g-C_3N_4 as illustrated in Fig. 31c. Moreover, Fig. 31d reveals that the N 1s binding energies shifted to 398.7, 400.0 and 404.3 eV due to the increase in the electron density in the N atoms after forming BiOI/g-C_3N_4 composite and indicated that the electrons were transferred from BiOI to g-C_3N_4.

Fig. 32a illustrates that the BiOI had higher photocatalytic activity for phenol degradation under LED light irradiation when compared to pure g-C_3N_4, that could be ascribed to lower energy valance band and further narrowing of the bandgap, but the BiOI/g-C_3N_4 composite had the highest performance. Also, the UV-Vis spectra evaluation of phenol solution over BiOI/g-C_3N_4 photocatalyst is demonstrated in Fig. 32b. Obviously, the rapid enhancement of the photocatalytic activity of BiOI/g-C_3N_4 heterojunction might be attributed to the migration of the charges in the two coupled materials, increasing in the light absorption and the specific surface area. The migration of electrons as a result of formation of heterojunction between the BiOI surface and the g-C_3N_4 nanosheets by moving the electrons from the conducting band (CB) of BiOI to valence band (VB) of g-C_3N_4 was endorsed by the established internal electric filed (IEF). Fig. 32c, shows the Z-scheme where the electrons form the CB of g-C_3N_4 and holes on the VB of BiOI were involved in the photocatalytic degradation process of phenol.

7. Some challenges of VOCs elimination by photocatalysis

While photocatalysis utilising semiconductor nanoparticles is one of the most investigated environmental nanotechnologies for air purification because it can decompose VOCs directly into harmless CO_2 and H_2O under ambient conditions, there are still some challenges with the technology. Photocatalysis can be particularly suitable for removing low concentration pollutants (sub-ppm levels) in indoor environments where conventional adsorption technologies are not very efficient. In addition, there is still need to (1) increase visible light activity to utilize abundantly available solar light and (2) preventing catalyst deactivation that hinders long-term usage of photocatalysts [198]. Another challenge is that the one-size-fits all principle does not work with environments polluted with different kinds of VOCs as the effectiveness of the photocatalysts differs from pollutant to pollutant. There is therefore need for further investigations into the optimisation of the different parameters that influence photocatalyst performance as well as pilot scale systems for large scale application of the technology.

8. Conclusion and future perspectives

In conclusion, the huge emission of the VOCs pollutant has many influences in our environment. That could raise the needs to improve effective treatment methods as well as active martials. Semiconductor materials can be used to solve many environmental pollution issues due to the unique photochemical redox properties. The g-C_3N_4 has exhibited great potential as a visible-light-driven photocatalyst for various environmental applications including degradation of VOCs because of its easy synthesis, metal-free nature, favourable electronic band structure and environmentally benign properties. The photocatalytic properties of g-C_3N_4 based photocatalysts can be improved by tuning the structure of the photocatalyst in order to enable light absorption in the visible-light region,

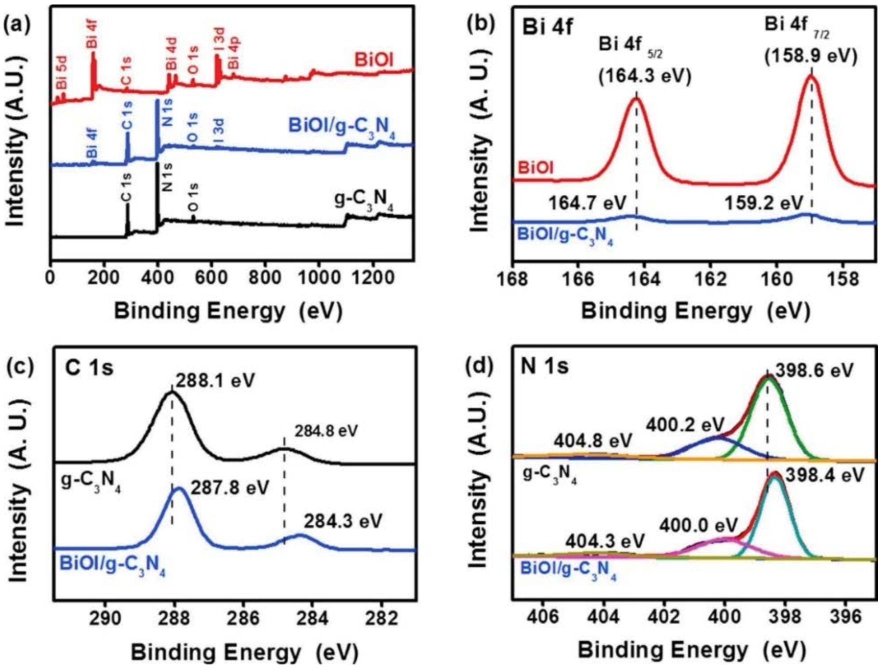

Fig. 31. XPS spectra of the prepare samples: (a) survey spectra, (b) Bi 4f, (c) C 1s and (d) N 1s [197].

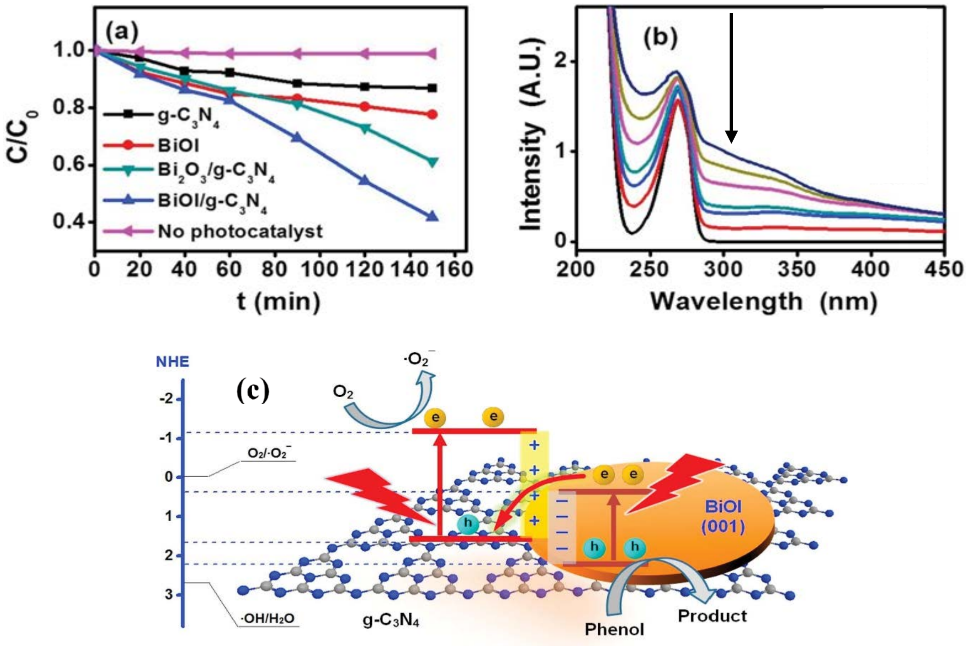

Fig. 32. (a) The phenol degradation over the BiOI, g-C_3N_4, Bi_2O_3/g-C_3N_4 and Bi_2O_3/g-C_3N_4 under the LED lamp (λ > 400), (b) UV-Vis spectra evaluation of phenol solution by BiOI/g-C_3N_4 photocatalyst and (c) proposed Z-scheme for the charge migration of the BiOI/g-C_3N_4 composite [197].

reducing the rate of recombination of photogenerated charge carriers, increasing the number of active sites on photocatalyst surfaces and increasing the surface area for pollutant adsorption. Several engineering strategies such as elemental doping, and formation of heterojunctions with other photocatalysts, have recently attracted a lot of attention as potential strategies to improve the photocatalytic properties of g-C_3N_4. However, g-C_3N_4 based photocatalysts still suffer from inherent drawbacks such as low photocatalytic performance and low visible-light harvesting properties, which hinder practical applications. It is thus important to modify g-C_3N_4 based photocatalysts to meet the practical demands of VOCs degradation in various indoor and outdoor environments. The metal free graphitic carbon nitride g-C_3N_4 can be coupled with other organic or inorganic active compounds to enhance the solar light absorption, narrow the band gab and reduce the charge carrier recombination rate. The nature of dopant materials, amount of doping and the preparation methods are crucial for photocatalytic properties. The g-C_3N_4 composites photocatalysts have demonstrated a fascinating capacity during the photocatalysis processes for VOCs degradation. The abundant availability, the renewable source of solar light and the ability to recover photocatalytic performance of g-C_3N_4 composites would extrapolate the future demand in the environmental remediation studies.

In perspective, a further development of efficient g-C_3N_4 based photocatalysts for VOCs removal are needed for applications especially in water treatment. Improving the synthesis procedure of the g-C_3N_4 composites require deep understanding of the reaction mechanisms. Reducing the drawbacks including minor optical adsorption characteristics, low rate of charge carriers and less specific surface area requires more research investigations. This can be overcome by jointing efforts from different research fields focusing on improving the photocatalytic efficiency and stability of the g-C_3N_4 based photocatalysts.

References

[1] L. Zhong, J.J. Brancho, S. Batterman, B.M. Bartlett, C. Godwin, Experimental and modeling study of visible light responsive photocatalytic oxidation (PCO) materials for toluene degradation, Appl. Catal., B, 216 (2017) 122–132.

[2] W. Zou, B. Gao, Y.S. Ok, L. Dong, Integrated adsorption and photocatalytic degradation of volatile organic compounds (VOCs) using carbon-based nanocomposites: a critical review, Chemosphere, 218 (2019) 845–859.

[3] R. Xie, J. Ji, K. Guo, D. Lei, Q. Fan, D.Y. Leung, H. Huang, Wet scrubber coupled with UV/PMS process for efficient removal of gaseous VOCs: roles of sulfate and hydroxyl radicals, Chem. Eng. J., 356 (2019) 632–640.

[4] Y. Shu, Y. Xu, H. Huang, J. Ji, S. Liang, M. Wu, D.Y. Leung, Catalytic oxidation of VOCs over Mn/TiO_2/activated carbon under 185 nm VUV irradiation, Chemosphere, 208 (2018) 550–558.

[5] A.C. Rai, P. Kumar, F. Pilla, A.N. Skouloudis, S. Di Sabatino, C. Ratti, D. Rickerby, End-user perspective of low-cost sensors for outdoor air pollution monitoring, Sci. Total Environ., 607 (2017) 691–705.

[6] F.I. Khan, A.K. Ghoshal, Removal of volatile organic compounds from polluted air, J. Loss Prev. Process Ind., 13 (2000) 527–545.

[7] L. Zhong, F. Haghighat, P. Blondeau, J. Kozinski, Modeling and physical interpretation of photocatalytic oxidation efficiency in indoor air applications, Build. Environ., 45 (2010) 2689–2697.

[8] L. Lin, Y. Chai, B. Zhao, W. Wei, D. He, B. He, Q. Tang, Photocatalytic oxidation for degradation of VOCs, Open J. Inorg. Chem., 3 (2013) 14–25.

[9] H. Zangeneh, A.A.L. Zinatizadeh, M. Habibi, M. Akia, M.H. Isa, Photocatalytic oxidation of organic dyes and pollutants in wastewater using different modified titanium dioxides: a comparative review, J. Ind. Eng. Chem., 26 (2015) 1–36.

[10] A.O. Ibhadon, P. Fitzpatrick, Heterogeneous photocatalysis: recent advances and applications, J. Catal., 3 (2013) 189–218.

[11] Y. Zhang, T. Mori, L. Niu, J. Ye, Non-covalent doping of graphitic carbon nitride polymer with graphene: controlled electronic structure and enhanced optoelectronic conversion, Energy Environ. Sci., 4 (2011) 4517–4521.

[12] L. Kong, J. Wang, F. Ma, M. Sun, J. Quan, Graphitic carbon nitride nanostructures: catalysis, Appl. Mater. Today, 16 (2019) 388–424.

[13] M.M. Fang, J.X. Shao, X.G. Huang, J.Y. Wang, W. Chen, Direct Z-scheme $CdFe_2O_4$/g-C_3N_4 hybrid photocatalysts for highly efficient ceftiofur sodium photodegradation, J. Mater. Sci. Technol., 56 (2020) 133–142.

[14] B. Shao, Z. Liu, G. Zeng, Z. Wu, Y. Liu, M. Cheng, H. Feng, Nitrogen-doped hollow mesoporous carbon spheres modified g-C_3N_4/Bi_2O_3 direct dual semiconductor photocatalytic system with enhanced antibiotics degradation under visible light, ACS Sustainable Chem. Eng., 6 (2018) 16424–16436.

[15] N.T.T. Truc, D.S. Duc, D. Van Thuan, T. Al Tahtamouni, T.D. Pham, N.T. Hanh, N.T.P. Le Chi, The advanced photocatalytic degradation of atrazine by direct Z-scheme Cu doped ZnO/g-C_3N_4, Appl. Surf. Sci., 489 (2019) 875–882.

[16] N.T.T. Truc, T.D. Pham, D. Van Thuan, D.T. Tran, M.V. Nguyen, N.M. Dang, H.T. Trang, Superior activity of Cu-$NiWO_4$/g-C_3N_4 Z direct system for photocatalytic decomposition of VOCs in aerosol under visible light, J. Alloys Compd., 798 (2019) 12–18.

[17] X. Wang, K. Maeda, X. Chen, K. Takanabe, K. Domen, Y. Hou, M. Antonietti, Polymer semiconductors for artificial photosynthesis: hydrogen evolution by mesoporous graphitic carbon nitride with visible light, J. Am. Chem. Soc., 131 (2009) 1680–1681.

[18] J. Wen, J. Xie, X. Chen, X. Li, A review on g-C_3N_4-based photocatalysts, Appl. Surf. Sci., 391 (2017) 72–123.

[19] X. Wang, S. Blechert, M. Antonietti, Polymeric graphitic carbon nitride for heterogeneous photocatalysis, ACS Catal., 2 (2012) 1596–1606.

[20] D.M. Teter, R.J. Hemley, Low-compressibility carbon nitrides, Science, 271 (1996) 53–55.

[21] B. Zhu, L. Zhang, B. Cheng, J. Yu, First-principle calculation study of tri-s-triazine-based g-C_3N_4: a review, Appl. Catal., B, 224 (2018) 983–999.

[22] Y. Xu, S.P. Gao, Bandgap of C_3N_4 in the GW approximation, Int. J. Hydrogen Energy, 37 (2012) 11072–11080.

[23] D. Masih, Y. Ma, S. Rohani, Graphitic C_3N_4 based noble-metal-free photocatalyst systems: a review, Appl. Catal., B, 206 (2017) 556–588.

[24] J. Fu, J. Yu, C. Jiang, B. Cheng, g-C_3N_4-Based heterostructured photocatalysts, Adv. Energy Mater., 8 (2018) 1701503, doi: 10.1002/aenm.201701503.

[25] D. Liang, T. Jing, Y. Ma, J. Hao, G. Sun, M. Deng, Photocatalytic properties of g-C_6N_6/g-C_3N_4 heterostructure: a theoretical study, J. Phys. Chem. C, 120 (2016) 24023–24029.

[26] Y. Ren, D. Zeng, W.J. Ong, Interfacial engineering of graphitic carbon nitride (g-C_3N_4)-based metal sulfide heterojunction photocatalysts for energy conversion: a review, Chin. J. Catal., 40 (2019) 289–319.

[27] C.M. Soukoulis, Ed., Photonic Bandgap Materials, Vol. 315, Springer Science & Business Media, Iowa, 2012.

[28] J. Low, J. Yu, M. Jaroniec, S. Wageh, A.A. Al-Ghamdi, Heterojunction photocatalysts, Adv. Mater., 29 (2017) 1601694, doi: 10.1002/adma.201601694.

[29] L.V. Bora, R. K, Mewada, Visible/solar light active photocatalysts for organic effluent treatment: fundamentals, mechanisms and parametric review, Renewable Sustainable Energy Rev., 76 (2017) 1393–1421.

[30] H. Katsumata, Y. Tachi, T. Suzuki, S. Kaneco, Z-scheme photocatalytic hydrogen production over WO_3/g-C_3N_4 composite photocatalysts, RSC Adv., 4 (2014) 21405–21409.

[31] W.J. Ong, L.L. Tan, Y.H. Ng, S.T. Yong, S.P. Chai, Graphitic carbon nitride (g-C_3N_4)-based photocatalysts for artificial photosynthesis and environmental remediation: are we a step closer to achieving sustainability?, Chem. Rev., 116 (2016) 7159–7329.

[32] A. Sudhaik, P. Raizada, P. Shandilya, D.Y. Jeong, J.H. Lim, P. Singh, Review on fabrication of graphitic carbon nitride based efficient nanocomposites for photodegradation of aqueous phase organic pollutants, J. Ind. Eng. Chem., 67 (2018) 28–51.

[33] H. Li, Z. Zhang, Y. Liu, W. Cen, X. Luo, Functional group effects on the HOMO–LUMO gap of g-C_3N_4, Nanomaterials, 8 (2018) 589, doi: 10.3390/nano8080589.

[34] Y. Zheng, Y. Jiao, Y. Zhu, L.H. Li, Y. Han, Y. Chen, S.Z. Qiao, Hydrogen evolution by a metal-free electrocatalyst, Nat. Commun., 5 (2014) 1–8.

[35] Z. Zhao, Y. Sun, F. Dong, Graphitic carbon nitride based nanocomposites: a review, Nanoscale, 7 (2015) 15–37.

[36] T.T. Pham, E.W. Shin, Influence of g-C_3N_4 precursors in g-C_3N_4/$NiTiO_3$ composites on photocatalytic behavior and the interconnection between g-C_3N_4 and $NiTiO_3$, Langmuir, 34 (2018) 13144–13154.

[37] L. Tang, C. Feng, Y. Deng, G. Zeng, J. Wang, Y. Liu, J. Wang, Enhanced photocatalytic activity of ternary Ag/g-C_3N_4/$NaTaO_3$ photocatalysts under wide spectrum light radiation: the high potential band protection mechanism, Appl. Catal., B, 230 (2018) 102–114.

[38] Q. Gu, Z. Gao, H. Zhao, Z. Lou, Y. Liao, C. Xue, Temperature-controlled morphology evolution of graphitic carbon nitride nanostructures and their photocatalytic activities under visible light, RSC Adv., 5 (2015) 49317–49325.

[39] Z. Mo, X. She, Y. Li, L. Liu, L. Huang, Z. Chen, H. Li, Synthesis of g-C_3N_4 at different temperatures for superior visible/UV photocatalytic performance and photoelectrochemical sensing of MB solution, RSC Adv., 5 (2015) 101552–101562.

[40] H. Yan, Y. Chen, S. Xu, Synthesis of graphitic carbon nitride by directly heating sulfuric acid treated melamine for enhanced photocatalytic H_2 production from water under visible light, Int. J. Hydrogen Energy, 37 (2012) 125–133.

[41] W. Ho, Z. Zhang, M. Xu, X. Zhang, X. Wang, Y. Huang, Enhanced visible-light-driven photocatalytic removal of NO: effect on layer distortion on g-C_3N_4 by H_2 heating, Appl. Catal., B, 179 (2015) 106–112.

[42] J. Chen, Z. Hong, Y. Chen, B. Lin, B. Gao, One-step synthesis of sulfur-doped and nitrogen-deficient g-C_3N_4 photocatalyst for enhanced hydrogen evolution under visible light, Mater. Lett., 145 (2015) 129–132.

[43] G. Wu, S.S. Thind, J. Wen, K. Yan, A. Chen, A novel nanoporous α-C_3N_4 photocatalyst with superior high visible light activity, Appl. Catal., B, 142 (2013) 590–597.

[44] Y. Zhang, J. Liu, G. Wu, W. Chen, Porous graphitic carbon nitride synthesized via direct polymerization of urea for efficient sunlight-driven photocatalytic hydrogen production, Nanoscale, 4 (2012) 5300–5303.

[45] J. Liu, T. Zhang, Z. Wang, G. Dawson, W. Chen, Simple pyrolysis of urea into graphitic carbon nitride with recyclable adsorption and photocatalytic activity, J. Mater. Chem., 21 (2011) 14398–14401.

[46] F. Dong, Z. Wang, Y. Sun, W.K. Ho, H. Zhang, Engineering the nanoarchitecture and texture of polymeric carbon nitride semiconductor for enhanced visible light photocatalytic activity, J. Colloid Interface Sci., 401 (2013) 70–79.

[47] P. Yang, J. Zhao, W. Qiao, L. Li, Z. Zhu, Ammonia-induced robust photocatalytic hydrogen evolution of graphitic carbon nitride, Nanoscale, 7 (2015) 18887–18890.

[48] D.J. Martin, K. Qiu, S.A. Shevlin, A.D. Handoko, X. Chen, Z. Guo, J. Tang, Highly efficient photocatalytic H_2 evolution from water using visible light and structure-controlled graphitic carbon nitride, Angew. Chem. Int. Ed., 53 (2014) 9240–9245.

[49] G. Zhang, J. Zhang, M. Zhang, X. Wang, Polycondensation of thiourea into carbon nitride semiconductors as visible light photocatalysts, J. Mater. Chem., 22 (2012) 8083–8091.

[50] Y. Cui, Z. Ding, P. Liu, M. Antonietti, X. Fu, X. Wang, Metal-free activation of H_2O_2 by g-C_3N_4 under visible light irradiation

for the degradation of organic pollutants, Phys. Chem. Chem. Phys., 14 (2012) 1455–1462.

[51] Y. Fang, X. Li, X. Wang, Synthesis of polymeric carbon nitride films with adhesive interfaces for solar water splitting devices, ACS Catal., 8 (2018) 8774–8780.

[52] Y. Cui, J. Zhang, G. Zhang, J. Huang, P. Liu, M. Antonietti, X. Wang, Synthesis of bulk and nanoporous carbon nitride polymers from ammonium thiocyanate for photocatalytic hydrogen evolution, J. Mater. Chem., 21 (2011) 13032–13039.

[53] L. Shi, L. Liang, F. Wang, J. Ma, J. Sun, Polycondensation of guanidine hydrochloride into a graphitic carbon nitride semiconductor with a large surface area as a visible light photocatalyst, Catal. Sci. Technol., 4 (2014) 3235–3243.

[54] B. Long, J. Lin, X. Wang, Thermally-induced desulfurization and conversion of guanidine thiocyanate into graphitic carbon nitride catalysts for hydrogen photosynthesis, J. Mater. Chem. A, 2 (2014) 2942–2951.

[55] Y. Wang, J. Yao, H. Li, D. Su, M. Antonietti, Highly selective hydrogenation of phenol and derivatives over a Pd@carbon nitride catalyst in aqueous media, J. Am. Chem. Soc., 133 (2011) 2362–2365.

[56] J. Liu, H. Wang, M. Antonietti, Graphitic carbon nitride "reloaded": emerging applications beyond (photo) catalysis, Chem. Soc. Rev., 45 (2016) 2308–2326.

[57] Y. He, L. Zhang, B. Teng, M. Fan, New application of Z-scheme Ag_3PO_4/g-C_3N_4 composite in converting CO_2 to fuel, Environ. Sci. Technol., 49 (2015) 649–656.

[58] Y. Zheng, L. Lin, B. Wang, X. Wang, Graphitic carbon nitride polymers toward sustainable photoredox catalysis, Angew. Chem. Int. Ed., 54 (2015) 12868–12884.

[59] J. Hong, D.K. Hwang, R. Selvaraj, Y. Kim, Facile synthesis of Br-doped g-C_3N_4 nanosheets via one-step exfoliation using ammonium bromide for photodegradation of oxytetracycline antibiotics, J. Ind. Eng. Chem., 79 (2019) 473–481.

[60] X. Hao, J. Zhou, Z. Cui, Y. Wang, Y. Wang, Z. Zou, Zn-vacancy mediated electron-hole separation in ZnS/g-C_3N_4 heterojunction for efficient visible-light photocatalytic hydrogen production, Appl. Catal., B, 229 (2018) 41–51.

[61] L. Yao, D. Wei, Y. Ni, D. Yan, C. Hu, Surface localization of CdZnS quantum dots onto 2D g-C_3N_4 ultrathin microribbons: highly efficient visible light-induced H_2-generation, Nano Energy, 26 (2016) 248–256.

[62] L. Zhang, Q. Liu, Y. Chai, W.L. Dai, Facile construction of phosphate incorporated graphitic carbon nitride with mesoporous structure and superior performance for H_2 production, Int. J. Hydrogen Energy, 43 (2018) 5591–5602.

[63] T. Montalvo-Herrera, D. Sánchez-Martínez, D.B. Hernandez-Uresti, E. Zarazua-Morin, Facile preparation of $KBiO_3$/g-C_3N_4 composites with microwave irradiation for photocatalytic hydrogen production, J. Chem. Technol. Biotechnol., 94 (2019) 3440–3446.

[64] A. Akhundi, A. Habibi-Yangjeh, Novel g-C_3N_4/Ag_2SO_4 nanocomposites: fast microwave-assisted preparation and enhanced photocatalytic performance towards degradation of organic pollutants under visible light, J. Colloid Interface Sci., 482 (2016) 165–174.

[65] Z. Zhang, X. Li, H. Chen, G. Shao, R. Zhang, H. Lu, Synthesis and properties of Ag/ZnO/g-C_3N_4 ternary micro/nano composites by microwave-assisted method, Mater. Res. Express, 5 (2018) 015021.

[66] X.J. Wang, W.Y. Yang, F.T. Li, Y.B. Xue, R.H. Liu, Y.J. Hao, In situ microwave-assisted synthesis of porous N-TiO_2/g-C_3N_4 heterojunctions with enhanced visible-light photocatalytic properties, Ind. Eng. Chem. Res., 52 (2013) 17140–17150.

[67] R.I. Walton, Subcritical solvothermal synthesis of condensed inorganic materials, Chem. Soc. Rev., 31 (2002) 230–238.

[68] M. Li, L. Zhang, X. Fan, M. Wu, Y. Du, M. Wang, J. Shi, Dual synergetic effects in MoS_2/pyridine-modified g-C_3N_4 composite for highly active and stable photocatalytic hydrogen evolution under visible light, Appl. Catal., B, 190 (2016) 36–43.

[69] W. Chen, T.Y. Liu, T. Huang, X.H. Liu, G.R. Duan, X.J. Yang, S.M. Chen, A novel yet simple strategy to fabricate visible light responsive C, N-TiO_2/g-C_3N_4 heterostructures with significantly enhanced photocatalytic hydrogen generation, RSC Adv., 5 (2015) 101214–101220.

[70] Z. Jiang, C. Zhu, W. Wan, K. Qian, J. Xie, Constructing graphite-like carbon nitride modified hierarchical yolk–shell TiO_2 spheres for water pollution treatment and hydrogen production, J. Mater. Chem. A, 4 (2016) 1806–1818.

[71] Q.Z. Huang, J.C. Wang, P.P. Wang, H.C. Yao, Z.J. Li, In-situ growth of mesoporous Nb_2O_5 microspheres on g-C_3N_4 nanosheets for enhanced photocatalytic H_2 evolution under visible light irradiation, Int. J. Hydrogen Energy, 42 (2017) 6683–6694.

[72] F. Chang, J. Zhang, Y. Xie, J. Chen, C. Li, J. Wang, X. Hu, Fabrication, characterization, and photocatalytic performance of exfoliated g-C_3N_4–TiO_2 hybrids, Appl. Surf. Sci., 311 (2014) 574–581.

[73] C. Li, Z. Sun, Y. Xue, G. Yao, S. Zheng, A facile synthesis of g-C_3N_4/TiO_2 hybrid photocatalysts by sol–gel method and its enhanced photodegradation towards methylene blue under visible light, Adv. Powder Technol., 27 (2016) 330–337.

[74] J. Li, Y. Liu, H. Li, C. Chen, Fabrication of g-C_3N_4/TiO_2 composite photocatalyst with extended absorption wavelength range and enhanced photocatalytic performance, J. Photochem. Photobiol., A, 317 (2016) 151–160.

[75] X. Tian, Y.J. Sun, Y.J. He, X.J. Wang, J. Zhao, S.Z. Qiao, F.T. Li, Surface P atom grafting of g-C_3N_4 for improved local spatial charge separation and enhanced photocatalytic H_2 production, J. Mater. Chem. A, 7 (2019) 7628–7635.

[76] L. Yang, J. Huang, L. Shi, L. Cao, Q. Yu, Y. Jie, J. Ye, A surface modification resultant thermally oxidized porous g-C_3N_4 with enhanced photocatalytic hydrogen production, Appl. Catal., B, 204 (2017) 335–345.

[77] G. Liu, P. Niu, C. Sun, S.C. Smith, Z. Chen, G.Q. Lu, H.M. Cheng, Unique electronic structure induced high photoreactivity of sulfur-doped graphitic C_3N_4, J. Am. Chem. Soc., 132 (2010) 11642–11648.

[78] H. Wang, C. Yang, M. Li, F. Chen, Y. Cui, Enhanced photocatalytic hydrogen production of restructured B/F codoped g-C_3N_4 via post-thermal treatment, Mater. Lett., 212 (2018) 319–322.

[79] M. Bellardita, E.I. García-López, G. Marcì, I. Krivtsov, J.R. García, L. Palmisano, Selective photocatalytic oxidation of aromatic alcohols in water by using P-doped g-C_3N_4, Appl. Catal., B, 220 (2018) 222–233.

[80] Y.P. Yuan, S.W. Cao, Y.S. Liao, L.S. Yin, C. Xue, Red phosphor/g-C_3N_4 heterojunction with enhanced photocatalytic activities for solar fuels production, Appl. Catal., B, 140 (2013) 164–168.

[81] W. Lin, Y. Cao, P. Wang, M. Sun, Unified treatment for plasmon–exciton co-driven reduction and oxidation reactions, Langmuir, 33 (2017) 12102–12107.

[82] X. Li, W. Cai, J. An, S. Kim, J. Nah, D. Yang, R.S. Ruoff, Large-area synthesis of high-quality and uniform graphene films on copper foils, Science, 324 (2009) 1312–1314.

[83] J. Liu, H. Wang, Z.P. Chen, H. Moehwald, S. Fiechter, R. van de Krol, M. Antonietti, Microcontact-printing-assisted access of graphitic carbon nitride films with favorable textures toward photoelectrochemical application, Adv. Mater., 27 (2015) 712–718.

[84] S. Zhang, N.T. Hang, Z. Zhang, H. Yue, W. Yang, Preparation of g-C_3N_4/graphene composite for detecting NO_2 at room temperature, Nanomaterials, 7 (2017) 12, doi: 10.3390/nano7010012.

[85] Y. Zhao, F. Zhao, X. Wang, C. Xu, Z. Zhang, G. Shi, L. Qu, Graphitic carbon nitride nanoribbons: graphene-assisted formation and synergic function for highly efficient hydrogen evolution, Angew. Chem. Int. Ed., 53 (2014) 13934–13939.

[86] Z. Zhang, F. Xiao, L. Qian, J. Xiao, S. Wang, Y. Liu, Facile synthesis of 3D MnO_2–graphene and carbon nanotube–graphene composite networks for high-performance, flexible, all-solid-state asymmetric supercapacitors, Adv. Energy Mater., 4 (2014) 1400064, doi: 10.1002/aenm.201400064.

[87] H. Huang, S. Yang, R. Vajtai, X. Wang, P.M. Ajayan, Pt-decorated 3D architectures built from graphene and graphitic carbon nitride nanosheets as efficient methanol oxidation catalysts, Adv. Mater., 26 (2014) 5160–5165.

[88] J. Duan, S. Chen, M. Jaroniec, S.Z. Qiao, Porous C_3N_4 nanolayers@N-graphene films as catalyst electrodes for highly efficient hydrogen evolution, ACS Nano., 9 (2015) 931–940.

[89] Y. Shi, L. Fu, X. Chen, J. Guo, F. Yang, J. Wang, Y. Hu, Hypophosphite/graphitic carbon nitride hybrids: preparation and flame-retardant application in thermoplastic polyurethane, Nanomaterials, 7 (2017) 259, doi: 10.3390/nano7090259.

[90] D. Xiao, K. Dai, Y. Qu, Y. Yin, H. Chen, Hydrothermal synthesis of α-Fe_2O_3/g-C_3N_4 composite and its efficient photocatalytic reduction of Cr(VI) under visible light, Appl. Surf. Sci., 358 (2015) 181–187.

[91] N.M. Deraz, The comparative jurisprudence of catalysts preparation methods: I. Precipitation and impregnation methods, J. Ind. Environ. Chem., 2 (2018) 19–21.

[92] S. Samanta, S. Martha, K. Parida, Facile synthesis of Au/g-C_3N_4 nanocomposites: an inorganic/organic hybrid plasmonic photocatalyst with enhanced hydrogen gas evolution under visible-light irradiation, ChemCatChem, 6 (2014) 1453–1462.

[93] N. Xiao, S. Li, S. Liu, B. Xu, Y. Li, Y. Gao, G. Lu, Novel PtPd alloy nanoparticle-decorated g-C_3N_4 nanosheets with enhanced photocatalytic activity for H_2 evolution under visible light irradiation, Chin. J. Catal., 40 (2019) 352–361.

[94] N. Xiao, Y. Li, S. Li, X. Li, Y. Gao, L. Ge, G. Lu, In-situ synthesis of PdAg/g-C_3N_4 composite photocatalyst for highly efficient photocatalytic H_2 generation under visible light irradiation, Int. J. Hydrogen Energy, 44 (2019) 19929–19941.

[95] A.E.A. Bakr, W.M. El Rouby, M.D. Khan, A.A. Farghali, B. Xulu, N. Revaprasadu, Synthesis and characterization of Z-scheme α-Fe_2O_3 NTs/ruptured tubular g-C_3N_4 for enhanced photoelectrochemical water oxidation, Sol. Energy, 193 (2019) 403–412.

[96] Z. Jiang, W. Wan, H. Li, S. Yuan, H. Zhao, P.K. Wong, A hierarchical Z-scheme α-Fe_2O_3/g-C_3N_4 hybrid for enhanced photocatalytic CO_2 reduction, Adv. Mater., 30 (2018) 1706108, doi: 10.1002/adma.201706108.

[97] L. Xu, J. Xia, H. Xu, S. Yin, K. Wang, L. Huang, H. Li, Reactable ionic liquid assisted solvothermal synthesis of graphite-like C_3N_4 hybridized α-Fe_2O_3 hollow microspheres with enhanced supercapacitive performance, J. Power Sources, 245 (2014) 866–874.

[98] H. Guo, M. Chen, Q. Zhong, Y. Wang, W. Ma, J. Ding, Synthesis of Z-scheme α-Fe_2O_3/g-C_3N_4 composite with enhanced visible-light photocatalytic reduction of CO_2 to CH_3OH, J. CO_2 Util., 33 (2019) 233–241.

[99] X.-N. Wei, H.-L. Wang, X.-K. Wang, W.-F. Jiang, Facile fabrication of mesoporous g-C_3N_4/TiO_2 photocatalyst for efficient degradation of DNBP under visible light irradiation, Appl. Surf. Sci., 426 (2017) 1271–1280.

[100] Y. Tan, Z. Shu, J. Zhou, T. Li, W. Wang, Z. Zhao, One-step synthesis of nanostructured g-C_3N_4/TiO_2 composite for highly enhanced visible-light photocatalytic H_2 evolution, Appl. Catal., B, 230 (2018) 260–268.

[101] R. Hao, G. Wang, H. Tang, L. Sun, C. Xu, D. Han, Template-free preparation of macro/mesoporous g-C_3N_4/TiO_2 heterojunction photocatalysts with enhanced visible light photocatalytic activity, Appl. Catal., B, 187 (2016) 47–58.

[102] L. Liu, Y. Qi, J. Hu, Y. Liang, W. Cui, Efficient visible-light photocatalytic hydrogen evolution and enhanced photostability of core@shell Cu_2O@g-C_3N_4 octahedra, Appl. Surf. Sci., 351 (2015) 1146–1154.

[103] D. Li, J. Zan, L. Wu, S. Zuo, H. Xu, D. Xia, Heterojunction tuning and catalytic efficiency of g-C_3N_4–Cu_2O with glutamate, Ind. Eng. Chem. Res., 58 (2019) 4000–4009.

[104] L. Liu, Y. Qi, J. Hu, W. An, S. Lin, Y. Liang, W. Cui, Stable Cu_2O@g-C_3N_4 core@shell nanostructures: efficient visible-light photocatalytic hydrogen evolution, Mater. Lett., 158 (2015) 278–281.

[105] P.Y. Kuang, Y.Z. Su, G.F. Chen, Z. Luo, S.Y. Xing, N. Li, Z, Q, Liu, g-C_3N_4 decorated ZnO nanorod arrays for enhanced photoelectrocatalytic performance, Appl. Surf. Sci., 358 (2015) 296–303.

[106] J. Liu, X.T. Yan, X.S. Qin, S.J. Wu, H. Zhao, W.B. Yu, B.L. Su, Light-assisted preparation of heterostructured g-C_3N_4/ZnO nanorods arrays for enhanced photocatalytic hydrogen performance, Catal. Today, 355 (2019) 932–936.

[107] P. Yang, J. Wang, G. Yue, R. Yang, P. Zhao, L. Yang, D. Astruc, Constructing mesoporous g-C_3N_4/ZnO nanosheets catalyst for enhanced visible-light driven photocatalytic activity, J. Photochem. Photobiol., A, 388 (2020) 112169, doi: 10.1016/j.jphotochem.2019.112169.

[108] W.K. Jo, N.C.S. Selvam, Enhanced visible light-driven photocatalytic performance of ZnO–g-C_3N_4 coupled with graphene oxide as a novel ternary nanocomposite, J. Hazard. Mater., 299 (2015) 462–470.

[109] S. Balu, S. Velmurugan, S. Palanisamy, S.W. Chen, V. Velusamy, T.C. Yang, E.S.I. El-Shafey, Synthesis of α-Fe_2O_3 decorated g-C_3N_4/ZnO ternary Z-scheme photocatalyst for degradation of tartrazine dye in aqueous media, J. Taiwan Inst. Chem. Eng., 99 (2019) 258–267.

[110] S. Cao, J. Yu, g-C_3N_4-based photocatalysts for hydrogen generation, J. Phys. Chem. Lett., 5 (2014) 2101–2107.

[111] Y. Wang, Q. Wang, X. Zhan, F. Wang, M. Safdar, J. He, Visible light driven type II heterostructures and their enhanced photocatalysis properties: a review, Nanoscale, 5 (2013) 8326–8339.

[112] Y.J. Bai, B. Lü, Z.G. Liu, L. Li, D.L. Cui, X.G. Xu, Q.L. Wang, Solvothermal preparation of graphite-like C_3N_4 nanocrystals, J. Cryst. Growth, 247 (2003) 505–508.

[113] J. Gao, Y. Zhou, Z. Li, S. Yan, N. Wang, Z. Zou, High-yield synthesis of millimetre-long, semiconducting carbon nitride nanotubes with intense photoluminescence emission and reproducible photoconductivity, Nanoscale, 4 (2012) 3687–3692.

[114] J. Mao, T. Peng, X. Zhang, K. Li, L. Ye, L. Zan, Effect of graphitic carbon nitride microstructures on the activity and selectivity of photocatalytic CO_2 reduction under visible light, Catal. Sci. Technol., 3 (2013) 1253–1260.

[115] B. Zhu, P. Xia, W. Ho, J. Yu, Isoelectric point and adsorption activity of porous g-C_3N_4, Appl. Surf. Sci., 344 (2015) 188–195.

[116] Y. Wang, X. Wang, M. Antonietti, Polymeric graphitic carbon nitride as a heterogeneous organocatalyst: from photochemistry to multipurpose catalysis to sustainable chemistry, Angew. Chem. Int. Ed., 51 (2012) 68–89.

[117] F. Al Marzouqi, R. Selvaraj, Y. Kim, Rapid photocatalytic degradation of acetaminophen and levofloxacin using g-C_3N_4 nanosheets under solar light irradiation, Mater. Res. Express, 6 (2020) 125538.

[118] M.A. Oturan, J.J. Aaron, Advanced oxidation processes in water/wastewater treatment: principles and applications. A review, Crit. Rev. Env. Sci. Technol., 44 (2014) 2577–2641.

[119] M. Yadav, R. Gupta, R.K. Sharma, Chapter 14–Green and Sustainable Pathways for Wastewater Purification, S. Ahuja, Ed., Advances in Water Purification Techniques: Meeting the Needs of Developed and Developing Countries, Elsevier, Delhi, 2019, pp. 355–383.

[120] L. Kotthoff, J. Keller, D. Lörchner, T.F. Mekonnen, M. Koch, Transformation products of organic contaminants and residues—overview of current simulation methods, Molecules, 24 (2019) 753, doi: 10.3390/molecules24040753.

[121] D.S. Bhatkhande, V.G. Pangarkar, A.A.C.M. Beenackers, Photocatalytic degradation for environmental applications–a review, J. Chem. Technol. Biotechnol., 77 (2002) 102–116.

[122] A. Mills, R.H. Davies, D. Worsley, Water purification by semiconductor photocatalysis, Chem. Soc. Rev., 22 (1993) 417–425.

[123] M.S. Kamal, S.A. Razzak, M.M. Hossain, Catalytic oxidation of volatile organic compounds (VOCs)–a review, Atmos. Environ., 140 (2016) 117–134.

[124] C. Yang, G. Miao, Y. Pi, Q. Xia, J. Wu, Z. Li, J. Xiao, Abatement of various types of VOCs by adsorption/catalytic oxidation: a review, Chem. Eng. J., 370 (2019) 1128–1153.

[125] J. Zhu, S.L. Wong, S. Cakmak, Nationally representative levels of selected volatile organic compounds in Canadian residential indoor air: population-based survey, Environ. Sci. Technol., 47 (2013) 13276–13283.

[126] C. He, J. Cheng, X. Zhang, M. Douthwaite, S. Pattisson, Z. Hao, Recent advances in the catalytic oxidation of volatile organic compounds: a review based on pollutant sorts and sources, Chem. Rev., 119 (2019) 4471–4568.

[127] R. Iranpour, H.H. Cox, M.A. Deshusses, E.D. Schroeder, Literature review of air pollution control biofilters and biotrickling filters for odor and volatile organic compound removal, Environ. Prog., 24 (2005) 254–267.

[128] E. Pelizzetti, C. Minero, V. Carlin, E. Borgarello, Photocatalytic soil decontamination, Chemosphere, 25 (1992) 343–351.

[129] S.L. Wang, Y. Zhu, X. Luo, Y. Huang, J. Chai, T.I. Wong, G.Q. Xu, 2D WC/WO_3 heterogeneous hybrid for photocatalytic decomposition of organic compounds with Vis–NIR light, Adv. Funct. Mater., 28 (2018) 1705357, doi: 10.1002/adfm.201705357.

[130] G.M. Zuo, Z.X. Cheng, H. Chen, G.W. Li, T. Miao, Study on photocatalytic degradation of several volatile organic compounds, J. Hazard. Mater., 128 (2006) 158–163.

[131] R. Perry, I.L. Gee, Vehicle emissions and effects on air quality: indoors and outdoors, Indoor Built Environ., 3 (1994) 224–236.

[132] T. Ohura, T. Amagai, X. Shen, S. Li, P. Zhang, L. Zhu, Comparative study on indoor air quality in Japan and China: characteristics of residential indoor and outdoor VOCs, Atmos. Environ., 43 (2009) 6352–6359.

[133] R. Selvaraj, S.M. Al-Kindy, M. Silanpaa, Y. Kim, Nanotechnology in environmental remediation: degradation of volatile organic compounds (VOCs) over visible-light-active nanostructured materials, Rev. Environ. Health, 29 (2014) 109–112.

[134] S. Atthajariyakul, T. Leephakpreeda, Real-time determination of optimal indoor-air condition for thermal comfort, air quality and efficient energy usage, Energy Build., 36 (2004) 720–733.

[135] Y. Lei, M. Ning, Thoughts on control path of the volatile organic compounds pollution during the period of "13th Five-Year", Sci. Environ. Prot., 45 (2017) 14–17.

[136] J. Ji, Y. Xu, H. Huang, M. He, S. Liu, G. Liu, D.Y. Leung, Mesoporous TiO_2 under VUV irradiation: enhanced photocatalytic oxidation for VOCs degradation at room temperature, Chem. Eng. J., 327 (2017) 490–499.

[137] S. Kumar, A.G. Fedorov, J.L. Gole, Photodegradation of ethylene using visible light responsive surfaces prepared from titania nanoparticle slurries, Appl. Catal., B, 57 (2005) 93–107.

[138] J. Mo, Y. Zhang, R. Yang, Novel insight into VOC removal performance of photocatalytic oxidation reactors, Indoor Air, 15 (2005) 291–300.

[139] H. Chen, C.E. Nanayakkara, V.H. Grassian, Titanium dioxide photocatalysis in atmospheric chemistry, Chem. Rev., 112 (2012) 5919–5948.

[140] M.H. Lee, E. Geva, B.D. Dunietz, Calculation from first-principles of golden rule rate constants for photoinduced subphthalocyanine/fullerene interfacial charge transfer and recombination in organic photovoltaic cells, J. Phys. Chem. C, 118 (2014) 9780–9789.

[141] Y. Yamada, Y. Kanemitsu, Determination of electron and hole lifetimes of rutile and anatase TiO_2 single crystals, Appl. Phys., 101 (2012) 133907, doi: 10.1063/1.4754831.

[142] K. Nakata, A. Fujishima, TiO_2 photocatalysis: design and applications, J. Photochem. Photobiol., C, 13 (2012) 169–189.

[143] A.H. Mamaghani, F. Haghighat, C.S. Lee, Photocatalytic oxidation technology for indoor environment air purification: the state-of-the-art, Appl. Catal., B, 203 (2017) 247–269.

[144] M. Jafarikojour, M. Sohrabi, S.J. Royaee, A. Hassanvand, Evaluation and optimization of a novel immobilized photoreactor for the degradation of gaseous toluene, CLEAN–Soil Air Water, 43 (2015) 662–670.

[145] J. Jeong, K. Sekiguchi, W. Lee, K. Sakamoto, Photodegradation of gaseous volatile organic compounds (VOCs) using TiO_2 photoirradiated by an ozone-producing UV lamp: decomposition characteristics, identification of by-products and water-soluble organic intermediates, J. Photochem. Photobiol., A, 169 (2005) 279–287.

[146] M. Sleiman, P. Conchon, C. Ferronato, J.M. Chovelon, Photocatalytic oxidation of toluene at indoor air levels (ppbv): towards a better assessment of conversion, reaction intermediates and mineralization, Appl. Catal., B, 86 (2009) 159–165.

[147] F.V. Lopes, R.A. Monteiro, A.M. Silva, G.V. Silva, J.L. Faria, A.M. Mendes, R.A. Boaventura, Insights into UV-TiO_2 photocatalytic degradation of PCE for air decontamination systems, Chem. Eng. J., 204 (2012) 244–257.

[148] A.K. Boulamanti, C.J. Philippopoulos, Photocatalytic degradation of C5–C7 alkanes in the gas–phase, Atmos. Environ., 43 (2009) 3168–3174.

[149] M.A. Sidheswaran, H. Destaillats, D.P. Sullivan, S. Cohn, W.J. Fisk, Energy efficient indoor VOC air cleaning with activated carbon fiber (ACF) filters, Build. Environ., 47 (2012) 357–367.

[150] M. Li, B. Lu, Q.F. Ke, Y.J. Guo, Y.P. Guo, Synergetic effect between adsorption and photodegradation on nanostructured TiO_2/activated carbon fiber felt porous composites for toluene removal, J. Hazard. Mater., 333 (2017) 88–98.

[151] H.H. Chun, W.K. Jo, Adsorption and photocatalysis of 2-ethyl-1-hexanol over graphene oxide–TiO_2 hybrids post-treated under various thermal conditions, Appl. Catal., B, 180 (2016) 740–750.

[152] A.K. Boulamanti, C.A. Korologos, C.J. Philippopoulos, The rate of photocatalytic oxidation of aromatic volatile organic compounds in the gas-phase, Atmos. Environ., 42 (2008) 7844–7850.

[153] J. Van Durme, J. Dewulf, W. Sysmans, C. Leys, H. Van Langenhove, Abatement and degradation pathways of toluene in indoor air by positive corona discharge, Chemosphere, 68 (2007) 1821–1829.

[154] O. Debono, F. Thevenet, P. Gravejat, V. Hequet, C. Raillard, L. Lecoq, N. Locoge, Toluene photocatalytic oxidation at ppbv levels: kinetic investigation and carbon balance determination, Appl. Catal., B, 106 (2011) 600–608.

[155] W. Den, C.C. Wang, Enhancement of adsorptive chemical filters via titania photocatalysts to remove vapor-phase toluene and isopropanol, Sep. Purif. Technol., 85 (2012) 101–111.

[156] W.A. Jacoby, D.M. Blake, J.A. Penned, J.E. Boulter, L.M. Vargo, M.C. George, S.K. Dolberg, Heterogeneous photocatalysis for control of volatile organic compounds in indoor air, J. Air Waste Manage. Assoc., 46 (1996) 891–898.

[157] F. Thevenet, C. Guillard, A. Rousseau, Acetylene photocatalytic oxidation using continuous flow reactor: gas phase and adsorbed phase investigation, assessment of the photocatalyst deactivation, Chem. Eng. J., 244 (2014) 50–58.

[158] H. Ourrad, F. Thevenet, V. Gaudion, V. Riffault, Limonene photocatalytic oxidation at ppb levels: Assessment of gas phase reaction intermediates and secondary organic aerosol heterogeneous formation, Appl. Catal., B, 168 (2015) 183–194.

[159] L. Yang, Z. Liu, J. Shi, H. Hu, W. Shangguan, Design consideration of photocatalytic oxidation reactors using TiO_2-coated foam nickels for degrading indoor gaseous formaldehyde, Catal. Today, 126 (2007) 359–368.

[160] W.H. Ching, M. Leung, D.Y. Leung, Solar photocatalytic degradation of gaseous formaldehyde by sol–gel TiO_2 thin film for enhancement of indoor air quality, Sol Energy, 77 (2004) 129–135.

[161] M. El-Roz, M. Kus, P. Cool, F. Thibault-Starzyk, New operando IR technique to study the photocatalytic activity and selectivity of TiO_2 nanotubes in air purification: influence of temperature, UV intensity, and VOC concentration, J. Phys. Chem. C, 116 (2012) 13252–13263.

[162] J. Mo, Y. Zhang, Q. Xu, R. Yang, Effect of TiO_2/adsorbent hybrid photocatalysts for toluene decomposition in gas phase, J. Hazard. Mater., 168 (2009) 276–281.

[163] V. Etacheri, C. Di Valentin, J. Schneider, D. Bahnemann, S.C. Pillai, Visible-light activation of TiO_2 photocatalysts: advances in theory and experiments, J. Photochem. Photobiol., C, 25 (2015) 1–29.

[164] S. Chu, Y. Wang, Y. Guo, J. Feng, C. Wang, W. Luo, Z. Zou, Band structure engineering of carbon nitride: in search of a polymer photocatalyst with high photooxidation property, ACS Catal., 3 (2013) 912–919.

[165] N. Abbas, M. Hussain, N. Russo, G. Saracco, Studies on the activity and deactivation of novel optimized TiO_2 nanoparticles for the abatement of VOCs, Chem. Eng. J., 175 (2011) 330–340.

[166] T. Yan, J. Long, X. Shi, D. Wang, Z. Li, X. Wang, Efficient photocatalytic degradation of volatile organic compounds by porous indium hydroxide nanocrystals, Environ. Sci. Technol., 44 (2010) 1380–1385.

[167] F. Petronella, A. Truppi, M. Dell'Edera, A. Agostiano, M.L. Curri, R. Comparelli, Scalable synthesis of mesoporous TiO_2 for environmental photocatalytic applications, Materials, 12 (2019) 1853.

[168] S. Apollo, M.S. Onyongo, A. Ochieng, UV/H_2O_2/TiO_2/Zeolite hybrid system for treatment of molasses wastewater, Iran. J. Chem. Chem. Eng., 33 (2014) 107–117.

[169] A. Fujishima, X. Zhang, Titanium dioxide photocatalysis: present situation and future approaches, C.R. Chim., 9 (2006) 750–760.

[170] G. Song, C. Luo, Q. Fu, C. Pan, Hydrothermal synthesis of the novel rutile-mixed anatase TiO_2 nanosheets with dominant [1] facets for high photocatalytic activity, RSC Adv., 6 (2016) 84035–84041.

[171] A.A. Assadi, A. Bouzaza, D. Wolbert, P. Petit, Isovaleraldehyde elimination by UV/TiO_2 photocatalysis: comparative study of the process at different reactors configurations and scales, Environ. Sci. Pollut. Res., 21 (2014) 11178–11188.

[172] A.A. Assadi, J. Palau, A. Bouzaza, D. Wolbert, Modeling of a continuous photocatalytic reactor for isovaleraldehyde oxidation: effect of different operating parameters and chemical degradation pathway, Chem. Eng. Res. Des., 91 (2013) 1307–1316.

[173] A.A. Assadi, A. Bouzaza, D. Wolbert, Study of synergetic effect by surface discharge plasma/TiO_2 combination for indoor air treatment: sequential and continuous configurations at pilot scale, J. Photochem. Photobiol., A, 310 (2015) 148–154.

[174] A.A. Assadi, A. Bouzaza, I. Soutrel, P. Petit, K. Medimagh, D. Wolbert, A study of pollution removal in exhaust gases from animal quartering centers by combining photocatalysis with surface discharge plasma: from pilot to industrial scale, Chem. Eng. Process. Process Intensif., 111 (2017) 1–6.

[175] A.A. Assadi, A. Bouzaza, D. Wolbert, Comparative study between laboratory and large pilot scales for VOC's removal from gas streams in continuous flow surface discharge plasma, Chem. Eng. Res. Des., 106 (2016) 308–314.

[176] L. Zou, Y. Luo, M. Hooper, E, Hu, Removal of VOCs by photocatalysis process using adsorption enhanced TiO_2–SiO_2 catalyst, Chem. Eng. Process. Process Intensif., 45 (2006) 959–964.

[177] X. Yang, J.A. Koziel, Y. Laor, W. Zhu, J.H. van Leeuwen, W.S. Jenks, R. Armon, VOC removal from manure gaseous emissions with UV photolysis and UV-TiO_2 photocatalysis, Catalysts, 10 (2020) 607, doi: 10.3390/catal10060607.

[178] R. Acharya, K. Parida, A review on TiO_2/g-C_3N_4 visible-light-responsive photocatalysts for sustainable energy generation and environmental remediation, J. Environ. Chem. Eng., 8 (2020) 103896, doi: 10.1016/j.jece.2020.103896.

[179] G. Xiao, S. Xu, P. Li, H. Su, Visible-light-driven activity and synergistic mechanism of TiO_2@g-C_3N_4 heterostructured photocatalysts fabricated through a facile and green procedure for various toxic pollutants removal, Nanotechnology, 29 (2018) 315601.

[180] S. Zhang, J. Li, M. Zeng, G. Zhao, J. Xu, W. Hu, X. Wang, In situ synthesis of water-soluble magnetic graphitic carbon nitride photocatalyst and its synergistic catalytic performance, ACS Appl. Mater. Interfaces, 5 (2013) 12735–12743.

[181] X. Lin, J. Xing, W. Wang, Z. Shan, F. Xu, F. Huang, Photocatalytic activities of heterojunction semiconductors Bi_2O_3/$BaTiO_3$: a strategy for the design of efficient combined photocatalysts, J. Phys. Chem. C, 111 (2007) 18288–18293.

[182] K.I. Katsumata, R. Motoyoshi, N. Matsushita, K. Okada, Preparation of graphitic carbon nitride (g-C_3N_4)/WO_3 composites and enhanced visible-light-driven photodegradation of acetaldehyde gas, J. Hazard. Mater., 260 (2013) 475–482.

[183] X. Zou, Y. Dong, S. Li, J. Ke, Y. Cui, X. Ou, Fabrication of V_2O_5/g-C_3N_4 heterojunction composites and its enhanced visible light photocatalytic performance for degradation of gaseous ortho-dichlorobenzene, J. Taiwan Inst. Chem. Eng., 93 (2018) 158–165.

[184] Y. Li, J. Wang, Y. Yang, Y. Zhang, D. He, Q. An, G. Cao, Seed-induced growing various TiO_2 nanostructures on g-C_3N_4 nanosheets with much enhanced photocatalytic activity under visible light, J. Hazard. Mater., 292 (2015) 79–89.

[185] R. Sun, Q. Shi, M. Zhang, L. Xie, J. Chen, X. Yang, W. Zhao, Enhanced photocatalytic oxidation of toluene with a coral-like direct Z-scheme $BiVO_4$/g-C_3N_4 photocatalyst, J. Alloys Compd., 714 (2017) 619–626.

[186] W. Yu, D. Xu, T. Peng, Enhanced photocatalytic activity of g-C_3N_4 for selective CO_2 reduction to CH_3OH via facile coupling of ZnO: a direct Z-scheme mechanism, J. Mater. Chem. A, 3 (2015) 19936–19947.

[187] Y. Bi, S. Ouyang, N. Umezawa, J. Cao, J. Ye, Facet effect of single-crystalline Ag_3PO_4 sub-microcrystals on photocatalytic properties, J. Am. Chem. Soc., 133 (2011) 6490–6492.

[188] Y. Shen, Z. Zhu, X. Wang, J. Gong, Y. Zhang, Synthesis of Z-scheme g-C_3N_4/Ag/Ag_3PO_4 composite for enhanced photocatalytic degradation of phenol and selective oxidation of gaseous isopropanol, Mater. Res. Bull., 107 (2018) 407–415.

[189] Y. Li, X. Wu, J. Li, K. Wang, G. Zhang, Z-scheme g-C_3N_4@$CsxWO_3$ heterostructure as smart window coating for UV isolating, Vis penetrating, NIR shielding and full spectrum photocatalytic decomposing VOCs, Appl. Catal., B, 229 (2018) 218–226.

[190] Y. Chen, W. Huang, D. He, Y. Situ, H. Huang, Construction of heterostructured g-C_3N_4/Ag/TiO_2 microspheres with enhanced photocatalysis performance under visible-light irradiation, ACS Appl. Mater. Interfaces, 6 (2014) 14405–14414.

[191] Y. Gong, X. Quan, H. Yu, H., S. Chen, Synthesis of Z-scheme Ag_2CrO_4/Ag/g-C_3N_4 composite with enhanced visible-light photocatalytic activity for 2,4-dichlorophenol degradation, Appl. Catal., B, 219 (2017) 439–449.

[192] H.T. Ren, S.Y. Jia, Y. Wu, S.H. Wu, T.H. Zhang, X. Han, Improved photochemical reactivities of Ag_2O/g-C_3N_4 in phenol degradation under UV and visible light, Ind. Eng. Chem. Res., 53 (2014) 17645–17653.

[193] R. He, J. Zhou, H. Fu, S. Zhang, C. Jiang, Room-temperature in situ fabrication of Bi_2O_3/g-C_3N_4 direct Z-scheme photocatalyst with enhanced photocatalytic activity, Appl. Surf. Sci., 430 (2018) 273–282.

[194] X. Zou, C. Ran, Y. Dong, Z. Chen, D. Dong, D. Hu, Y. Cui, Synthesis and characterization of $BiPO_4$/g-C_3N_4 nanocomposites with significantly enhanced visible-light photocatalytic activity for benzene degradation, RSC Adv., 6 (2016) 20664–20670.

[195] V.D. Dao, T.D. Nguyen, N. Van Noi, N.M. Ngoc, T.D. Pham, P. Van Quan, H.T. Trang, Superior visible light photocatalytic activity of g-C_3N_4/$NiWO_4$ direct Z system for degradation of gaseous toluene, J. Solid State Chem., 272 (2019) 62–68.

[196] M. Zhang, X. Liu, X. Zeng, M. Wang, J. Shen, R. Liu, Photocatalytic degradation of toluene by In_2S_3/g-C_3N_4 heterojunctions, Chem. Phys. Lett., 7 (2020) 100049, doi: 10.1016/j.cpletx.2020.100049.

[197] R. He, K. Cheng, Z. Wei, S. Zhang, D Xu, Room-temperature in situ fabrication and enhanced photocatalytic activity of direct Z-scheme BiOI/g-C_3N_4 photocatalyst, Appl. Surf. Sci., 465 (2019) 964–972.

[198] S. Weon, F. He, W. Choi, Status and challenges in photocatalytic nanotechnology for cleaning air polluted with volatile organic compounds: visible light utilization and catalyst deactivation, Environ. Sci. Nano, 6 (2019) 3185–3214.